Modeling Large-Scale Singular Climate Events for Integrated Assessment

D I S S E R T A T I O N

zur Erlangung des akademischen Grades
Doktor der Naturwissenschaften (Dr. rer. nat.)
in der Wissenschaftsdisziplin
Theoretische Physik

eingereicht an der
Mathematisch-Naturwissenschaftlichen Fakultät
der Universität Potsdam

vorgelegt von
Kirsten Zickfeld
geboren am 20.09.1971 in Saarbrücken

Potsdam, im Oktober 2003

We are at the very beginning of time for the human race. It is not unreasonable that we grapple with problems. But there are tens of thousands of years in the future. Our responsibility is to do what we can, learn what we can, improve the solutions, and pass them on.

Richard Feynman (1918 - 1988)

Abstract

Concerns have been raised that anthropogenic climate change could lead to large-scale singular climate events, i.e., abrupt nonlinear climate changes with repercussions on regional to global scales. One central goal of this thesis is the development of models of two representative components of the climate system that could exhibit singular behavior: the Atlantic thermohaline circulation (THC) and the Indian monsoon. These models are conceived so as to fulfill the main requirements of integrated assessment modeling, i.e., reliability, computational efficiency, transparency and flexibility.

The model of the THC is an interhemispheric four-box model calibrated against data generated with a coupled climate model of intermediate complexity. It is designed to be driven by global mean temperature change which is translated into regional fluxes of heat and freshwater through a linear down-scaling procedure. Results of a large number of transient climate change simulations indicate that the reduced-form THC model is able to emulate key features of the behavior of comprehensive climate models such as the sensitivity of the THC to the amount, regional distribution and rate of change in the heat and freshwater fluxes.

The Indian monsoon is described by a novel one-dimensional box model of the tropical atmosphere. It includes representations of the radiative and surface fluxes, the hydrological cycle and surface hydrology. Despite its high degree of idealization, the model satisfactorily captures relevant aspects of the observed monsoon dynamics, such as the annual course of precipitation and the onset and withdrawal of the summer monsoon. Also, the model exhibits the sensitivity to changes in greenhouse gas and sulfate aerosol concentrations that are known from comprehensive models.

A simplified version of the monsoon model is employed for the identification of changes in the qualitative system behavior against changes in boundary conditions. The most notable result is that under summer conditions a saddle-node bifurcation occurs at critical values of the planetary albedo or insolation. Furthermore, the system exhibits two stable equilibria: besides the wet summer monsoon, a stable state exists which is characterized by a weak hydrological cycle. These results are remarkable insofar, as they indicate that anthropogenic perturbations of the planetary albedo such as sulfur emissions and/or land-use changes could destabilize the Indian summer monsoon.

The reduced-form THC model is employed in an exemplary integrated assessment application. Drawing on the conceptual and methodological framework of the tolerable windows approach, emissions corridors (i.e., admissible ranges of CO_2 emissions) are derived that limit the risk of a THC collapse while considering expectations about the socio-economically acceptable pace of emissions reductions. Results indicate, for example, a large dependency of the width of the emissions corridor on climate and hydrological sensitivity: for low values of climate and/or hydrological sensitivity, the corridor boundaries are far from being transgressed by any plausible emissions scenario for the 21^{st} century. In contrast, for high values of both quantities low non-intervention scenarios leave the corridor already in the early decades of the 21^{st} century. This implies that if the risk of a THC collapse is to be kept low, business-as-usual paths would need to be abandoned within the next two decades.

All in all, this thesis highlights the value of reduced-form modeling by presenting a number of applications of this class of models, ranging from sensitivity and bifurcation analysis to integrated assessment. The results achieved and conclusions drawn provide a useful contribution to the scientific and policy debate about the consequences of anthropogenic climate change and the long-term goals of climate protection.

Zusammenfassung

Erkenntnisse aus paläoklimatologischen Studien, theoretischen Betrachtungen und Modellsimulationen deuten darauf hin, dass anthropogene Emissionen von Treibhausgasen und Aerosolen zu großskaligen, singulären Klimaereignissen führen könnten. Diese bezeichnen stark nichtlineare, abrupte Klimaänderungen, mit regionalen bis hin zu globalen Auswirkungen. Ziel dieser Arbeit ist die Entwicklung von Modellen zweier maßgeblicher Komponenten des Klimasystems, die singuläres Verhalten aufweisen könnten: die atlantische thermohaline Zirkulation (THC) und der indische Monsun. Diese Modelle sind so konzipiert, dass sie den Anforderungen der "Integrated Assessment"-Modellierung genügen, d.h., sie sind realistisch, recheneffizient, transparent und flexibel.

Das THC-Modell ist ein einfaches, interhemisphärisches Boxmodell, das anhand von Daten kalibriert wird, die mit einem gekoppelten Klimamodell mittlerer Komplexität erzeugt wurden. Das Modell wird durch die globale Mitteltemperatur angetrieben, die mit Hilfe eines linearen Downscaling-Verfahrens in regionale Wärme- und Süßwasserflüsse übersetzt wird. Die Ergebnisse einer Vielzahl von zeitabhängigen Simulationen zeigen, dass das Modell in der Lage ist, maßgebliche Eigenschaften des Verhaltens komplexer Klimamodelle wiederzugeben, wie die Sensitivität bezüglich des Ausmaßes, der regionalen Verteilung und der Rate der Klimaänderung.

Der indische Monsun wird anhand eines neuartigen eindimensionalen Boxmodells der tropischen Atmosphäre beschrieben. Dieses enthält Parametrisierungen der Oberflächen- und Strahlungsflüsse, des hydrologischen Kreislaufs und der Hydrologie der Landoberfläche. Trotz des hohen Idealisierungsgrades ist das Modell in der Lage, relevante Aspekte der beobachteten Monsundynamik, wie z.B. den Jahresgang des Niederschlags und das Eintritts- sowie Rückzugsdatum des Sommermonsuns, zufrieden stellend zu simulieren. Außerdem erfasst das Modell die Sensitivität des Monsuns bezüglich Änderungen der Treibhausgas- und Aerosolkonzentrationen, die aus komplexeren Modellen bekannt sind.

Eine vereinfachte Version des Monsunmodells wird für die Untersuchung des qualitativen Systemverhaltens in Abhängigkeit von Änderungen der Randbedingungen eingesetzt. Das bemerkenswerteste Ergebnis ist das Auftreten einer Sattelknotenbifurkation des Sommermonsuns für kritische Werte der planetaren Albedo oder der Sonneneinstrahlung. Darüber hinaus weist das Modell zwei stabile Zustände auf: neben dem niederschlagsreichen Sommermonsun besteht ein Zustand, der sich durch einen schwachen hydrologischen Kreislauf auszeichnet. Das Beachtliche an diesen Ergebnissen ist, dass anthropogene Störungen der Albedo, wie Schwefelemissionen und/oder Landnutzungsänderungen, zu einer Destabilisierung des indischen Monsuns führen könnten.

Das THC-Boxmodell findet exemplarische Anwendung in einem "Integrated Assessment" von Klimaschutzstrategien. Basierend auf dem konzeptionellen und methodischen Gerüst des Leitplankenansatzes werden Emissionskorridore (d.h. zulässige Spannen an CO_2-Emissionen) berechnet, die das Risiko eines THC-Zusammenbruchs begrenzen sowie sozioökonomische Randbedingungen berücksichtigen. Die Ergebnisse zeigen u.a. eine starke Abhängigkeit der Breite der Emissionskorridore von der Klima- und hydrologischen Sensitivität. Für kleine Werte einer oder beider Sensitivitäten liegt der obere Korridorrand bei weit höheren Emissionswerten als jene, die von plausiblen Emissionsszenarien für das 21. Jahrhundert erreicht werden. Für große Werte der Sensitivitäten hingegen, verlassen schon niedrige Emissionsszenarien den Korridor in den frühen Jahrzehnten des 21. Jahrhunderts. Dies impliziert eine Abkehr von den gegenwärtigen Emissionstrends innerhalb der kommenden Jahrzehnte, wenn

das Risko eines THC-Zusammenbruchs gering gehalten werden soll.

Anhand einer Vielzahl von Anwendungen - von Sensitivitäts- über Bifurkationsanalysen hin zu integrierter Modellierung - zeigt diese Arbeit den Wert reduzierter Modelle auf. Die Ergebnisse und die daraus zu ziehenden Schlußfolgerungen liefern einen wertvollen Beitrag zu der wissenschaftlichen und politischen Diskussion bezüglich der Folgen des anthropogenen Klimawandels und der langfristigen Klimaschutzziele.

Contents

Chapter 1

Introduction

1.1 Setting the stage

Human activity is changing the climate. In its Second Assessment Report (SAR), the Intergovernmental Panel on Climate Change (IPCC) for the first time asserted that human interference is having 'a discernible influence' on the climate system (Houghton et al. 1995). Since 1860, the time Otto developed the gasoline engine, global mean temperature has warmed by 0.6±0.2 °C (Houghton et al. 2001). Consequences of this rate of warming, which is unprecedented at the human time-scale, are being observed in natural systems worldwide: glaciers shrink, sea-ice extent and thickness decrease, plants flower and birds breed earlier, and a number of plant and animal species extend their ranges northwards or upwards (for a review cf. Walther et al. 2003). Statistically significant associations between these processes (Parmesan and Yohe 2003; Root et al. 2003) and trends in regional climate have recently led the IPCC to assert with high confidence 'a widespread and coherent impact of 20th-century climate change on many physical and biological systems' (McCarthy et al. 2001). Yet, as long as anthropogenic emissions of greenhouse gases are not effectively reduced, climate will continue to change. The most recent IPCC report projects a global mean temperature increase by 1.4–5.8 °C relative to 1990 at the end of this century (Houghton et al. 2001). Global mean temperature, however, is only a highly aggregated indicator of climatic changes. In the physical world, these changes will mainly be felt through local modifications in other climate variables including precipitation, soil moisture, storminess and annual or diurnal temperature ranges. Extreme occurrences in most of these variables, i.e., droughts, floods and storms are likely to increase in magnitude and frequency in a warmer world (Houghton et al. 2001).

1.2 Large-scale singular climate events

The climate is a complex system, i.e., it consists of a number of constituents such as ocean, atmosphere, biosphere and cryosphere which interact with each other in possibly strong nonlinear ways. Such complex, nonlinear systems, when persistently forced, may exhibit 'singular' behavior, i.e., they may evolve through a series of disruptions and phase transitions that render the system's variables discontinuous, unlimited or strongly oscillating (Schellnhuber 1997).

Past examples of singular behavior in response to smooth external forcing include large, abrupt climate changes evident in Greenland ice-core records (known as Dansgaard-Oeschger

oscillations; Dansgaard et al. 1993) and episodic, massive discharges of icebergs into the North Atlantic detected in ocean sediment cores (known as Heinrich events; Heinrich 1988).

This theoretical and palaeo-climatic evidence, supported by results from model simulations (Manabe and Stouffer 1988), has raised concern that anthropogenic greenhouse gas (GHG) forcing could cause singular responses in the future. Prominent examples of conceivable singular events with repercussions on regional or global scales (so-called 'large-scale singularities'; McCarthy et al. 2001) are the shutdown of the Atlantic thermohaline circulation, the transformation of continental monsoons, shifts in the El Niño - Southern Oscillation (ENSO) dynamics, the disintegration of ice-sheets with subsequent large sea-level rise, and the runaway carbon dynamics (McCarthy et al. 2001).

In recent years, these events and their potential consequences have attracted increasing interest in the policy arena. The reason is that they are believed to occur abruptly, possibly transcending the adaptive capabilities of human societies. Further, they could occur unanticipated (the reason why they are often termed 'surprises' in the literature; Schneider et al. 1998) and some of them be irreversible on time scales of centuries to millennia. These prospects call on climate policymakers and their advisors ('policy analysts') to appropriately deal with large-scale singularities.

1.3 Reduced-form climate modeling

Climate policy analysis often relies upon so-called integrated assessment (IA) models (IAMs). These cover the entire causal chain from socio-economic activities giving rise to greenhouse gas emissions, to concentrations, climate, and impacts. The need to limit the total computational costs of IAMS is the reason why they often rely on simplified representations of the subsystems involved. Furthermore, in a broad class of IAMs specific model variables (e.g., a global welfare functional) are calculated via optimization, which adds further demands on computational efficiency (cf. section 1.6). For these reasons, state-of-the-art climate models such as, for instance, three-dimensional general circulation models ('GCMs'), as well as Earth system models of intermediate complexity ('EMICs') are often too complex to be incorporated into IA frameworks.

Most IAMs incorporate 'reduced-form' climate models. These models attempt to capture the basic features, but not necessarily to reproduce the dimensionality of the real-world counterpart. Representatives of this class are, for instance, globally aggregated (i.e., zero-dimensional) climate models such as energy-balance models (e.g. MAGICC; Wigley 1994) or impulse response function (IRF) representations (e.g. NICCS; Hooss et al. 2001). Of the globally aggregated climate models standardly used in IAMs, none exhibits singular behavior. The reason is that the underlying components and the respective couplings are strongly linearized.

There is thus a strong need for the development of model components which:

- simulate singular responses of the climate system,
- meet the requirements of IA modeling.

One goal of this thesis is the development of reduced-form models of large-scale singularities suited for the inclusion into IAMs, that is, are realistic, computationally efficient, transparent and flexible (chapters 2 and 3).

Besides the employment in IA modeling, so conceived reduced-form models serve a number of other purposes. If the structure of the governing equations is simple enough, it is possible to unravel the existence of singular points (chapter 3). In fact, qualitative changes in the system's dynamics can then be identified by means of standard methods of Nonlinear Dynamics such as analytical bifurcation theory (Argyris et al. 1995). The critical threshold of the Atlantic thermohaline circulation, for instance, was discovered in a simple two-box model (Stommel 1961). If the model is flexible (i.e., allows one to easily change model parameters and structure), it is possible to investigate the sensitivity of output variables on uncertain parameters ('parametric uncertainties'), as well as on model configurations and representation of individual physical processes ('structural uncertainties'). In conjunction with low computational costs, this enables one to project relevant variables for a large number of model and parameter assumptions (chapter 2). For instance, the IPCC global mean temperature projections (Houghton et al. 2001) rely on simulations with the MAGICC model which was tuned to emulate nine different GCMs and was driven by the full range of scenarios proposed in the Special Report on Emissions Scenarios (SRES; Nakićenović and Swart 2000).

In the development of reduced-form models, this thesis focuses on two representative large-scale singularities, the nonlinear response of the Atlantic thermohaline circulation and the transformation of the Indian monsoon. The following two sections shall illustrate their relevance in the climate policy context, explain the reasons for their nonlinearity and raise questions pertinent to their modeling.

1.4 Nonlinear response of the Atlantic thermohaline circulation

The Atlantic thermohaline circulation (THC) is the part of the Atlantic ocean circulation which is driven by surface fluxes of heat and freshwater and subsequent interior mixing of heat and salt, as opposed to the wind-driven circulation (Rahmstorf 2003). In strongly confined regions in the North Atlantic (i.e., the central Labrador Sea and the Greenland-Iceland-Norwegian Sea) very dense water sinks to depth and entrains the neighboring water masses ('deep convection'). The horizontal pressure gradient between these dense waters and lighter waters at low latitudes and in the Southern Atlantic gives raise to a southward flow at depth. This deep flow is compensated at the surface by an opposite return flow, whereby light warm and salty waters are transported from the Tropics towards the northern latitudes. On their way northwards, these waters release huge amounts of heat to the atmosphere (up to 10^{15} W; Ganachaud and Wunsch 2000), contributing a large amount to the heat budget of the North Atlantic region.

Why the interest in the THC from a climate policy perspective? Evidence from palaeoclimate reconstructions (Dansgaard et al. 1993), theoretical considerations (Stommel 1961) and model simulations (Manabe and Stouffer 1988) suggests that the thermohaline circulation system is subject to a nonlinear threshold dynamics switching into and out certain states where either the circulation breaks down completely or a shift in the location of deep-water formation occurs.

Two feedback mechanisms have been identified as the primary reason for the nonlinearity of the THC: an advective and a convective feedback (Rahmstorf 1999). The advective feedback is linked to the northward transport ('advection') of salt, which increases the salinity and hence the density of the North Atlantic waters. This leads to an enhanced north-south

density gradient and, in turn, a stronger circulation. The convective feedback operates as follows: in the regions of the North Atlantic where deep convection occurs, freshwater from net precipitation is effectively mixed downwards. If for some reason (e.g., anomalous warm winter temperature), convection is inhibited, a fresh and light surface layer is formed, which impedes the restart of convection. Both feedbacks are positive, i.e. they tend to reinforce a given circulation pattern once it is active. This is the reason for the existence of multiple stable states of the circulation. As a consequence of the advective feedback, climatic states with and without deep-water formation in the North Atlantic (also referred to as THC 'on' and 'off' states) are both stable equilibria. This bistability was first demonstrated by Stommel with a simple box model (Stommel 1961) and later re-discovered by experiments with general circulation models (Manabe and Stouffer 1988). Concerning the convective feedback, some models indicate that it may lead to stable states with different convection patterns in the North Atlantic, for example, with or without convection in the Labrador Sea (Rahmstorf 1995).

Experiments with models have shown that anthropogenic climate change might act as a trigger for switches between different THC states. Manabe and Stouffer (1993), for example, simulated a complete shutdown of the THC for a quadrupling of atmospheric CO_2 concentrations. Rahmstorf and Ganopolski (1999a) obtained the transition to the off state for a scenario with CO_2 concentrations peaking at around 1200 ppm in the 22$^{\text{nd}}$ century and declining thereafter (for reference: the present-day CO_2 concentration is 360 ppm). Stocker and Schmittner (1997) found a permanent shutdown of the THC under stabilization of CO_2 concentrations at 750 ppm. The 'critical' stabilization level, however, was shown to be dependent on the rate at which the final CO_2 concentration level was attained. A regional shutdown of deep-water formation in the Labrador and the Greenland-Iceland-Norwegian (GIN) Sea was simulated by Wood et al. (1999) resp. Schaeffer et al. (2002) in the 21$^{\text{st}}$ century under 'business-as-usual' emissions scenarios.

The consequences of a complete collapse of the THC for the climate of the North Atlantic region are highly uncertain. The reason is that estimates of the magnitude and the exact location of the cooling anomaly associated with a reduction of the oceanic heat transport differ widely between models. Vellinga and Wood (2002), Ganopolski et al. (2001) and Manabe and Stouffer (1988), for example, simulated a maximum mean annual cooling of 6–12 °C. An outlier study even finds a cooling of up to 22 °C (Schiller et al. 1997). While in Ganopolski et al. (2001) and Manabe and Stouffer (1988) the maximum cooling is located over the western North Atlantic, in Vellinga and Wood (2002) it is centered over the eastern North Atlantic. Also, it is unclear to what extent the cooling over the North Atlantic could be compensated locally by greenhouse warming. Model simulations, though, reveal that a greenhouse gas induced collapse of the THC could lead to a sudden reversal of the warming trend and a cooling by 2–3 °C (relative to the peak warming) within a few decades touching north-western Europe and north-eastern America (Rahmstorf and Ganopolski 1999a). A shutdown of deep-water formation in the Labrador or the GIN Sea is shown to have mainly regional effects (Wood et al. 1999; Schaeffer et al. 2002).

In either case (i.e., regional or complete shutdown of the THC), circulation changes would affect the physical properties (e.g., temperature, mixed layer depth) of the North Atlantic waters, with possibly disruptive consequences for marine ecosystems and the services they provide (e.g., nutrition and carbon uptake; cf. Rahmstorf et al. 2003).

The threshold behavior of the THC has become the prototype for singular behavior in the climate system and has therefore attracted large scientific interest. The nonlinearities

associated with the THC have been explored in the full hierarchy of models, from conceptual box models (e.g., Stommel 1961, Huang et al. 1992, Tziperman et al. 1994, Rahmstorf 1996, Scott et al. 1999), to models of intermediate complexity (e.g., Stocker and Schmittner 1997, Rahmstorf and Ganopolski 1999a) and GCMs (e.g., Manabe and Stouffer 1988, Rahmstorf 1995).

In the development of a reduced-form THC model (chapter 2) we draw on this rich body of research. For the reasons laid out in section 2.1, we build on the interhemispheric four-box model of Rahmstorf (1996), which has proven to satisfactorily describe the overall phenomenon and reproduce even the weakening or shutdown of the THC in response to climate change. Central questions pursued in this thesis (chapter 2) are:

- Can reduced-form models be used to reliably project the evolution of the THC under climate change? How must they be conceived to serve this purpose?
- How sensitive is the reduced-form THC model to variations of uncertain physical parameters?
- How sensitive is the model to structural uncertainties, such as box configurations and inclusion/exclusion of physical processes?

The first question is of general interest. The latter two are particularly relevant in view of IA applications such as the one presented in chapter 4.

1.5 Transformation of the Indian monsoon

The Indian summer monsoon is a recurrent large-scale climate phenomenon: each year in May/June the northeasterly winds over India (the 'winter monsoon') are replaced by southwesterlies which are laden with moisture and lead to abundant rainfall. The change in the direction of the winds is caused by the reversal of the temperature contrast between the Eurasian landmass and the adjacent Indian Ocean (Webster et al. 1998): As the solar zenith migrates over the Northern Hemisphere, the land is heated relative to the ocean. Over land, the air expands and rises vertically in the atmosphere, producing a region of high atmospheric pressure in the upper troposphere. In contrast, a region of lower pressure develops over the Indian Ocean. This upper-level pressure gradient gives rise to a southward ('northerly') flow of air, which, because of the conservation of mass, is compensated by a surface flow moving from the ocean towards the land ('southerly'). The southwesterly direction arises because of the Coriolis force, which acts to deflect winds in the Northern Hemisphere to the right of their path.

Changes in the timing, intensity and intraseasonal variability of the Indian monsoon would profoundly impact the people living in the region. The monsoon rains play a crucial role for agricultural and industrial production, as they provide 75–90% of the annual rainfall over India. Approximately two thirds of the one billion inhabitants live in the rural areas of India and derive large part of their income from agriculture. Mudur (1995) estimates that a reduction of average rainfall by about 10% would seriously threaten agricultural performance, increasing the risk of widespread famine and economic disruptions. On the other hand, intensification of the Indian monsoon could lead to devastating floods.

The Indian summer monsoon is clearly a nonlinear phenomenon: already the onset is very abrupt, with the monsoon 'bursting' suddenly over the country. Also, the power of the

monsoon unfolds because of an important feedback mechanism involving moist processes: As soon as the land-ocean temperature gradient is reversed and the direction of the wind has changed, large amounts of moisture are transported towards India. Over the hot continent, this moist air is forced to rise and condensates, leading to the release of large amounts of latent heat to the middle and upper troposphere. This, in turn, strengthens the upper-level pressure gradient and hence the monsoon circulation (Webster 1987). Note that this 'moisture advection' feedback bears some resemblance with the salt advection feedback discussed above in the context of multiple stable states of the THC.

The development of a region of strong convection over India is related to the annual migration of the Intertropical Convergence Zone (ITCZ), a region of low surface pressure where the trade winds converge. In summer, the ITCZ migrates over the Indian subcontinent, where it is known as the Monsoon Trough (MT). The location of the MT switches between two preferred latitudes, one associated with convergence and abundant rainfall over India (the 'active' monsoon), the other with convergence over the equatorial Indian Ocean and poor rainfall over land (the 'break' monsoon). Palmer (1994) identified the active and break monsoon with the two regimes of the classical 3-component Lorenz (1963) model and put forward the idea that the transition between these regimes could be chaotic. This would explain the difficulty in predicting the fine-grain statistics of the monsoon associated with transitions between break and active phases (Palmer 1994; Webster et al. 1998).

Evidence from palaeoclimate studies indicates that the monsoon has undergone a number of abrupt changes, both during the last glacial period (Altabet et al. 2002) and during the Holocene (Gupta et al. 2003; Fleitmann et al. 2003; Morrill et al. 2003). Remarkably, these abrupt changes seem to be tied to similar events in the North Atlantic: times of weakened monsoon correspond to cold episodes in the North Atlantic, while times of stronger monsoon corresponds to warm episodes (Gupta et al. 2003). Whether abrupt shifts in monsoon strength were triggered directly by smooth changes in forcing (e.g., insolation) or indirectly via teleconnections with other parts of the climate system, in particular the North Atlantic and the tropical Pacific, cannot yet be resolved.

This palaeoclimatic evidence and the nonlinear nature of the Indian monsoon reveal the potential for abrupt changes of this system in the future. A number of studies have investigated the response of the Indian monsoon to anthropogenic emissions of greenhouse gases (GHGs) and aerosols (Meehl and Washington 1993; Lal et al. 1995; Meehl et al. 1996; Kitoh et al. 1997; Bhaskaran and Mitchell 1998; Boucher et al. 1998; Roeckner et al. 1999; Douville et al. 2000; Hu et al. 2000; May 2002; Lal et al. 2003). If GHG forcing alone is taken into account, mean precipitation increases during the summer monsoon in most of the cited studies. Some studies attribute this to a strengthening of the land-ocean temperature gradient and the associated pressure-driven flow (Meehl and Washington 1993; Bhaskaran and Mitchell 1998; Hu et al. 2000). Others found a weakening of the monsoon circulation under enhanced GHG conditions (Kitoh et al. 1997; Douville et al. 2000; May 2002). The net effect is nevertheless an intensification of precipitation because of the increased moisture content of the warmer air. If scattering aerosols such as sulfate are considered in addition to GHGs, most studies indicate a net weakening of the Indian monsoon relative to the present-day strength (Lal et al. 1995; Meehl et al. 1996; Boucher et al. 1998). The reason is that the aerosol forcing acts locally, cooling the land relative to the ocean. Exceptions are the studies by Roeckner et al. (1999) and Lal et al. (2003) where the strengthening of the monsoon due to greenhouse warming is found to dominate the damping effect of the aerosols. Given that most of these studies are time-slice (as opposed to time-dependent or 'transient') experiments,

none discusses the time scale of the detected monsoon changes.

The state of the science concerning the Indian monsoon differs from that concerning the THC: The system is presumed to be strongly nonlinear, but conclusive evidence has to be awaited. Well-defined thresholds, let alone multi-stability, have not been discovered. Probably as a consequence, conceptual modeling is by far not as common as in the THC case. We are aware of a single study where a box model of the (African) monsoon has been used (Brovkin et al. 1998). The simplest models available are models of intermediate complexity (Neelin and Zeng 2000; Zeng et al. 2000). We therefore embark on the ab initio development of a reduced-form model of the Indian monsoon (chapter 3). Conceptually, it is a one-dimensional box model of the tropical atmosphere. It includes parameterizations of the radiative and surface fluxes, the hydrological cycle and surface hydrology. Central questions concern:

- the ability of the reduced-form model to realistically describe the observed monsoon dynamics
- the sensitivity of the model to changes in model parameters and boundary conditions.

Given that little is known about the existence of singular points in the dynamics of the Indian monsoon, it is of great interest to explore the possibility of changes in the qualitative system behavior. To this end, we reduce the 'basic' model to a somewhat simpler form which is amenable to analytic bifurcation[1] analysis. This allows us to seek answer to the following questions:

- Do bifurcation points exist in the reduced model's joint phase[2] and parameter space? Where are they located relative to the present-day state?

In order to be of relevance to climate policy, the possible existence of bifurcation points in the dynamics of the reduced-form monsoon would have to be confirmed by experiments with comprehensive models, setting the cornerstones of a research agenda (chapter 5.2).

1.6 Integrated assessment modeling of climate change

The prospect that anthropogenic climate change could inflict severe impacts upon human societies calls on policymakers to take appropriate response measures - reduce anthropogenic greenhouse gas emissions or enhance the adaptive capacity of endangered systems. Nations worldwide have recognized the salience of climate change and signed a legally binding charta, the United Nations Framework Convention on Climate Change (UNFCCC; UNEP/WMO 1992). In an often quoted passus, it calls for

> "...stabilization of greenhouse gas concentrations in the atmosphere at a level that would prevent dangerous anthropogenic interference with the climate system. Such a level should be achieved within a time frame sufficient to allow ecosystems to adapt naturally to climate change, to ensure that food production is not threatened and to enable economic development to proceed in a sustainable manner"(Article 2).

[1] Bifurcations are qualitative transitions of dynamical systems (e.g. stability changes) which occur when parameter cross critical values (the 'bifurcation points').

[2] The phase space of an n-dimensional system is here defined according to Argyris et al. (1995) as the space spanned by the variables x_1, x_2,..., x_n.

This perfectly illustrates the multi-dimensionality of the climate change issue: What is 'dangerous' climate change? What are 'safe' concentration levels? What rate of climate change exceeds the adaptive capacity of natural ecosystems and the food production system? How can safe concentration levels be achieved in a cost-effective manner?

These questions pertain to the realm of climate policy analysis and the tools it relies upon - the integrated assessment models. As mentioned above, IAMs comprise a variety of components simulating the socio-economic activities giving rise to greenhouse gas emissions, the carbon cycle, the climate system, and the sectors affected by climate change, allowing one to explore climate-policy related problems in an 'integrated' manner (for a review of IA approaches cf. Schneider 1997, Schellnhuber and Yohe 1998). One prominent paradigm in IA modeling has so far been cost-benefit analysis (cf., e.g., Nordhaus 1994), whereby emissions reduction costs are balanced against benefits of avoided damages to calculate 'optimal' emissions trajectories. The conclusions emerging from standard cost-benefit IAMs is that economic efficiency considerations do not justify more than very minor emissions reductions (Nordhaus 1994).

The recognition that the future evolution of the climate system could feature singular behavior has led several scientists to call that IAMs take singular climate events into account (Schellnhuber 1997; Schneider and Thompson 2000). Some pioneering studies have since been conducted (Keller et al. 2000; Mastrandrea and Schneider 2001), but adequate incorporation of singularities is by far not the rule in state-of-the-art IAMs. One reason is that one predominant paradigm in IA modeling - cost-benefit analysis - struggles in dealing with singularities (for a detailed discussion cf. Schellnhuber 1997, Wright 2003).

These difficulties have led scientists to think of alternative approaches. Turning the tables, Schellnhuber (1997) proposes to take advantage of the existence of systemic thresholds in the climate system in the search for sustainable management strategies: singular points may provide 'knock-out criteria' given that any responsible climate policy should strive for avoiding them - because approaching or transgressing critical points would possibly inflict intolerable impacts upon natural or socio-economic systems (Schellnhuber 1998; Schellnhuber 1999).

An integrated assessment framework which is conceived in the spirit of avoiding unacceptable impacts is the 'tolerable windows approach' (TWA or 'guardrail approach'; Petschel-Held et al. 1999; Bruckner et al. 1999). It is an inverse approach as it starts from singular points or, more generally, 'guardrails' excluding intolerable impact phenomena and unbearable mitigation costs and translates these backwards into admissible domains in climate (the 'tolerable climate window') and economic phase space and finally into admissible greenhouse gas emissions (Tóth et al. 2003a; Tóth et al. 2003b). The range of emissions which complies with the initially defined guardrails is referred to as 'emissions corridor'. Accordingly, an emissions corridor represents the leeway for action for climate policies committed to a specific goal (e.g., preventing 'dangerous' climate change).

In chapter 4, we move along the conceptual and methodological lines of the TWA to derive emissions corridors which limit the risk of singular climate change while also taking into account economically motivated guardrails. The scope of this analysis is twofold:

- demonstrate the suitability of the developed reduced-form models for integrated assessment,

- illustrate the kind of consequences the potential for singularities implies for climate policy.

To this end, we exemplarily employ the THC model presented in chapter 2 and link it to the globally aggregated ICLIPS climate model (Bruckner et al. 2003). The socio-economy is simply represented in the form of constraints on the emissions behavior. The modeling framework so obtained allows us to explore a number of policy-relevant questions:

- What is the leeway for climate policies committed to the preservation of the THC and to the avoidance of unacceptable mitigation costs?
- How sensitive is this leeway to assumptions about uncertain climate parameters?
- How sensitive is the leeway to the specified policy goals (i.e., the guardrails)?
- What is the timing of required emissions reductions?

With the modeling tools developed in this thesis, their application in the context of integrated assessment, and the resulting conclusions, we hope to deliver a useful contribution to the scientific and policy debate concerning long-term goals of climate protection such as those put forward by Article 2 of the UNFCCC.

Chapter 2

A reduced-form model for the response of the Atlantic thermohaline circulation to climate change

2.1 Motivation

The scope of this chapter is the development of a model of the Atlantic thermohaline circulation (THC) suited for the inclusion into integrated assessment (IA) frameworks. One main requirement on such a model (besides, obviously, physical soundness) is that it be computationally efficient, given that IA models (IAMs) incorporate a number of sub-modules and are often used in the optimization mode (cf. chapter 1). Another central demand on models employed in the policy-relevant context is that they be flexible, allowing one to explore the sensitivity of the variable of interest on the main uncertain physical quantities and processes. In ocean modeling, these are, for instance, the mixing parameterizations and the heat and freshwater fluxes at the surface, which largely determine the sensitivity of the THC to climate change (cf., e.g., Rahmstorf and Ganopolski 1999a). In view of uncertainty analysis, it is of advantage if the model is physically based such that its parameters can readily be identified with physical quantities (this is not the case, e.g., in fit models such as impulse response function (IRF) models, where the amplitudes and time scales of the IRF representation do not bear any physical meaning; cf. section 4.3.1).

Ocean general circulation models (OGCMs) are clearly too complex to be incorporated into IAMs. Ocean models of intermediate complexity, such as zonally-averaged models, provide an adequate level of physical complexity and flexibility (cf., e.g., Knutti et al. 2000). Nevertheless, even if up-scaled to include only a few hundred boxes, they are still to expensive for the computational tasks to be tackled in IA modeling. Appropriate computational efficiency is given in the conceptual THC models. Despite their limited representation of physical processes, these models have proven able to describe the essential characteristics of the THC dynamics.

The prototype of the class of conceptual THC models is the Stommel (1961) model. It consists of two boxes representing the tropical and the northern Atlantic. The THC is parameterized in terms of the horizontal density gradient between the two boxes. This

density gradient is maintained because of heat forcing at the box surface and the advection of salt by the circulation itself. This simple representation of the salt advection feedback (cf. section 1.4) enables the model to capture the main nonlinear features of the THC, i.e., the bifurcation point and the existence of multiple stable states. These characteristics are preserved in the suite of box models that have been developed following on Stommel's work. Of these, the majority represents the Atlantic basin north of the equator in two or four boxes (Huang et al. 1992; Tziperman et al. 1994; Gargett and Ferron 1996). Since observations and results from studies with OGCMs indicate that the THC is an interhemispheric process (cf., e.g., Rahmstorf 1996 and Thorpe et al. 2001), more recent box models of the Atlantic extend over two hemispheres (Rahmstorf 1996; Scott et al. 1999). These models differ mainly in the representation of the meridional freshwater fluxes. In the Rahmstorf (1996) model, these are taken to be equatorward in the southern and poleward in the Northern Hemisphere. The reason for this asymmetry is that these fluxes represent the total freshwater transport (i.e., atmospheric plus oceanic wind-driven) into resp. within the 'catchment area' of North Atlantic Deep Water (NADW) (which for the present-day circulation mode consists of the combined surface areas of the tropical and northern Atlantic). In the model described in Scott et al. (1999), the freshwater fluxes are poleward in both hemispheres, as they are taken to represent merely atmospheric water vapor transports. This difference in the representation of the freshwater fluxes leads to conceptually different pictures about the driving forces and the stability of the THC: in the Rahmstorf (1996) model, the circulation is driven by interhemispheric temperature gradients and slowed down by freshwater forcing, whereas in the Scott et al. (1999) model, the circulation is driven by salinity gradients and inhibited by thermal forcing. Since, according to GCM experiments, the freshwater balance postulated by Rahmstorf (1996) is more realistic, we have chosen his model as starting point for our work.

The model is described in detail in section 2.2. It has so far mainly been applied for theoretical investigations of bifurcations and the stability properties of the THC (Rahmstorf 1996; Rahmstorf and Ganopolski 1999b; Titz et al. 2002). The purpose of the present work is different: it aims at developing a model which reliably projects the time-dependent (or 'transient') response of the THC to climate change. Therefore, we extend the model to allow for the consideration of different box volumes and use it in the transient mode (Zickfeld et al. 2004). Given the physical simplicity of the four-box model, it would not be enough to determine the model parameters so as to reproduce the present-day state of the Atlantic Ocean. In fact, this would not guarantee for the ability of the model to realistically simulate climate states different from today's. Our strategy therefore consists in fitting the box-model parameters so as to emulate key aspects of the behavior exhibited by more complex models, which can be expected to be more realistic counterparts of the real-world ocean (section 2.3).

In view of IA applications, the box model should provide a simple interface for the coupling to the globally aggregated climate models standardly employed in IAMs. Since global mean temperature (GMT) is a standard output quantity of these models, it is convenient to link the models through this variable. Section 2.4 describes a procedure by which GMT can be appropriately down-scaled into fluxes of heat and freshwater needed to drive the THC model.

Given its simplicity, confidence has to be raised in the box model's ability to reliably project future THC changes. We therefore characterize the model response to a specific global mean temperature scenario for a wide range of parameter settings and discuss it in relation to the behavior exhibited by comprehensive coupled ocean-atmosphere models (section 2.5). This also allows us to gain insight about the sensitivity of the THC on parameter changes.

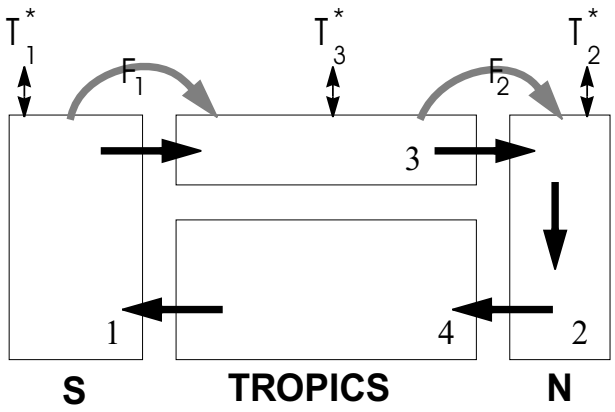

Figure 2.1: Schematic of the four-box model of the Atlantic thermohaline circulation. The temperatures of boxes 1, 2, and 3 are relaxed towards the values T_1^*, T_2^*, and T_3^*, respectively. The salinities are forced by the freshwater fluxes F_1 and F_2. The meridional flow (black arrows) is proportional to the density gradient between boxes 1 and 2.

Since the box model represents only the basic physical process underlying the THC (i.e., advection of heat and salt), the question arises whether inclusion of additional physical mechanisms would change the model behavior substantially. In section 2.6 we discuss the effects of including vertical and horizontal mixing on the transient model response.

2.2 Model description

The model configuration is shown in Fig. 2.1. It consists of four well-mixed boxes of different size, representing the southern, tropical, northern, and deep Atlantic, respectively. Neighboring boxes are connected to allow for a continuous, closed-loop circulation. The surface boxes exchange heat and freshwater with the overlying atmosphere. These surface fluxes render the water in the northern box denser than that in the southern box, giving rise to a pressure-driven circulation with northward flow near the surface and southward flow at depth. This picture reflects the view of the Atlantic THC as a cross-hemispheric circulation, with sinking in the North Atlantic and upwelling in the Southern Ocean, driven by thermohaline forcing (Rahmstorf 1996; Rahmstorf and England 1997).

In this four-box model, the meridional volume transport m (or 'overturning') is proportional to the density difference $\rho_2 - \rho_1$ between boxes 1 and 2:

$$m = \frac{k\,(\rho_2 - \rho_1)}{\rho_0} = k\,[\beta\,(S_2 - S_1) - \alpha\,(T_2 - T_1)] \tag{2.1}$$

where $S_2 - S_1$ and $T_2 - T_1$ are the north-south salinity and temperature gradients, respectively, k is a hydraulic constant linking volume transport m to the density difference, ρ_0 is the reference density, α and β are thermal and haline expansion coefficients. The rightmost side of Eq. 2.1 is obtained by presuming a linear equation of state.

The temperatures and salinities of the four boxes adjust to the oceanic transport of heat and freshwater. Further, temperatures and salinities of the surface boxes are forced by the overlying atmosphere. The surface heat fluxes are computed from the condition $Q = \Gamma\,(T^* - T)$. This formula, although having the same form as classical Haney restoring

(Haney 1971), has a different interpretation: the thermal coupling constant Γ subsumes the radiative relaxation constant and a constant related to atmospheric heat diffusion, and T^* defines the oceanic temperature in the absence of heat transport, rather than the surface air temperature (Rahmstorf and Willebrand 1995). Though extremely simple, this approach allows to capture the feedback of the oceanic heat transport on thermal forcing.

The freshwater fluxes F_i at the ocean surface consist of prescribed freshwater transports between the upper boxes. As discussed above, the latter do not only represent atmospheric water vapor transport but also wind-driven oceanic transport. This is the reason for their asymmetry: the gain of freshwater due to the wind-driven oceanic circulation more than compensates the loss of freshwater due to evaporation and hence the flux F_1 is directed equatorwards (i.e., into the NADW catchment).

This results in the following set of ordinary differential equations for temperatures T_i and salinities S_i of the four boxes:

$$\dot{T_1} = \frac{m}{V_1}(T_4 - T_1) + \lambda_1 (T_1^* - T_1) \tag{2.2}$$

$$\dot{T_2} = \frac{m}{V_2}(T_3 - T_2) + \lambda_2 (T_2^* - T_2) \tag{2.3}$$

$$\dot{T_3} = \frac{m}{V_3}(T_1 - T_3) + \lambda_3 (T_3^* - T_3) \tag{2.4}$$

$$\dot{T_4} = \frac{m}{V_4}(T_2 - T_4) \tag{2.5}$$

$$\dot{S_1} = \frac{m}{V_1}(S_4 - S_1) + \frac{S_0 F_1}{V_1} \tag{2.6}$$

$$\dot{S_2} = \frac{m}{V_2}(S_3 - S_2) - \frac{S_0 F_2}{V_2} \tag{2.7}$$

$$\dot{S_3} = \frac{m}{V_3}(S_1 - S_3) - \frac{S_0 (F_1 - F_2)}{V_3} \tag{2.8}$$

$$\dot{S_4} = \frac{m}{V_4}(S_2 - S_4)\,. \tag{2.9}$$

Here V_i are box volumes, λ_i thermal coupling constants, and T_i^* the temperatures the southern, northern and tropical boxes are relaxed towards. F_1 and F_2 are the freshwater fluxes (multiplied by a reference salinity, S_0, for conversion to a salt flux) into the tropical and northern Atlantic, respectively. Since the overturning m depends on both temperature T_i and salinity S_i, the differential equations are nonlinear. Note that in the above system of differential equations we have used upwind differencing assuming a positive (i.e., northward at the surface and southward at depth) meridional flow. For negative flow, the finite-difference form changes: in the advective terms, the temperature resp. salinity of the box which is located 'upwind' of the box under consideration has to be replaced (e.g. in Eq. 2.2 T_4 must be replaced with T_3).

2.2.1 Steady state solutions

In the following, equilibrium conditions are considered: then according to Eqs. (2.5) and (2.9) the deep box plays no role ($T_4 = T_2, S_4 = S_2$), and the steady state equations for temperature and salinity read:

$$\frac{m}{V_1}(T_2 - T_1) = \lambda_1 (T_1 - T_1^*) \tag{2.10}$$

$$\frac{m}{V_2}\left(T_3 - T_2\right) = \lambda_2\left(T_2 - T_2^*\right) \tag{2.11}$$

$$\frac{m}{V_3}\left(T_1 - T_3\right) = \lambda_3\left(T_3 - T_3^*\right) \tag{2.12}$$

$$m\left(S_2 - S_1\right) = -S_0 F_1 \tag{2.13}$$

$$m\left(S_3 - S_2\right) = S_0 F_2 \tag{2.14}$$

$$m\left(S_1 - S_3\right) = S_0\left(F_1 - F_2\right). \tag{2.15}$$

The combination of Eqs. (2.1) and (2.13) yields a quadratic equation in m:

$$m^2 + k\alpha\left(T_2 - T_1\right)m + k\beta S_0 F_1 = 0. \tag{2.16}$$

The north-south temperature gradient $T_2 - T_1$ can be expressed as a function of the parameters by combining Eqs. (2.10–2.12):

$$T_2 - T_1 = \left(T_2^* - T_1^*\right) + \frac{P_1^2\left(m\right)}{P_2^2\left(m\right)} \tag{2.17}$$

where the P_i^2 are 2^{nd} order polynomials in m:

$$P_1^2 = \left(\frac{\lambda_1\lambda_3}{V_2}\left(T_3^* - T_2^*\right) - \frac{\lambda_2\lambda_3}{V_1}\left(T_2^* - T_1^*\right)\right)m - \left(\frac{\lambda_1}{V_2V_3} + \frac{\lambda_2}{V_1V_3} + \frac{\lambda_3}{V_1V_2}\right)\left(T_2^* - T_1^*\right)m^2 \tag{2.18}$$

$$P_2^2 = \left(\frac{m}{V_1} + \lambda_1\right)\left(\frac{m}{V_2} + \lambda_2\right)\left(\frac{m}{V_3} + \lambda_3\right) - \frac{m^3}{V_1V_2V_3}. \tag{2.19}$$

Eq. (2.16) in combination with Eq. (2.17) results in a 4^{th} order equation in m. The structure of the physical solutions is identical to that discussed in Rahmstorf (1996) and Titz et al. (2002). For present-day climate conditions, i.e. $F_1 > 0$ and $T_1 > T_2$, two stable solutions exist: an 'on' mode with a vigorous overturning ($m > 0$) and a 'reverse' mode with sinking of water masses in the southern and upwelling in the northern box ($m < 0$). If F_1 is increased up to a critical value, a saddle-node bifurcation occurs such that the 'on' mode becomes unstable and the only stable solution is the 'reverse' mode.

Eq. (2.16) indicates that the equilibrium overturning depends only on F_1, not on F_2. This is due to the fact that under steady state conditions it makes no difference whether the freshwater enters the northern box via atmospheric transport or oceanic advection. F_2 merely determines the salinity gradient between the tropical and the northern boxes. In the transient case, however, it affects the response of the overturning, as on finite time scales atmospheric freshwater transport is more effective in freshening the northern box than oceanic advection. This implies that a large transient freshwater forcing F_2 may trigger a complete shutdown of the circulation. For an in-depth discussion of the role of the freshwater fluxes F_i and the stability properties of the four-box model cf. Rahmstorf (1996) and Titz et al. (2002).

As initial values for the transient experiments we use the steady state salinities S_i^{eq} and temperatures T_i^{eq} of the single boxes. The latter can be derived analytically from Eqs. (2.10–2.12) and Eq. (2.17):

$$T_1^{eq} = \frac{\frac{m_{eq}^2}{V_1V_2}\lambda_3T_3^* + \left(\frac{m_{eq}}{V_3} + \lambda_3\right)\left(\frac{m_{eq}}{V_1}\lambda_2T_2^* + \left(\frac{m_{eq}}{V_2} + \lambda_2\right)\lambda_1T_1^*\right)}{P_2^2\left(m_{eq}\right)}$$

$$
\begin{aligned}
T_2^{eq} &= \frac{\frac{m_{eq}^2}{V_2 V_3}\lambda_1 T_1^* + \left(\frac{m_{eq}}{V_1}+\lambda_1\right)\left(\frac{m_{eq}}{V_2}\lambda_3 T_3^* + \left(\frac{m_{eq}}{V_3}+\lambda_3\right)\lambda_2 T_2^*\right)}{P_2^2\left(m_{eq}\right)} \\
T_3^{eq} &= \frac{\frac{m_{eq}^2}{V_1 V_3}\lambda_2 T_2^* + \left(\frac{m_{eq}}{V_2}+\lambda_2\right)\left(\frac{m_{eq}}{V_3}\lambda_1 T_1^* + \left(\frac{m_{eq}}{V_1}+\lambda_1\right)\lambda_3 T_3^*\right)}{P_2^2\left(m_{eq}\right)}.
\end{aligned}
$$

where P_2^2 is defined as above. m_{eq} is the equilibrium overturning for the present-day value of F_1. The steady state salinity gradients are derived from Eqs. (2.13–2.15) as:

$$
\begin{aligned}
S_2^{eq} - S_1^{eq} &= -\frac{S_0 F_1}{m_{eq}} \\
S_3^{eq} - S_2^{eq} &= \frac{S_0 F_2}{m_{eq}} \\
S_1^{eq} - S_3^{eq} &= \frac{S_0\left(F_1 - F_2\right)}{m_{eq}}.
\end{aligned}
$$

2.3 Determination of the model parameters

As motivated in section 2.1, our fitting strategy consists in determining the model parameters such that key features of the behavior of more comprehensive models can be emulated. As benchmark we have chosen CLIMBER-2, a coupled ocean-atmosphere model of intermediate complexity, which has proven to successfully describe crucial elements of the climate system, including the THC (Petoukhov et al. 2000; Ganopolski et al. 2001). It is intended to tune the box model parameters such that not only the present-day state of the Atlantic ocean as simulated by CLIMBER-2 is reproduced, but also key features of its dynamic behavior as, for instance, the location of the bifurcation point of the THC. We therefore determine part of the unknown parameters (i.e., the restoring temperatures T_1^*, T_2^* and T_3^*, the flow constant k, and the thermal coupling constant Γ) by a least square fit of the equilibrium solution $m(F_1)$ of the box model to a hysteresis experiment performed with CLIMBER-2 (cf. Fig. 2.2). We impose additional constraints on the 'optimal' parameters by requiring equilibrium temperatures T_i^{eq} and overturning m_{eq} to be equal to the present-day CLIMBER-2 values (cf. Table 2.2). Since the latter are averaged over the corresponding regions in the Atlantic, the extents of the southern, tropical and northern boxes (i.e., V_i and z_i, $i \in \{1,2,3\}$) have to be fixed beforehand and are not part of the optimization.

It should be noted that for a given model the bifurcation diagram (i.e., the curve depicting the asymptotic response of a system against some parameter) conceptually differs from the hysteresis curve. In fact, the hysteresis is traced by diagnosing the transient response of the system to a transiently varying parameter (cf. caption of Fig. 2.2). However, if the rate at which the parameter is varied is slow enough, the system can be assumed to be in quasi-equilibrium such that the hysteresis curve is close to the asymptotic response. Fig. 2.2 demonstrates that in the case of the box model the hysteresis even coincides with the equilibrium curve for subcritical values of the freshwater forcing F_1. In CLIMBER-2, the equilibrium overturning for some fixed values of the freshwater perturbation is found to lie below the quasi-equilibrium response, the distance to the latter increasing in the proximity of the bifurcation point (Thomas Schneider, personal communication).

The extents of the surface boxes are chosen to roughly reflect the distribution of observed water masses in the Atlantic ocean. The tropical box extends from 30°S to 45°N, representing

		Model parameters
		Constants
c	4000 J kg^{-1} °C^{-1}	Specific heat capacity of sea water
ρ_0	1025 kg m^{-3}	Density of sea water
α	$1.7{\cdot}10^{-4}$ °C^{-1}	Thermal expansion coefficient
β	$8{\cdot}10^{-4}$ psu^{-1}	Haline expansion coefficient
S_0	35 psu	Reference salinity
		Fixed parameters
V_1	$1.1{\cdot}10^{17}$ m^3	Volume of the southern box
V_2	$0.4{\cdot}10^{17}$ m^3	Volume of the northern box
V_3	$0.68{\cdot}10^{17}$ m^3	Volume of the tropical box
V_4	$0.05{\cdot}10^{17}$ m^3	Volume of the deep box
z_1	3000 m	Depth of the southern box
z_2	3000 m	Depth of the northern box
z_3	1000 m	Depth of the tropical box
F_2	0.065 Sv	Freshwater transport from tropical to northern box
		Tunable parameters
T_1^*	6.6 °C	Relaxation temperature of the southern box
T_2^*	2.7 °C	Relaxation temperature of the northern box
T_3^*	11.7 °C	Relaxation temperature of the tropical box
Γ	$7.3{\cdot}10^8$ J yr^{-1} m^{-2} °C^{-1}	Thermal coupling constant
k	$25.4{\cdot}10^{17}$ m^3 yr^{-1}	Empirical flow constant

Table 2.1: Parameters of the box model. Note that the model is calibrated such that the equilibrium overturning $m_{eq} = m(F_1^{eq})$ is given for a freshwater flux F_1^{eq} equal to 0.014 Sv, which is the present-day value diagnosed in the CLIMBER-2 model. 1 Sv corresponds to 10^6 m^3 s^{-1}.

low latitude water above the main thermocline in the Atlantic at ∼1000 m depth. The northern box extends from 45°N-70°N, corresponding to the formation region of NADW. This water spreads southward at ∼3000 m depth and joins the water masses of the Antarctic Circumpolar Current (ACC) at approximately the latitudes of the Cape of Good Hope (30°S). Since the model does not represent the dynamics of the ACC, this is the latitude where the analogy between the box model and the 'real' Atlantic ends. Consequently, the southern box can be taken to represent any ocean portion outside the NADW catchment. In this study, the southern box is chosen to extend from 60°S to 30°S. The motivation is that the density difference between this part of the South Atlantic and the North Atlantic is shown to have the strongest correlation with the strength of the THC (Thorpe et al. 2001).

The remaining parameters, i.e. the freshwater transport F_2 and the volume of the deep box V_4, do not affect the equilibrium solutions of the box model (cf. Eqs. (2.16) and (2.17)) and therefore cannot be constrained by the optimization procedure outlined below. F_2 is derived by requiring a salinity gradient between the tropical and the northern box close to the CLIMBER-2 value. V_4 is determined such that the critical freshwater forcing in the transient case corresponds to the CLIMBER-2 value (cf. section 2.5). This results in a relatively small value for V_4 which is not unrealistic since only the portion of the deep Atlantic adjacent to the American continental slope is involved in the southward transport of NADW.

The individual coupling constants λ_i can be computed from the thermal coupling constant

Elements of the optimization	
Parameters:	
T_1^*, T_2^*, T_3^*, Γ, k	
Constraints:	
$\lvert G(F_{1i}, m_i, \vec{x})\rvert^2 \leq \delta_i$	match CLIMBER-2 hysteresis
$5 < T_1^{eq} < 7$ °C, $T_2^{eq} = 4.7$ °C, $T_3^{eq} = 11.4$ °C	match CLIMBER-2 temperatures
$m_{eq} = 22.6$ Sv	match CLIMBER-2 overturning
$10 < \Gamma < 75$ W m^{-2} °C^{-1}	keep Γ in realistic range

Table 2.2: Parameters and constraints used in the optimization. Note that the constraint for T_1^{eq} is given as inequality since the CLIMBER-2 value is not known exactly (cf. Table 2.3).

Γ and the respective box thickness z_i:

$$\lambda_i = \frac{\Gamma}{c\rho_0 z_i},$$

where c is the specific heat capacity of sea water and ρ_0 its density. An overview of the model parameters is given in Table 2.1.

The fitting procedure itself is performed by applying a mathematical optimization method to the weighted least-squares cost functional

$$J(\vec{m}, \vec{x}) \quad := \quad \frac{1}{2}\sum_{i=1}^{N} \omega_i (m_i - \bar{m}_i)^2. \tag{2.20}$$

Here

- $\vec{x} = (T_1^*, T_2^*, T_3^*, k, \Gamma)$ is the vector of parameters to be adjusted,
- $\vec{m} \in \mathbb{R}^N$ is a vector of approximations m_i to the equilibrium solutions $m(F_{1i}, \vec{x})$ of the box model for given F_{1i} and $\vec{x}$,
- $(F_{1i}, \bar{m}_i)_{i=1,\ldots,N}$ are data from the CLIMBER-2 hysteresis curve,
- the ω_i are non-negative weights used to enforce a closer fit in certain regions of the hysteresis curve, for example near the bifurcation point.

Each equilibrium solution m of the box model has to satisfy an equation

$$G(F_1, m, \vec{x}) \quad = \quad 0 \tag{2.21}$$

which is a 4^{th} order polynomial derived from Eqs. (2.16) and (2.17). To realize the coupling between F_{1i}, m_i, and x we thus have to impose Eq. (2.21) for all $i = 1, \ldots, N$ as additional constraints. Since Eq. (2.21) can only be solved approximately, we replace it by the least squares inequality

$$\lvert G(F_{1i}, m_i, \vec{x})\rvert^2 \quad \leq \quad \delta_i. \tag{2.22}$$

Here the δ_i can be used to adjust the desired accuracy point-wise. This is crucial since a very high prescribed accuracy for m_i may cause the optimization to fail because it stops at parameter values where some of the constraints are not satisfied.

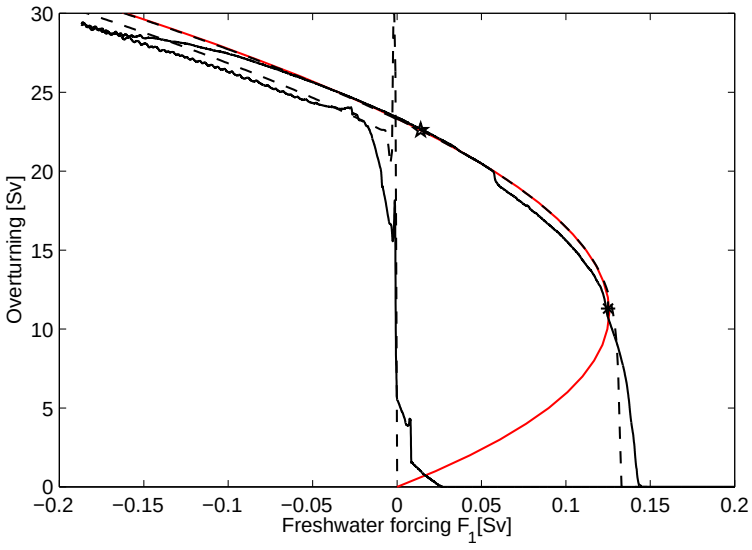

Figure 2.2: Positive branch of the equilibrium solutions $m(F_1)$ and hysteresis of the box model (red and dashed curves, respectively) and hysteresis derived with CLIMBER-2 (solid curve). The star and the asterisk denote the present-day overturning m_{eq} and the bifurcation point (F_1^{crit}, m_{crit})=(0.125 Sv, 11.3 Sv), respectively. The hysteresis curves are traced by slowly increasing and subsequently decreasing the freshwater flux into the Atlantic south of 50°N. The freshwater perturbation is applied at a rate of $0.05{\cdot}10^{-3}$ Sv/yr following the method described in Rahmstorf (1995). Note that in tracing the hysteresis of the box model the transition to the reverse circulation mode is inhibited by setting m to zero for $m < 0$.

The equality constraints for T_2^{eq} and T_3^{eq} and the inequality constraint for T_1^{eq} (cf. Table 2.2) are written as

$$c_j^{eq}(m_{eq}, \vec{x}) = 0, \quad j = 1, 2, \tag{2.23}$$

$$c_j(m_{eq}, \vec{x}) \leq 0, \quad j = 1, 2 \tag{2.24}$$

using nonlinear functions c_j^{eq}, c_j.

We thus end up with the minimization problem

$$\min_{(\vec{m},\vec{x})} J(\vec{m}, \vec{x}) \quad \text{subject to} \quad \text{Eqs. (2.22), (2.23), (2.24)}$$

and additional bounds on m_{eq} and Γ.

This problem is solved by the routine `fmincon` from MATLAB's optimization toolbox (distributed by The Mathworks Inc., Natick, MA, USA). It incorporates the constraints by introducing Lagrange multipliers.

The method makes use of provided sensitivity information of cost functional and constraints with respect to variations in $\vec{m}$ and $\vec{x}$. The computation of the sensitivities of the cost functional J is straight-forward; those of the more complex nonlinear constraints are computed *exactly*, i.e without any approximation errors, by the software tool ADMAT (Verma 2002). This tool algorithmically computes the derivatives along with the function value itself by evaluating G, c_j^{eq}, and c_j for given F_{1i}, m_i and $\vec{x}$. For a more detailed discussion of the algorithmic differentiation cf. Slawig and Zickfeld (2004).

Equilibrium values			
	Box model	CLIMBER-2	
T_1^{eq}	6.5 °C	5 to 7 °C	Equilibrium temperature of the southern box
T_2^{eq}	4.7 °C	4.7 °C	Equilibrium temperature of the northern box
T_3^{eq}	11.4 °C	11.4 °C	Equilibrium temperature of the tropical box
$S_1^{eq} - S_2^{eq}$	-0.02 psu	-0.3 to 0 psu	Equilibrium salinity gradient
$S_3^{eq} - S_2^{eq}$	0.1 psu	0.1 psu	Equilibrium salinity gradient
$S_3^{eq} - S_1^{eq}$	0.08 psu	0.1 to 0.4 psu	Equilibrium salinity gradient
m_{eq}	22.6 Sv	22.6 Sv	Equilibrium overturning

Table 2.3: Equilibrium values of the box model and present-day values of the CLIMBER-2 model (averaged over corresponding regions). Note that the values for T_1^{eq} and S_1^{eq} are determined only in approximate terms from CLIMBER-2 since the real-ocean analogy to the southern box is unclear.

The optimal fit to the CLIMBER-2 hysteresis is shown in Fig. 2.2 and the parameters of the box model are summarized in Table 2.1. The equilibrium mass transport, salinities and temperatures resulting from these parameters are shown in Table 2.3. For comparison, the present day values of the CLIMBER-2 model are also given.

2.4 Heat and freshwater forcing

It is the purpose to develop a low-order model of the Atlantic THC which can be driven by scenarios of global mean temperature (GMT) change. The reason is that the latter is the output of the globally aggregated climate models mostly used in integrated assessment frameworks. Therefore, an appropriate procedure for down-scaling changes in GMT into basin-wide patterns of changes in restoring temperatures ΔT_i^* and net freshwater fluxes ΔF_i which force the box model is needed. A common method for the efficient construction of regionally explicit climate change projections is the so-called scaled scenario approach (Mitchell et al. 1999; Smith and Pitts 1997). It describes future climate change by scaling spatial patterns of climate anomalies by the respective global mean temperature change ΔT^{GL}. Following this approach, changes in restoring temperatures ΔT_i^* evolve in accordance with:

$$\Delta T_i^*(t) = p_i \Delta T^{GL}(t),\ i \in \{1,2,3\}, \tag{2.25}$$

with constant values p_i. For determining the freshwater forcing, we take advantage of the fact that in CLIMBER-2 as well as in other models changes in the meridional atmospheric water vapor transports are approximately proportional (Manabe and Stouffer 1994; Ganopolski et al. 2001) to the mean temperature change in the Northern and Southern Hemisphere, i.e. ΔT^{NH} and ΔT^{SH}, respectively:

$$\Delta F_1(t) = h_1 \Delta T^{SH}(t) = h_1 p_{SH} \Delta T^{GL}(t), \tag{2.26}$$

$$\Delta F_2(t) = h_2 \Delta T^{NH}(t) = h_2 p_{NH} \Delta T^{GL}(t). \tag{2.27}$$

The constant factors p_i, p_j and h_k are derived from greenhouse gas simulations with the CLIMBER-2 model. The p_i ($i \in \{1,2,3\}$) are calculated by means of a constant least-squares fit to the ratio $\Delta T_i^{SAT}(t)/\Delta T^{GL}(t)$, where the ΔT_i^{SAT} are changes in surface air temperature over the respective Atlantic box. Here we implicitly assume that the ΔT_i^* correspond to

Climate change scenario parameters	
Regional temperature constants:	
p_1	0.86
p_2	1.07
p_3	0.79
p_{SH}	0.93
p_{NH}	1.07
Hydrological sensitivities:	
h_1	–0.005 Sv $^\circ$C^{-1}
h_2	0.013 Sv $^\circ$C^{-1}

Table 2.4: Climate change scenario parameters derived from simulations with the CLIMBER-2 model.

changes in surface air temperatures ΔT_i^{SAT}, although the T_i^* have a somewhat different physical interpretation. In fact the T_i^* are the temperatures the oceanic boxes would assume in the absence of overturning m and the associated heat transport, as discussed in section 2.2. Since we deal with anomalies in the two quantities, however, the approximation $\Delta T_i^* \approx \Delta T_i^{SAT}$ is justified. The p_j ($j \in \{NH, SH\}$) and the h_k ($k \in \{1, 2\}$) are obtained as above from the ratios $\Delta T^j(t)/\Delta T^{GL}(t)$ and $\Delta F_k(t)/\Delta T^j(t)$, respectively. The factor h_2, which considers the flux into the Atlantic north of 50°N, is in the following referred to as 'North Atlantic hydrological sensitivity' and is diagnosed as 0.013 Sv/°C in CLIMBER-2. h_1 and the temperature constants are given in Table 2.4. Under greenhouse warming, changes in the poleward atmospheric water vapor transport are positive in both hemispheres in CLIMBER-2. h_1 is negative since the perturbation ΔF_1 is as F_1 directed towards the equator. Changes in the freshwater transport by the wind-driven ocean circulation are assumed to be negligible.

The above formulation of temperature and freshwater forcing allows for a large flexibility in the consideration of uncertainties about the amount and regional distribution of the warming and changes in the hydrological cycle, which are among the main uncertain factors in predicting the response of the THC to climate change. Indeed, quantities which are 'diagnostic' in conventional climate models are here represented as parameters and can easily be varied. Not included is the feedback of THC changes on freshwater fluxes and GMT (recall that the feedback on thermal forcing is taken into account through the value of the thermal coupling constant Γ; cf. section 2.2). The feedback on GMT, however, appears to be small (Rahmstorf and Ganopolski 1999a), while the feedback of the circulation on meridional freshwater transport is in CLIMBER-2 and other models found to become relevant only after a complete shutdown of the THC (Hughes and Weaver 1996).

2.5 Transient climate change experiments

In this section, we characterize the response of the THC as simulated by the box model and compare it to the behavior of CLIMBER-2 and other comprehensive models. As forcing scenario we assume that GMT rises linearly by 4.5 °C over 150 years and stays constant thereafter. This scenario approximately mimics the response of the CLIMBER-2 model to a 4×CO_2 stabilization scenario, with CO_2 concentrations increasing at 1% per year. As initial conditions for the transient runs we use the steady state values given in Table 2.3.

In section 2.5.1 we discuss the box model response for standard parameter settings. In sections 2.5.2–2.5.5 we investigate the box model behavior for a broad range of forcing parameters and propose extensions of the model for taking into account ulterior sources of uncertainty.

2.5.1 Response of the THC for standard parameters

In the first experiment, the model parameters are set to their standard values (cf. Tables 2.1 and 2.4). The time series of the forcing and the main box model variables are shown in Fig. 2.3. As the temperatures T_i^* and the poleward atmospheric freshwater transports increase along with global mean temperature, the overturning slows down to 16.5 Sv. It recovers as soon as the forcing is stabilized. In qualitative terms, this corresponds to the behavior of CLIMBER-2 (cf. curve labelled '0.013' in Fig. 2.4) as well as of several other coupled ocean-atmosphere models (Houghton et al. 2001). Quantitatively, the overturning weakens less than in CLIMBER-2 and also recovers more rapidly. This is a consequence of the choice for the volume of the deep box V_4 which is taken to be rather small in order to reproduce the sensitivity of CLIMBER-2 to freshwater forcing ΔF_2 (cf. next section). Indeed, the smaller V_4, the shorter the timescale at which heat and freshwater perturbations are distributed among the boxes and the initial north-south density gradient is restored. This reduces the sensitivity of the system to perturbations and leads to a faster recovery of the circulation. One could have chosen the free parameter V_4 such that the amount of weakening and the recovery timescale of CLIMBER-2 were reproduced. We preferred the first option as in view of specific integrated assessment applications (Keller et al. 2000; Mastrandrea and Schneider 2001; Zickfeld and Bruckner 2003) our main interest lies in correctly reproducing the THC threshold. Also, the amount of weakening of the overturning as simulated by CLIMBER-2 is considerably lower and the recovery timescale much slower than in other models (Houghton et al. 2001).

In the box model the initial weakening of the overturning is mainly due to thermal forcing, as can be inferred from Fig. 2.3-e. Indeed, the northern box warms faster than the southern box (compare the blue and green curves in Fig. 2.3-c), leading to a reduction of the north-south temperature gradient which drives the flow. This effect is amplified by a negative feedback on salinity, since a weaker circulation implies reduced salt advection towards the northern latitudes.The recovery of the THC after stabilization of the forcing is primarily caused by the northward advection of the positive salinity anomaly that has formed in the Tropics (cf. Fig. 2.3-d and 2.3-e). The overturning does not fully regain its original strength because of the asymmetric warming of the southern and northern boxes which leads to a permanent weakening of the driving temperature gradient. A more detailed discussion of the role of the regional distribution of the warming in determining the response of the THC is given in the next section. The stabilization of the THC at a level which lies below the present-day value was also found by Schmittner and Stocker (1999) with a model of intermediate complexity. Note that in this case GCM experiments can hardly be used as reference since the runs are too short as to allow the models to reach a new equilibrium.

In order to further test the hypothesis that the initial weakening of the circulation is caused by thermal forcing, we isolate the latter from the freshwater forcing by setting h_2 to 0. We found that temperature effects alone, together with the negative feedback of the circulation on salinity, lead to a considerable weakening of the overturning (compare curves labelled '0' and '0.013' in Fig. 2.5). This behavior is similar to that exhibited by CLIMBER-2 as well as many other models where thermal forcing was found to be responsible for the weakening

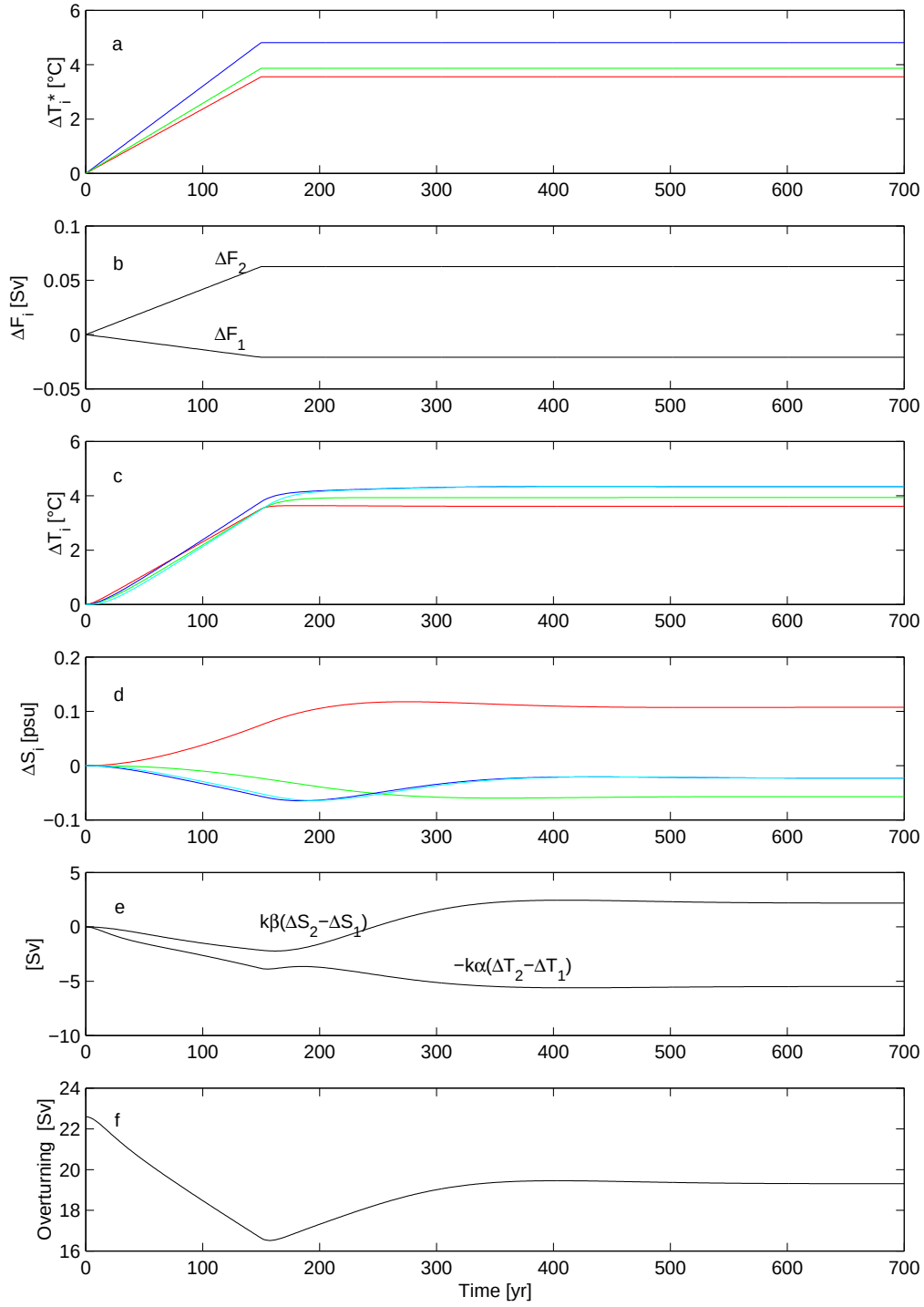

Figure 2.3: Time series of key model variables for standard parameter values: (a) regional temperature forcings (b) freshwater forcing, (c) temperature anomaly of each box, (d) salinity anomaly of each box, (e) contributions of temperature and salinity gradient anomalies to the overturning (cf. Eq. 2.1), (f) overturning. The deep blue curves denote changes related to the northern box, the green curves changes related to the southern box, the red curves changes related the tropical box and the light blue curves changes related to the deep ocean.

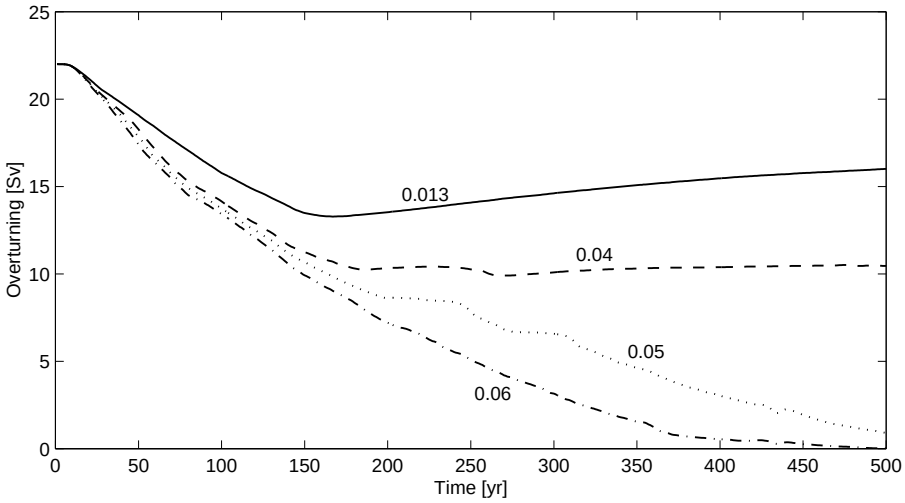

Figure 2.4: Response of the Atlantic overturning as simulated by CLIMBER-2 for standard and enhanced values of the hydrological sensitivity h_2 [Sv/°C]. The underlying scenario is a $4\times CO_2$ stabilization scenario with CO_2 concentrations increasing at 1% per year.

of the THC (Thorpe et al. 2001; Mikolajewicz and Voss 2000; Rahmstorf and Ganopolski 1999a; Schmittner and Stocker 1999). There are models, though, where the freshwater fluxes play the key role in slowing down the THC (Dixon et al. 1999).

2.5.2 Response for different assumptions about changes in the hydrological cycle

In a first set of experiments we investigated the response of the THC to the same scenario as above but for different values of the North Atlantic hydrological sensitivity h_2. This parameter is among the main uncertain quantities in predicting the fate of the THC. The reason is that estimates of evaporation, precipitation, river runoff and meltwater changes in the North Atlantic catchment differ largely. In the CLIMBER-2 model, for example, the value for h_2 is 0.013 Sv/°C, which is at the lower end of the range spanned by climate models (Rahmstorf and Ganopolski 1999a). The GFDL model shows a much stronger response of the hydrological cycle than CLIMBER-2: a 7.5 °C hemispheric warming leads to an additional freshwater flux to the North Atlantic of approximately 0.4 Sv, which results in a hydrological sensitivity of 0.053 Sv/°C (Manabe and Stouffer 1994). Recent observational studies were able to constrain at least part of the projected North Atlantic freshwater budget: Peterson et al. (2002) found that the Eurasian river discharge to the Arctic Ocean increased by 7% since 1936. Regressing discharge against GMT change over the same period, Peterson et al. (2002) provide an empirical estimate of the contribution of the Eurasian river discharge to the Atlantic hydrological sensitivity of 0.007 Sv/°C. Considering that Eurasian river discharge accounts for only approximately 40% of the total discharge to the Arctic Ocean and that meltwater runoff from ice sheets and glaciers and precipitation minus evaporation over the ocean also contribute to the Atlantic freshwater budget, this empirical estimate suggests that a value of 0.05 Sv/°C for the North Atlantic hydrological sensitivity is not unrealistic.

Scenarios with enhanced hydrological response are considered by increasing the hydrological sensitivity h_2 to 0.03, 0.04, 0.05 and 0.06 Sv/°C. For the above temperature scenario this

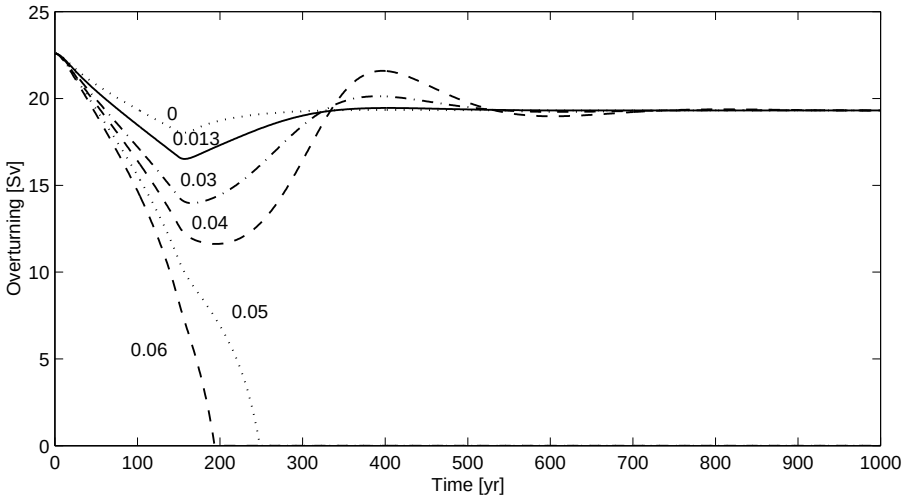

Figure 2.5: Response of the Atlantic overturning to the climate change scenario described in the text for different values of the hydrological sensitivity h_2 [Sv/°C].

leads to an additional freshwater transport ΔF_2 into the northern box of 0.14, 0.19, 0.24 and 0.29 Sv, respectively. The response of the overturning to these scenarios is shown in Fig. 2.5. The responses diverge, falling in two categories: those in which the overturning recovers and those in which it collapses. This is in line with CLIMBER-2 experiments where a critical value for the hydrological sensitivity h_2 was determined (cf. Fig. 2.4). The critical value h_2^{crit} in the box model is 0.046 Sv/°C, yielding a critical freshwater forcing ΔF_2 of 0.22 Sv. This value corresponds to that of CLIMBER-2 since the free parameter V_4 was tuned to reproduce this quantity (cf. section 2.3).

A notable feature in Fig. 2.5 is the 'overshooting' and subsequent oscillation of the overturning in the recovery phase for values of h_2 close to h_2^{crit}. This is due to the fact that in the latter case the overturning is slowed down considerably such that a strong positive salinity anomaly develops in the tropical box which is advected northwards as soon as the circulation regains strength. This might suggest that the overshooting is a model artefact due to the neglect of mixing processes. Indeed, the latter would allow for diffusive transport of salt out of the Tropics even in the absence of a vigorous overturning. The same mechanism (i.e., the massive advection of salt as the circulation regains strength) also causes the 'spike' in the hysteresis curve traced with the box model (cf. Fig. 2.2).

Note that for a hydrological sensitivity h_2 of 0.05 Sv/°C, which approximately corresponds to the value diagnosed in the GFDL model, the overturning collapses. This implies that for a suitable choice for h_2 the box model results are similar to those of the GFDL model where a collapse of the THC was found for a quadrupling of atmospheric CO_2 (Manabe and Stouffer 1993; Manabe and Stouffer 1999).

Another source of uncertainty concerns the freshwater forcing ΔF_1. In a set of experiments we explored the sensitivity of the model response to the perturbation ΔF_1 by scanning the hydrological sensitivity h_1 in the range 0 to –0.02 Sv/°C while keeping all other parameters at their standard values. In all cases, we found that qualitatively the model response changes little compared to that shown in Fig. 2.3: the overturning circulation is weakened and subsequently recovers. It reaches a minimum of 15.7 Sv for $h_1 = 0$ and 18.9 Sv for

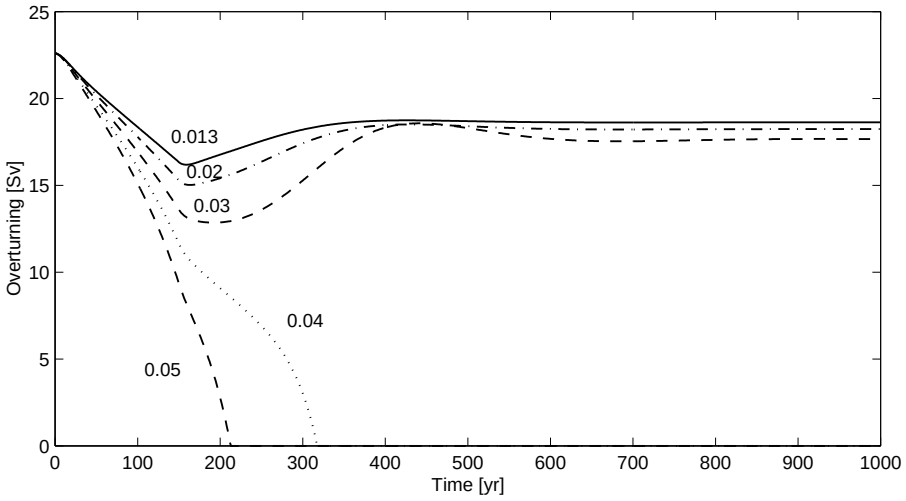

Figure 2.6: Response of the Atlantic overturning for different values of the hydrological sensitivity h_2^{tot} [Sv/°C]. 1/3 of the additional freshwater entering the northern box is provided by meltwater from ice sheets and glaciers in the North Atlantic catchment.

$h_1 = -0.02$ (compared to 16.5 Sv for the standard case $h_1 = -0.005$). We then increased h_2 as in the experiment above and computed the critical value for h_2: h_2^{crit} is lowered to 0.040 Sv/°C for $h_1 = 0$ and raised to 0.063 Sv/°C for $h_1 = -0.02$ (compared to 0.046 Sv/°C for $h_1 = -0.005$). This sensitivity can be explained as follows: the more negative h_1, the stronger the net freshwater export from the tropical Atlantic. The latter tends to counterbalance the freshening of the high latitudes through enhanced salt advection to the north. A positive h_1, on the other hand, would lead to a fresher tropical Atlantic and reduced salt advection, acting in the same direction as the freshening of the North Atlantic to destabilize the circulation.

So far we subsumed changes in the atmospheric freshwater transport F_2 and increased meltwater runoff from ice sheets and glaciers under the same forcing parameter, the hydrological sensitivity h_2. This is not fully correct since in the atmospheric vapor transport case, the freshwater gain in the North Atlantic is compensated by freshwater loss in the Tropics, whereas in the meltwater case it is not. For subsequent sensitivity experiments we modified the box model such that meltwater runoff from the Greenland ice sheet and meltwater from Arctic sea ice could be taken into account. This was achieved by introducing an additional meltwater flux F_2^{MW} into the northern box which is not compensated within the box model. We assume that changes in this flux can also be approximately described by a linear equation:

$$\Delta F_2^{MW} = h_2^{MW} \Delta T^{NH}. \tag{2.28}$$

The total freshwater forcing ΔF_2^{tot} of the northern box then is:

$$\Delta F_2^{tot} = \Delta F_2 + \Delta F_2^{MW} = \left(h_2 + h_2^{MW}\right) \Delta T^{NH} \equiv h_2^{tot} \Delta T^{NH}. \tag{2.29}$$

We assume that 1/3 of the total additional freshwater ΔF_2^{tot} entering the northern box is provided by meltwater (i.e., $h_2^{MW} = 1/3\, h_2^{tot}$). This implies that we expect the contributions from meltwater runoff and atmospheric transport to be of the same sign (i.e., positive) and order of magnitude. For Greenland, the latest report of the IPCC indicates a sensitivity of

0.001 to 0.005 Sv for a 1 °C *local* warming (Houghton et al. 2001). Given that in CLIMBER-2 and in other models the temperature change over Greenland is approximately twice as large as that of the Northern Hemisphere as a whole (i.e., $p^{GRL}/p^{NH} \approx 2$, where p^{GRL} is the temperature constant for Greenland), this range corresponds to $h_2^{MW} = 0.002 - 0.01$ Sv/°C in our notation. The contribution of sea ice to h_2^{MW} can be estimated as follows: in the last two decades or so, about 14% of perennial Arctic sea ice have melted away (Johannessen et al. 1999). Since perennial sea ice is about 3–4 m thick and occupies an area of $6–7 \cdot 10^6$ km^2, the contribution to the freshwater budget can be estimated to about 0.01 Sv. During the same time, annual mean air temperature in the Northern Hemisphere has increased by about 0.8 °C (Houghton et al. 2001). This would yield an estimate of 0.0125 Sv/°C for the contribution of sea ice to the hydrological sensitivity h_2^{MW}. Note, however, that this sensitivity declines as the Arctic sea ice cover fades away.

In a set of experiments we increase h_2^{tot} up to 0.05 Sv/°C and compute the corresponding circulation response. In this case the overturning is more sensitive than under increased atmospheric freshwater transport ΔF_2 alone (cf. Fig. 2.6): the critical value for h_2^{tot} is 0.039 Sv/°C, corresponding to a total freshwater forcing of 0.19 Sv (compared to 0.22 Sv above). This greater sensitivity can be explained as follows: in the case of enhanced meridional freshwater transport F_2 alone, the tropical box becomes more saline. This salt anomaly is subsequently advected poleward, increasing the salinity of the northern box and therefore stabilizing the circulation. When part of the additional freshwater is supplied by meltwater, the freshening of the northern box is only partly compensated by salinity advection from the Tropics. This also explains why in comparison to the experiments with enhanced meridional freshwater transport alone the overturning takes longer to re-intensify and no overshooting is observed. The above effect was already noted by Rahmstorf and Ganopolski (1999a): in global warming experiments they found the critical freshwater flux to differ by approximately 25% between the meltwater and the meridional transport cases.

In a recent paper Latif et al. (2000) pointed towards another possible source of uncertainty in simulating the response of the THC. They showed that greenhouse gas warming could lead to an additional freshwater export from the tropical Atlantic to the tropical Pacific with a stabilizing effect on the THC. The physical mechanism responsible for this freshwater transport was found to be an El Niño-like warming pattern in the eastern equatorial Pacific associated with changes in the atmospheric circulation in the Tropics. In order to allow for the consideration of inter-basin freshwater transport in the box model, we introduce a (negative) freshwater flux F_4 into the tropical box which is compensated in the Pacific (i.e., outside the box model). We again approximate changes in this freshwater flux by a linear relationship:

$$\Delta F_4 = h_4 \Delta T_3^*. \tag{2.30}$$

According to Latif et al. (2000) we set h_4 to –0.1 Sv/°C (i.e., a change in inter-basin freshwater transport of –0.2 Sv for ∼2 °C warming in the Tropics), while all other parameters are held at their standard values. Fig. 2.7 displays the response of the key box model variables under consideration of the freshwater export from the Atlantic to the Pacific. The overturning m is weakened slightly as long as the warming is sustained and then recovers, even exceeding the initial strength. This is due to the enhanced salinity in the Tropics which is advected northwards and leads to a permanent increase in the density gradient between the northern and the southern box. Because of this stabilizing mechanism, the freshwater perturbation ΔF_2 needed to shut down the circulation is almost twice as large as in experiments without inter-basin freshwater transport F_4 (0.38 Sv compared to 0.22 Sv). Note that the sustained

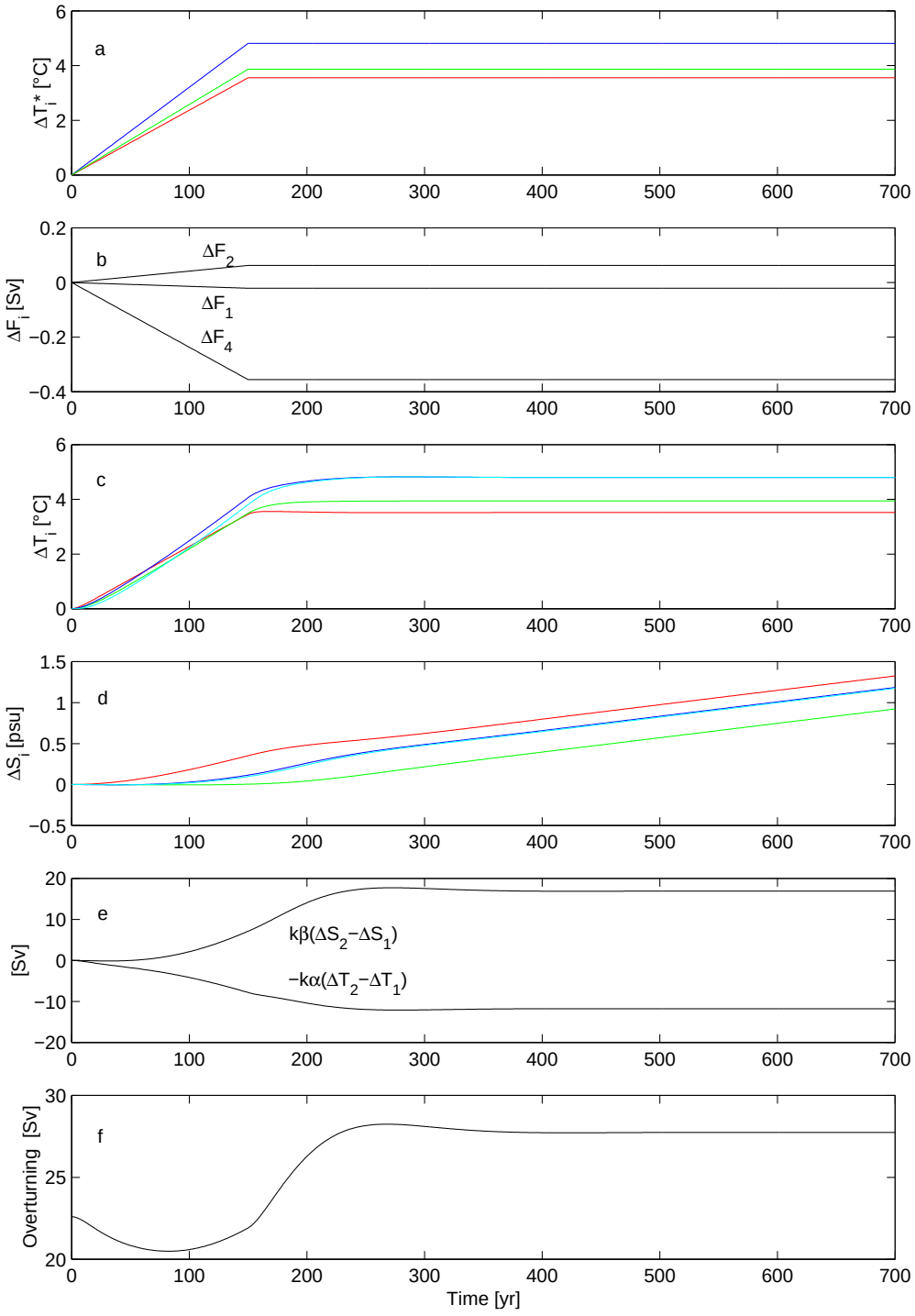

Figure 2.7: Time series of key model variables under enhanced freshwater export ΔF_4 from the tropical Atlantic. h_4 is –0.1 Sv/°C, all other parameters are at their standard values. (a) prescribed regional temperature forcings (b) prescribed freshwater forcings, (c) temperature anomaly of each box, (d) salinity anomaly of each box, (e) contributions of temperature and salinity gradient anomalies to the overturning (cf. Eq. 2.1), (f) overturning. The deep blue curves denote changes in the northern box, the green curves changes in the southern box, the red curves changes in the tropical box and the light blue curves changes in the deep ocean.

increase in the salinities of the four boxes (cf. Fig. 2.7-d) is due to an idealization of the box model (i.e., the isolation of the Atlantic from the other oceanic basins) which prevents the freshwater exported to the Pacific from circulating back into the Atlantic.

2.5.3 Response for different spatial patterns of temperature change

So far we investigated mainly the role of the uncertain freshwater fluxes in determining the response of the THC. Another factor contributing to the response is the unequal thermal forcing of the three boxes, as expressed by the parameters p_i (cf. Table 2.4). To study its effect we isolate the thermal from the freshwater forcing by fixing the p_j ($j \in \{NH, SH\}$) and performing a sensitivity analysis with respect to the p_i ($i \in \{1, 2, 3\}$). In the first experiment, we set the southern temperature parameter p_1 to the same value as the northern parameter p_2. We find that the overturning is reduced much less and recovers more rapidly as compared to the standard case and even exceeds its initial strength after the forcing is stabilized. This is because of the symmetric warming which does not act to offset the north-south temperature gradient as is the case for the standard assumption $p_1 < p_2$. As a consequence, after stabilization the thermal component of the circulation (i.e., $-k\alpha\,(\Delta T_2 - \Delta T_1)$) acts in the same direction of the haline component to strengthen the flow (contrarily to the standard case; cf. Fig. 2.3-e). Under this parameter setting (i.e., $p_1 = p_2$) the critical value for the hydrological sensitivity h_2 increases to 0.086 Sv/°C. We then assume equality between the tropical and the northern temperature constants by equating p_3 with p_2. The overturning is found to be more sensitive to the climate change scenario (h_2^{crit} is lowered to 0.041 Sv/°C). Indeed, as the thermal forcing of the tropical box is increased, the northward advection of warmer waters acts to further reduce the north-south density gradient. In a last experiment we set $p_3 = p_1 = p_2$. The circulation weakens less and recovers faster than for the standard p_i and exceeds its initial strength. The value of h_2^{crit} amounts to 0.079 Sv/°C. This indicates that in this case the stabilizing effect associated with the symmetric warming of both hemispheres outweighs the destabilizing effect due to advection of warmer tropical waters.

2.5.4 Response for different rates of temperature change

Results of a further set of experiments indicate that the THC as simulated in the box model is sensitive to the rate of climate change: the greater the rate of temperature increase, the stronger the weakening of the circulation (cf. Fig. 2.8). In a set of experiments with h_2 at the critical value (0.046 Sv/°C) and the other sensitivities at their standard values ($h_1 = -0.005$ Sv/°C, $h_2^{MW} = h_4 = 0$ Sv/°C) we found that for slower rates of temperature change the circulation weakens and then recovers, while for faster rates of change it irreversibly collapses. The 'critical' rate (i.e., 3 °C/century) is determined by the time scale at which excess heat and freshwater are redistributed among the boxes. This mechanism is similar to the one identified by Stocker and Schmittner (1997), who firstly demonstrated that the response of the THC is dependent upon the rate of climate change.

In order to allow for a quantitative comparison between our results and those obtained by Stocker and Schmittner (1997) (henceforth referred to as 'S&S'), we calculated the stability diagram of the THC in the temperature, rate of temperature increase (i.e., $(T, \dot{T})$) phase space assuming high, medium and low values of the hydrological sensitivity h_2 (i.e., 0.01, 0.03, 0.05 Sv/°C, respectively). The result is displayed in Fig. 2.9. Each marked point on the stability curves is obtained by prescribing the rate of temperature change and by increasing the temperature up to a value for which the circulation collapses. Fig. 2.9 also displays the

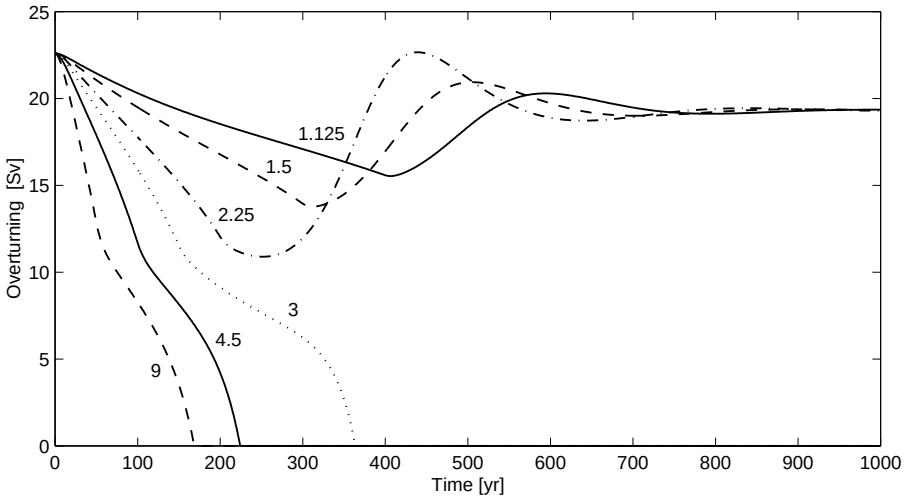

Figure 2.8: Response of the Atlantic overturning for different rates of temperature increase [°C/century]. The hydrological sensitivities are the same in all experiments ($h_2 = 0.046$ Sv/°C, $h_1 = -0.005$ Sv/°C, $h_2^{MW} = h_4 = 0$ Sv/°C).

stability curve calculated by S&S with a zonally-averaged ocean model. Note that originally this curve was computed in the CO_2 concentrations and rate of concentrations increase phase space. For the purpose of comparability, we use the S&S curve translated to $(T, \dot{T})$ phase space (cf. Tóth et al. 1998). Fig. 2.9 shows that the box model and the S&S curves are similar in shape, with a stronger sensitivity of the THC threshold on temperature increase for smaller rates of change. Our results also indicate that for the emulation of the stability properties of the model used by S&S, the hydrological sensitivity h_2 would need to be set to 0.04–0.05 Sv/°C.

2.5.5 Response for different initial overturning intensities

Lastly, the sensitivity of the circulation with respect to the initial overturning intensity m_{eq} is investigated. The initial overturning can be varied in two ways: by varying the model parameters, i.e., the *shape* of the equilibrium solution curve $m(F_1)$ (cf. Fig. 2.2), or by varying the freshwater flux F_1 (i.e., the *position* of m_{eq} on the solution curve). We here consider the model parameters to be fixed, and restrict ourselves to the second case. Fig. 2.2 suggests that the position of m_{eq} on the curve (i.e., the strength of the m_{eq}) determines the 'distance' of the system to the bifurcation point and hence the freshwater perturbation which is needed to shut down the circulation (cf. Rahmstorf 2000). To test the validity of this hypothesis for the transient case we adjusted the freshwater flux F_1 so to create weaker ($m_{eq} = 10 - 20$ Sv) and stronger ($m_{eq} = 25 - 30$ Sv) overturning rates compared to our standard setting ($m_{eq} = 22.6$ Sv). Note that these values for m_{eq} match the range of 10–30 Sv for the initial (i.e., control) overturning spanned by state-of-the-art climate models (Houghton et al. 2001). Observations-based studies estimate the present-day overturning at approximately 15 Sv (Ganachaud and Wunsch 2000; Stammer et al. 2002). For each case we then performed a sensitivity analysis with respect to the parameter h_2. The results are shown in Fig. 2.10. As conjectured, the stronger the initial overturning, the larger the critical value for the hydrological sensitivity. For $m_{eq} = 20$ Sv h_2^{crit} is 0.027 Sv/°C, for $m_{eq} = 25$ Sv h_2^{crit}

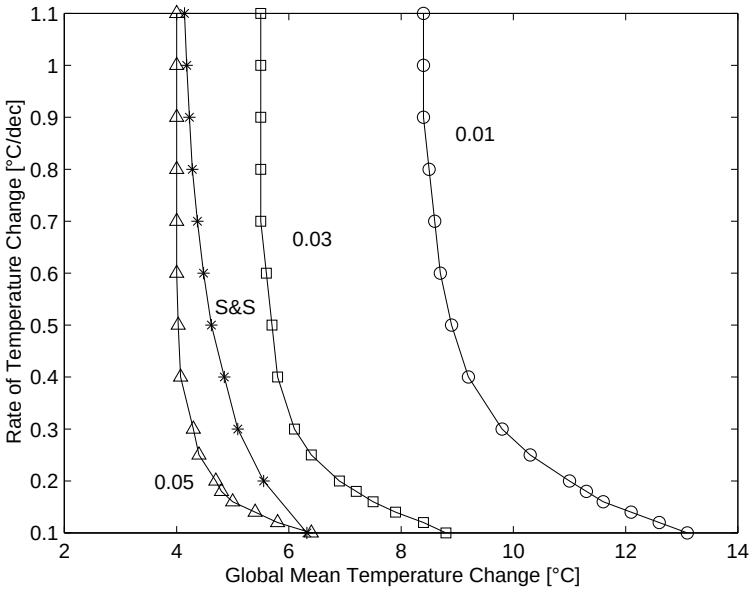

Figure 2.9: Stability diagram of the THC in (T, $\dot{T}$) phase space for different assumptions about the hydrological sensitivity h_2 [Sv/°C]. The stable (unstable) domains are located to the left (right) of the respective curves. For comparison we show the stability curve derived from Stocker and Schmittner (1997) (labelled 'S&S').

is 0.067 Sv/°C and for $m_{eq} = 30$ Sv h_2^{crit} is 0.122 Sv/°C, corresponding to critical freshwater fluxes of 0.13 Sv, 0.32 Sv and 0.59 Sv, respectively. In the cases $m_{eq} = 10-15$ Sv (not shown), the circulation collapses even without any additional freshwater input to the northern box, meaning that thermal forcing alone is sufficient to reverse the driving north-south density gradient.

So far one single attempt has been made to perform similar sensitivity experiments with a coupled ocean-atmosphere GCM (Tziperman 1997). The results, however, cannot be taken as benchmark for the behavior of the box model since the initial states prepared by Tziperman 1997 are physically not fully consistent (weaker THC states than today's with present-day observed sea surface temperature fields; see note by Rahmstorf and Ganopolski 1999b).

2.6 The effects of vertical and horizontal mixing

A number of studies have used three or four ocean boxes in one hemisphere, with a vertically stacked high latitude box (Huang et al. 1992; Tziperman et al. 1994; Griffies and Tziperman 1995; Gargett and Ferron 1996). In two hemispheres, such model setup would imply six or eight boxes, depending on whether the low-latitude box is split into a northern and a southern part or not (cf., e.g., Gildor and Tziperman 2001). The advantage of such model configurations is that they provide the opportunity to introduce additional physical processes, such as vertical diffusion and convection in the southern and northern boxes.

Concerning the southern box in our model, the subdivision into an upper and a lower part and the implementation of vertical mixing would not deliver new physical insights. The reason is that in the conception of the THC underlying the four-box model, box 1 represents the entire ocean south of the latitudes of the Cape of Good Hope, rather than the polar Southern

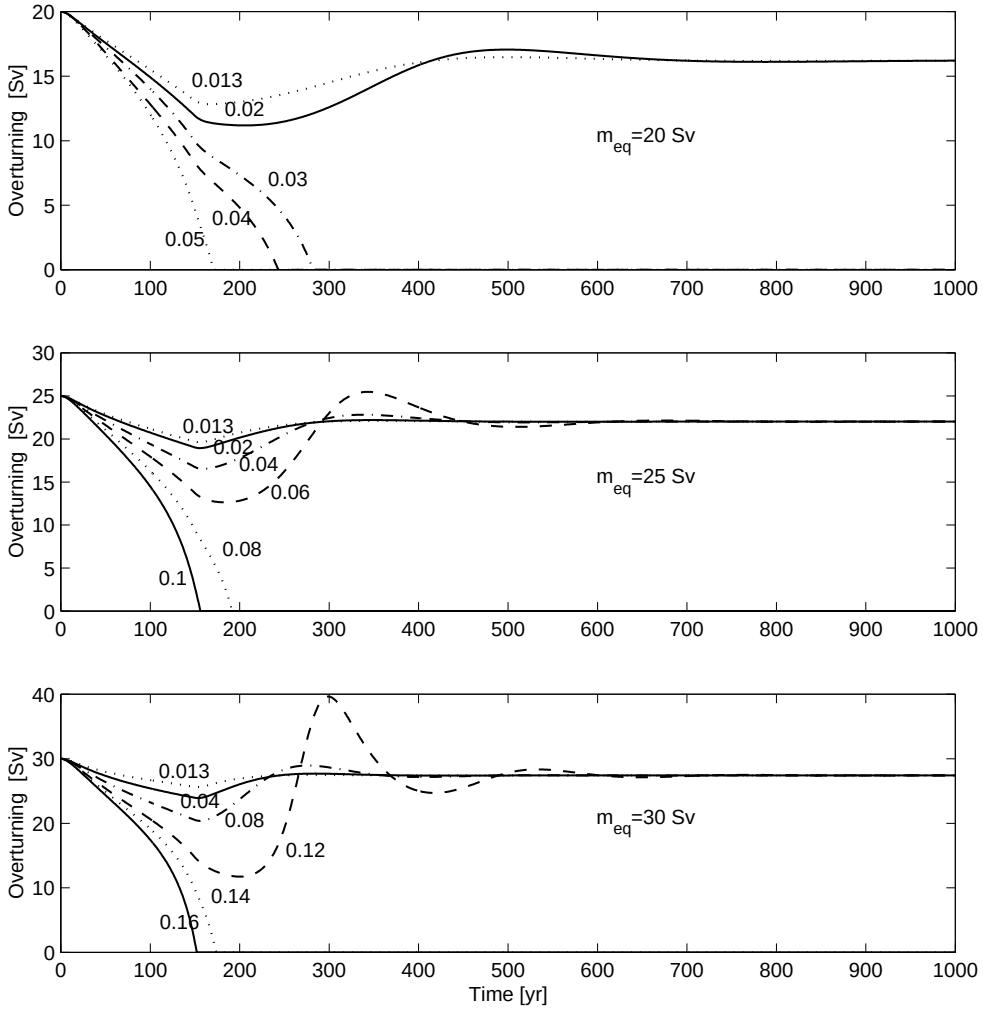

Figure 2.10: Response of the Atlantic overturning for different values of the initial overturning m_{eq} [Sv] and hydrological sensitivity h_2 [Sv/°C]. In the cases $m_{eq} = 10 - 15$ Sv (not shown) the circulation collapses already for $h_2 = 0$.

Ocean. Given that the heat forcing at the surface is chosen accordingly, and that the deep southern box would be filled with NADW, the vertical stratification of the water column would not become unstable, consistently with the absence of open-ocean deep convection in the real Southern Ocean. Also, vertical diffusion of the order of $10^{-4}\,\mathrm{m^2\,s^{-1}}$ would be small compared to the advective flux connecting lower and upper box (and mimicking upwelling). The split-up of the southern box would therefore merely amount to a redefinition of the box volumes, with NADW extending further south and the waters of southern origin being confined to the surface layer.

Also for the northern box, we don't expect the effects of the explicit representation of stratification and vertical mixing to be large. To test this conjecture, we subdivided the northern box in an upper and a lower part, and connected them by an advective (downward) and a diffusive (bidirectional) flux (cf. appendix A). In this model setup, convection is represented through the choice of the vertical diffusion coefficient, which is taken to be very

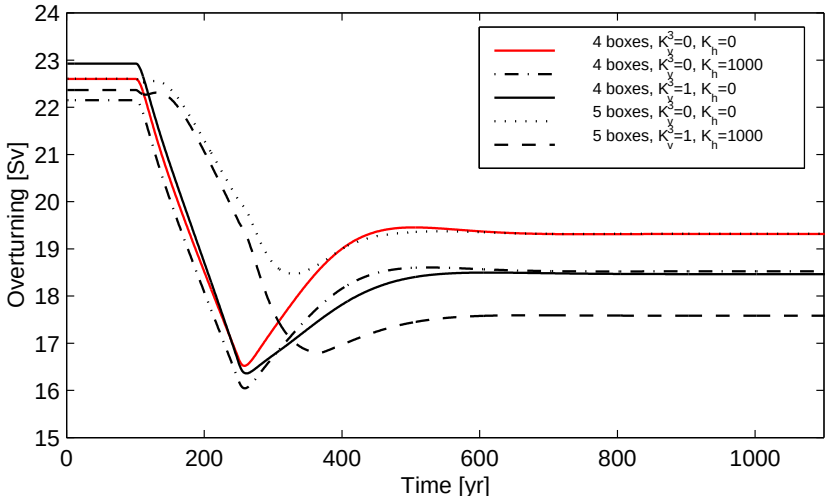

Figure 2.11: Response of the Atlantic overturning to the climate change scenario introduced in section 2.5 for different box configurations and different values of the vertical and horizontal mixing coefficients [$10^{-4}\,\mathrm{m^2\,s^{-1}}$]. The red curve depicts the response for standard model settings. Note that the climate change scenario is applied from year 100 on.

high for conditions of static instability of the water column and low for static stability, similarly to Shaffer and Olsen (2001) and Gildor and Tziperman (2001). This formulation is equivalent to the complete mixing of the water properties (i.e., heat and salt) of the two overlying boxes in the case of unstable stratification (Huang et al. 1992; Gargett and Ferron 1996). It should be noted, however, that the representation of convection in a coarse box model without implementation of the seasonal cycle is problematic. The reason is that in reality the convective events are spatially and temporally highly localized: they occur exclusively in winter, lasting but a few days, on spatial scales of 50–100 km.

In appendix A, we give the equations for the model version representing vertical and horizontal mixing explicitly. In the case of vertical mixing in the northern box alone (i.e., for K_v^3 and K_h equal to zero), it is easily inferred from Eqs. (A.5) and (A.10) that in equilibrium T_2 and S_2 equal T_5 and S_5, such that the vertical diffusion coefficient for the northern box, K_v^2, does not influence the strength of the overturning. Also the transient THC behavior remains largely unaffected by northern vertical mixing: the amount and time scale of the weakening and recovery of the overturning in response to the climate change scenario introduced in section 2.5 are not sensitive at all to the vertical mixing coefficient. The same applies to the value of the freshwater perturbation ΔF_2^{crit} that the overturning can sustain without collapsing. The reason for this insensitivity is that the stratification of the water column remains stable throughout the transient run, such that convection does not occur, and turbulent mixing of the order of $10^{-4}\,\mathrm{m^2\,s^{-1}}$ is small compared to the advective fluxes. The delay (by some decades) and reduction (by about 2 Sv) of the weakening of the overturning as compared to our standard model setup (compare the dotted and red lines in Fig. 2.11) is solely due to the split-up of the northern box in two parts.

A process neglected so far in our model is diapycnal mixing across the main thermocline. In order to estimate the error made by omitting this process, we introduced a vertical flux between box 3 and 4 (while retaining the four-box formulation). We found that the low-latitude diffusion coefficient (K_v^3; cf. appendix A) affects the equilibrium overturning only

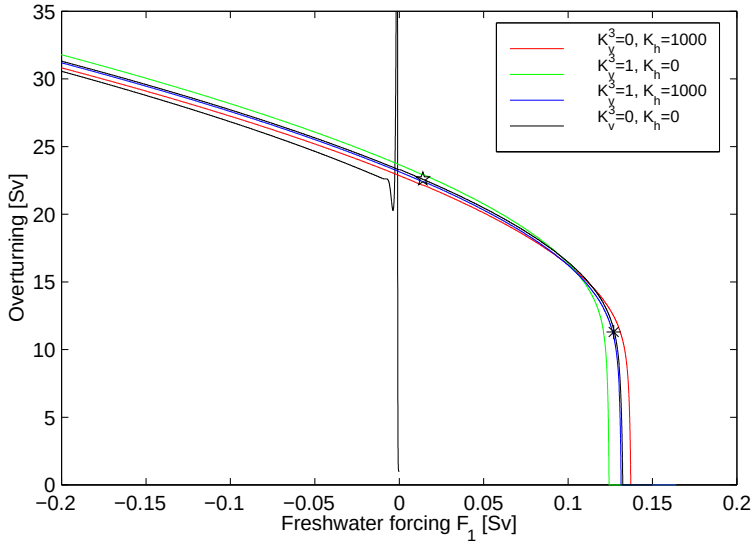

Figure 2.12: Upper branch of the hysteresis for different values of the vertical and horizontal diffusion coefficients [$10^{-4}\,\mathrm{m^2\,s^{-1}}$]. For reference, we display the full hysteresis curve calculated with our standard model setup. As in Fig. 2.2, the star and the asterisk denote the present-day overturning and the bifurcation point, respectively. Note that the hysteresis for $K_v^3 = 10^{-4}\ \mathrm{m^2\,s^{-1}}$, $K_h = 10^{-1}\ \mathrm{m^2\,s^{-1}}$ almost coincides with the hysteresis for the standard case ($K_v^3 = 0$, $K_h = 0$).

slightly: increasing K_v^3 from 0 to $10^{-4}\ \mathrm{m^2\,s^{-1}}$ leads to a strengthening of the overturning by 0.5 Sv. The reason for this slight increase is downward diffusion of heat and subsequent southward advection, which strengthens the meridional density gradient. Also, the response of the overturning to our standard climate change scenario changes only little if vertical diffusion is introduced: the amount and time scale of the weakening are almost the same, just the stabilization level decreases by about 1 Sv for values of the vertical diffusion coefficient of $10^{-4}\ \mathrm{m^2\,s^{-1}}$ (compare the red and solid lines in Fig. 2.11). As far as the sensitivity of the overturning to freshwater perturbation is concerned, it turns out that the critical freshwater forcing ΔF_2^{crit} decreases for non-zero values of the diffusion coefficient: for K_v^3 equal to $10^{-4}\,\mathrm{m^2\,s^{-1}}$ ΔF_2^{crit} is reduced by 30% compared to the case $K_v^3 = 0$. Note, however, that a diffusivity of $10^{-4}\,\mathrm{m^2\,s^{-1}}$ is at the high end of estimates of diffusion in the real ocean: measurements yield a value of about $10^{-5}\,\mathrm{m^2\,s^{-1}}$ at the thermocline (Ledwell et al. 1998). The reason for this stronger sensitivity is that in the presence of vertical diffusion the freshwater anomaly which is advected from the northern box towards the south mixes with high salinity water from the Tropics. As a consequence, the redistribution of the freshwater anomaly among the boxes, which acts to stabilize the overturning (cf. section 2.5.1), takes longer for higher values of K_v^3. Note that this result is in contrast to the findings of studies using two and three-dimensional ocean models (Schmittner and Weaver 2001; Prange et al. 2003), where the critical freshwater perturbation is found to increase significantly with the vertical diffusivity. The reason for this discrepancy is not clear.

Lastly, we augmented the four-box model with horizontal diffusion, which is meant to represent the mixing effects of the wind-driven circulation. This is achieved by introducing horizontal fluxes between adjacent boxes (cf. appendix A). As for vertical diffusion, the effects on the overturning are small. The equilibrium state decreases only slightly with increasing

horizontal diffusivity (by about 0.4 Sv for K_h equal to 10^{-1} m^2 s^{-1}), and the characteristics of the response curve remain essentially the same (compare the dashed-dotted and red lines in Fig. 2.11). The freshwater perturbation needed to shut down the circulation is unaffected by horizontal diffusion. A notable result is that the oscillations evident during the recovery phase of the overturning for values of h_2 close to critical (cf., e.g., Figs. 2.5 and 2.10) are more strongly damped for larger values of the horizontal diffusivity, as was conjectured in section 2.5.2.

What do the results discussed in this section imply in terms of the optimal fit to the CLIMBER-2 experiments? Given that the unperturbed equilibrium state is not affected at all by vertical mixing in the North and only slightly by vertical and horizontal diffusion across the low-latitude boxes, inclusion of these processes would change the parameters determined via a least-square fit to the CLIMBER-2 hysteresis only slightly (cf. Fig. 2.12). The parameter V_4, which was adjusted to match the critical freshwater perturbation ΔF_2^{crit} determined with CLIMBER-2, would change only in the case of vertical diffusion across the thermocline (recall that ΔF_2^{crit} remains largely unaffected by northern vertical mixing and horizontal diffusion): since vertical diffusion was found to increase the sensitivity of the circulation to freshwater perturbations, V_4 would have to be decreased further with increasing vertical diffusivity. These results suggest that the freedom gained by introducing the additional tunable parameters K_v^2, K_v^3 and K_h would not help to improve the fit to the transient CLIMBER-2 behavior.

In chapter 4, we present an integrated assessment application of the reduced-form THC model. A summary of the results presented in this chapter and the pertinent conclusions will be given in chapter 5.

Chapter 3

A reduced-form model of the Indian monsoon

3.1 Motivation

In this chapter, we present a novel reduced-form model of the Indian monsoon. It is conceived so as to fulfill the main requirements of integrated assessment (IA) modeling which have been extensively discussed in section 2.1. The reason for the ab initio development of such a tool is that models of adequate complexity do not exist. The simplest available models are of intermediate complexity (Neelin and Zeng 2000; Zeng et al. 2000) which, as outlined in section 2.1, are still too complex to be incorporated into IA frameworks.

As described in section 1.5, the Indian monsoon is a recurrent large-scale circulation pattern arising from the thermal contrast between the Asian continent and the Indian Ocean. Its dynamics involves complex interactions between ocean, land and atmosphere. The ocean, through sea surface temperature (SST) variations, plays a role in determining the monsoon circulation (Chandrasekar and Kitoh 1998; Li et al. 2001). Land processes, such as soil moisture, evapotranspiration and albedo (Meehl 1994; Claussen 1997; Chou et al. 2000) and topography, in particular the elevation of the Tibetan Plateau (Hahn and Manabe 1975; Yanai et al. 1992) influence the intensity and position of the monsoon. Further, the Indian monsoon is at the center of a web of important teleconnections: the summer (winter) monsoon links to the ascending (subsiding) branch of the meridional Hadley circulation (Webster et al. 1998). Also, monsoon precipitation shows significant correlation with the El Niño Southern Oscillation (ENSO), warm (cold) events in the eastern Pacific being associated with below (above) summer rainfall over India (Ju and Slingo 1995; Webster et al. 1998). The Eurasian snow cover was shown to influence the springtime temperature of the Asian continent and thereby the land-sea thermal contrast (Sankar-Rao et al. 1996).

By definition, a reduced-form model of the Indian monsoon cannot do justice to this complexity. We nevertheless demonstrate that despite its high degree of idealization, such a model is a useful tool for a) the investigation of the role of individual physical processes and feedback mechanisms in shaping the dynamics of the Indian monsoon, b) the exploration of the sensitivity of the monsoon to variations of parameters and boundary conditions, c) the realistic simulation of some highly aggregated measure of the intensity of the Indian monsoon, such as, for instance, rainfall averaged over India (All-India Rainfall; AIR).

In section 3.2, we describe the model in detail. In order to raise confidence in the ability

of the model to reproduce the observed dynamics, we discuss simulations of the annual cycle of the Indian monsoon (section 3.3). We proceed by presenting a reduction of the basic model to a form which can be treated analytically (section 3.4). The purpose of this reduction is the exploration of the system's joint phase and parameter space by means of well established methods of Nonlinear Dynamics such as analytical bifurcation analysis (Argyris et al. 1995). From this exercise, we expect to gain insight about changes in the qualitative behavior of the system, in particular the existence of parameter-dependent state-transitions ('bifurcations'). In section 3.5 we investigate the response of the basic model to changes in parameters and boundary conditions associated with anthropogenic greenhouse gases and aerosol emissions. The scope of these experiments is twofold: firstly, we intend to analyze the performance of the basic model under climate change by comparing our findings with those obtained with comprehensive climate models. Secondly, we aim at exploring whether plausible changes in the model parameters and boundary conditions may lead to a transgression of the bifurcation points identified in section 3.4.

3.2 Model description

From the available body of literature, the following elements can be identified as key 'ingredients' of a reduced-form model of the Indian monsoon:

- the temperature gradient between India and the adjacent Indian Ocean
- the hydrological cycle, including soil hydrological processes
- the large-scale circulation patterns, such as the Hadley and trade-wind circulations
- the Tibetan Plateau.

Key feedback processes that we aim at representing in the model include:

- the moisture advection feedback (Webster 1987; Webster et al. 1998) whereby the upper-level pressure gradient which drives the monsoon circulation is reinforced by the moisture the monsoon itself carries from the ocean (cf. section 1.5)
- the soil moisture feedback (Meehl 1994; Webster et al. 1998; Chou et al. 2000) whereby soil moisture influences the monsoon circulation via evapotranspiration
- the vegetation feedback (Claussen 1997), whereby the vegetation fraction determines the surface properties (i.e., albedo and roughness) and hence the monsoon circulation.

Conceptually, our model is similar to the box model developed by Brovkin et al. (1998) for the description of the climate-vegetation interaction in the Western Sahara during the African summer monsoon. Our model consists of one four-sided box which is delimited by the Indian Ocean at its western, southern and eastern boundaries and by the Tibetan Plateau at its northern boundary. In the vertical, the atmosphere is represented by three layers: the planetary boundary layer (PBL) with the surface layer at its lower boundary, the free troposphere and the stratosphere (cf. Fig. 3.1). The underlying land compartment is represented by two soil layers. The prognostic variables in the system are the near-surface air temperature and specific humidity, denoted by T_a and q_a, respectively, and the soil moisture in two layers (w_1, w_2). From these, all other variables (e.g., cloudiness, precipitation, evapotranspiration,

surface wind) are diagnosed. Inside the box, the variables are described in terms of their spatial averages. The only meridional and zonal gradients are those between the box interior (i.e., the Indian subcontinent) and its boundaries (i.e., the Indian Ocean and the Tibetan Plateau), whose climatic conditions are externally prescribed. The associated gradients drive the annual evolution of the local monsoon circulations. The large-scale Hadley and trade-wind circulations are prescribed.

3.2.1 Governing equations

The temporal evolution of the surface temperature T_a and the specific humidity q_a are computed from the vertically integrated energy and water balance equations:

$$\int_0^{H_a} c_p\,\rho\frac{\partial\theta}{\partial t}\,dz = \mathcal{L}C + H - F_{\downarrow}^{SL,S}\,(1-A_s) + F_{\uparrow}^{LW,S} - F_{\downarrow}^{LW,S} + \\ + F_{\downarrow}^{SL,TA}\,(1-A_{sys}) - F_{\uparrow}^{LW,TA} + A_T, \tag{3.1}$$

$$\int_0^{H_a} \rho\frac{\partial q}{\partial t}\,dz = E - C + A_v, \tag{3.2}$$

where $\theta = T(z) + \Gamma_a z$ denotes the potential temperature and Γ_a the adiabatic lapse rate in the atmosphere. $q = q(z)$ is the vertical profile of specific humidity. The terms on the right hand side of the equations denote the following fluxes and sources/sinks:

C: Condensation rate,

H: Sensible heat flux at the surface,

A_T: Horizontal advection of heat,

$F_{\downarrow}^{SL,S}$: Downward solar radiation at the surface,

$F_{\uparrow}^{LW,S}$, $F_{\downarrow}^{LW,S}$: Upward and downward longwave radiation at the surface,

$F_{\downarrow}^{SL,TA}$: Incident solar radiation at the top of the atmosphere,

$F_{\uparrow}^{LW,TA}$: Outgoing longwave radiation at the top of the atmosphere,

A_s, A_{sys}: Surface and planetary albedos,

E: Evapotranspiration,

A_v: Horizontal advection of moisture.

Further, H_a denotes the height of the atmosphere, $\rho = \rho(z)$ the air density. c_p is the specific heat of air at constant pressure and $\mathcal{L}$ the latent heat of evaporation.

The surface temperature T_s can be computed from the energy balance equation at the surface:

$$h_s c_s \frac{\partial T_s}{\partial t} = -H + F_{\downarrow}^{SL,S}\,(1-A_s) - F_{\uparrow}^{LW,S} + F_{\downarrow}^{LW,S} - \mathcal{L}E, \tag{3.3}$$

where h_s refers to the depth of the upper soil layer (which is assumed to correspond to the $1/e$ damping depth for the annual thermal wave) and c_s to the heat capacity per unit soil

volume, respectively. Note that the latter increases along with the water content of the soil (cf. Dickinson et al. 1986).

For the sake of simplicity, we approximate the rate of change of T_s with the rate of change of the surface air temperature T_a: $\partial T_s/\partial t \approx \partial T_a/\partial t$. This approximation allows one to summarize Eqs. 3.1 and 3.3 into a single expression:

$$\int_0^{H_a} c_p\,\rho\frac{\partial\theta}{\partial t}\,dz + h_s c_s\frac{\partial T_a}{\partial t} = \mathcal{L}\,(C-E) + F_{\downarrow}^{SL,TA}\,(1-A_{sys}) - F_{\uparrow}^{LW,TA} + A_T, \tag{3.4}$$

where $c_p\int_0^{H_a}\rho\,dz + h_s c_s$ can be interpreted as the 'effective' heat capacity of the surface plus atmosphere system. Note that in the simplified Eq. 3.4 all surface fluxes except evapotranspiration cancel out, such that the neglect of the surface temperature feedbacks has only a minor effect on the system's behavior.

The soil moisture (which determines evapotranspiration) is described explicitly according to a two-layer model (Hansen et al. 1983), whereby the water content of the upper layer responds to evapotranspiration and precipitation and the lower layer acts as a reservoir. The rates of change of moisture in the two soil layers are:

$$\frac{\partial w_1}{\partial t} = \frac{P-E-R}{f_1} - \frac{w_1-w_2}{\tau}, \tag{3.5}$$

$$\frac{\partial w_2}{\partial t} = \frac{f_1}{f_2}\frac{w_1-w_2}{\tau}, \tag{3.6}$$

where the wetness of the i^{th} layer w_i is the ratio of available water to field capacity f_i (i.e., the total water content of the soil at saturation, which is a function of soil type and vegetation). Further, P is precipitation, R the surface runoff and τ the time constant for diffusion of moisture between the two layers.

3.2.2 Vertical structure of the atmosphere

The basic elements of the vertical structure of the atmosphere are depicted in Fig. 3.1. The vertical temperature profile is assumed to be linear in the troposphere and constant in the stratosphere, the latter being in radiative equilibrium:

$$T(z) = \begin{cases} T_a - \Gamma\,z, & \text{if} \quad 0 < z < H_t \\ T_a - \Gamma\,H_t, & \text{if} \quad H_t < z < H_a \end{cases} \tag{3.7}$$

where H_t is the height of the troposphere and Γ the atmospheric lapse rate. The latter is a function of the temperature T_a, the specific humidity q_a and the cumulus cloud amount N_{cu} and is described according to the approach developed in Petoukhov et al. (2003):

$$\Gamma = \Gamma_0 + \Gamma_1\,(T_a - T_0)\left(1 - a_q\,q_a^2\right) - \Gamma_2\,N_{cu}. \tag{3.8}$$

Γ_0, Γ_1, Γ_2, a_q are assigned constant values which are listed in Table 3.1. T_0 denotes the reference temperature. The specific humidity q is assumed to follow an exponential vertical profile (Petoukhov et al. 2003):

$$q(z) = q_a\,\exp\left(-\frac{z}{H_e}\right), \tag{3.9}$$

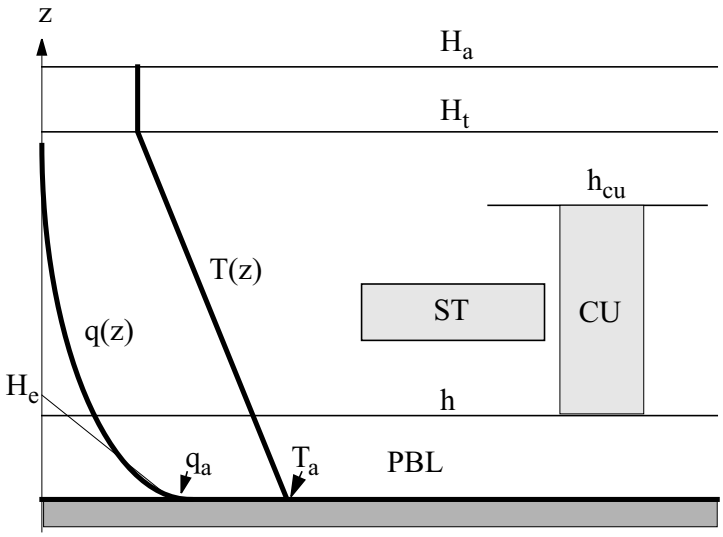

Figure 3.1: Parameterization of the vertical structure of the atmosphere.

where H_e is the water vapor scale height. The air density is described in the inelastic approximation as (Petoukhov et al. 2003):

$$\rho(z) = \rho_0 \exp\left(-\frac{z}{H_0}\right), \tag{3.10}$$

where ρ_0 is the reference air density, $H_0 = RT_0/g$ the density scale height, R the gas constant for dry air and g the acceleration due to gravity.

3.2.3 Surface wind

The total wind velocity at the surface, v_0, is given as the sum of the intensity of the monsoon circulations $u^0_{m,i}$ across each of the four box boundaries ($i \in \{W, S, E, N\}$), the zonal wind u^0_{tr} and the Hadley circulation v^0_H:

$$v_0 = \left(\sum_i \left(u^0_{m,i}\right)^2 + (u^0_{tr})^2 + (v^0_H)^2\right)^{1/2}. \tag{3.11}$$

The terms u^0_{tr} and v^0_H are prescribed according to observational data (cf. Table 3.3), whereas the surface monsoon circulations $u^0_{m,i}$ are calculated explicitly.

The $u^0_{m,i}$ are proportional to the sea-level pressure gradient $\nabla\, p_i$ between the Indian subcontinent and the respective boundary (i.e., the Indian Ocean to the west, south and east and the Tibetan plateau to the north):

$$u^0_{m,i} = \frac{\sin(\alpha_0)}{\rho_0\, f}\, \nabla\, p_i \tag{3.12}$$

where $\sin(\alpha_0)$ is the cross-isobar angle and $f = 2\,\omega\,\sin(\phi_0)$ the Coriolis parameter. Assuming $\nabla\, p_i = -(g p_0 H_t / 2RT_0^2)\nabla\, T_i$ (cf. Petoukhov et al. 2000), where $p_0 = \rho_0 RT_0$ and T is the

sea-level temperature, the $u^0_{m,i}$ across the three oceanic boundaries can be approximated by:

$$u^0_{m,i} = \frac{\sin(\alpha_0)\, g\, p_0\, H_t}{\rho_0\, f\, 2\, R\, T_0^2\, \Delta L}(T_a - T_i). \tag{3.13}$$

Here ΔL denotes the width of the (quadratic) box representing the Indian subcontinent and T_i the temperature at the i^{th} boundary ($i \in \{W, S, E\}$). For the monsoon circulation across the northern boundary, Eq. 3.13 takes a slightly different form which accounts for the difference in surface elevation between the Indian peninsula and the Tibetan plateau:

$$u^0_{m,N} = \frac{\sin(\alpha_0)_{tib}\, g\, p_0\, (H_t - H_{tib})}{\rho_0\, f\, 2\, R\, T_0^2\, \Delta L}\, (T(H_{tib}) - T_N)\,, \tag{3.14}$$

where $T(H_{tib})$ denotes the air temperature at the height of Tibet (H_{tib}) and $\sin(\alpha_0)_{tib}$ the cross-isobar angle for Tibet.

The cross-isobar angle $\sin(\alpha_0)$ is determined from the condition that the shear stress be continuous between the Ekman layer and the surface layer (Petoukhov et al. 2000). It is a function of the PBL kinematic vertical viscosity K, the depth of the surface layer z_s, the surface roughness z_0, and the mean wind speed at the upper boundary of the PBL $\bar{u}(h)$:

$$\sin(\alpha_0) = \left(2 + \sqrt{2\, f\, K}\, \frac{\ln^2 \frac{z_s}{z_0}}{\kappa^2\, |\bar{u}(h)|}\right)^{-1}, \tag{3.15}$$

where κ is von Kármán's constant. For Tibet, the cross-isobar angle is calculated in the same way, but with z_{tib} instead of z_0 (since the surface roughness depends on large-scale topography) and K_{tib} instead of K.

The vertical kinematic viscosity K is again a function of z_s and z_0:

$$K = C_k \frac{\kappa^2}{\ln^2 \frac{z_s}{z_0}}, \tag{3.16}$$

where C_k is a parameter listed in Table 3.1. It takes different values depending on whether the vertical velocity is positive or negative. The quantity $\kappa^2 / \ln^2(z_s/z_0)$ is referred to as the 'drag coefficient' (C_D). K_{tib} is also obtained according to Eq. 3.16 but with z_{tib} instead of z_0.

In the model, z_0 is a combination of the roughness of the surface covered by vegetation and the roughness of the bare soil. This is accounted for by aggregating the drag coefficients for bare and vegetated soil (Claussen 1991):

$$\left(\ln^2 \frac{z_s}{z_0}\right)^{-1} = V \left(\ln^2 \frac{z_s}{z_v}\right)^{-1} + (1 - V) \left(\ln^2 \frac{z_s}{z_b}\right)^{-1}, \tag{3.17}$$

where V is the fractional vegetation cover (i.e., the fraction of the land surface covered by vegetation), z_v is the roughness length of vegetated and z_b that of bare soil.

V is calculated according to Brovkin et al. (1998) as a hyperbolic function of precipitation P:

$$V = \begin{cases} 0 & \text{if} \quad P < P_{cr} \\ 1 - \frac{1}{1 + a_v (P - P_{cr})^2} & \text{otherwise} \end{cases}, \tag{3.18}$$

where P_{cr} is a threshold value of annual mean precipitation below which the vegetation cover cannot be sustained in the long term. a_v is a parameter.

3.2.4 Vertical velocity

The vertical velocity w at the upper boundary of the PBL is derived from the continuity equation as the sum of the contributions due to the monsoon and the Hadley circulations (the trade winds do not contribute to w since they are homogenous across India):

$$w = \left(\sum_i u^0_{m,i} + v^0_H \right) \frac{h}{\Delta L}. \tag{3.19}$$

Finally, the vertical depth of the PBL h is described according to Petoukhov et al. (2000) as:

$$h = C_h \left(\frac{2K}{|f|} \right)^{1/2}, \tag{3.20}$$

where K is the vertical kinematic viscosity introduced in the previous section and C_h is a constant listed in Table 3.1. Note that similarly to C_K, C_h takes different values depending on the sign of the vertical velocity.

3.2.5 Hydrological cycle

Evapotranspiration E is described as the sum of evaporation from bare soil E_b and transpiration from vegetated soil E_v:

$$E = (1 - V)E_b + VE_v. \tag{3.21}$$

E_b is described in the bulk transfer approach as (Hansen et al. 1983):

$$E_b = \rho_0 \, C^b_D \, v_0 \, w_1 \, (q_s - q_a) \, . \tag{3.22}$$

Here C^b_D is the drag coefficient for bare soil (i.e., $C^b_D = \kappa^2 / \ln(z_s/z_b)^2$) and q_s the specific humidity at the surface. We approximate the latter by the saturation specific humidity at $T = T_s$ and $p = p_0$, $q_{sat}(T_s, p_0)$, which is calculated by means of the Clausius-Clapeyron equation (Peixoto and Oort 1992). The effective transpiration from vegetated soil E_v is given as the product of potential transpiration E^{max}_v and a factor depending on soil type, soil moisture and vegetation characteristics (i.e., the root fraction f^i_r and the wilting point p^i_w in the i^{th} soil layer) (Dickinson et al. 1986):

$$E_v = E^{max}_v \left(f^1_r \left(1 - p^1_w \right) + f^2_r \left(1 - p^2_w \right) \right). \tag{3.23}$$

The wilting points p^1_w, p^2_w are parameterized as (Dickinson et al. 1986):

$$p^i_w = \begin{cases} 1 & \text{if} \quad w_i < w_0 \\ \frac{w_i^{-B} - 1}{w_0^{-B} - 1} & \text{otherwise} \end{cases} \tag{3.24}$$

where w_0 and B are parameters listed in Table 3.1. E^{max}_v is calculated in the same way as E_b (i.e., according to Eq. 3.22), but with the drag coefficient C^v_D (which is a function of the roughness of vegetated soil z_v) instead of C^b_D.

Following Petoukhov et al. (2000), the precipitation P is described as:

$$P = \frac{N}{\tau_P} \int_0^{H_t} \rho \, q \, dz, \tag{3.25}$$

	Parameter	Value	Unit
	Fixed parameters		
ρ_0	reference air density	1.29	$\mathrm{kg\,m^{-3}}$
T_0	reference air temperature	273.2	K
Γ_a	dry adiabatic lapse rate	$9.8{\cdot}10^{-3}$	$\mathrm{K\,m^{-1}}$
$q_{sat}(T_0)$	saturation specific humidity at T_0, p_0	$3.808{\cdot}10^{-3}$	$\mathrm{kg\,kg^{-1}}$
H_a	height of the atmosphere	$30{\cdot}10^{3}$	m
H_e	specific humidity scale height	$2{\cdot}10^{3}$	m
h_s	damping depth of thermal wave in soil layer	4	m
Γ_0	lapse rate coefficient	$6{\cdot}10^{-3}$	$\mathrm{K\,m^{-1}}$
Γ_1	lapse rate coefficient	$5.5{\cdot}10^{-5}$	$\mathrm{m^{-1}}$
Γ_2	lapse rate coefficient	$1{\cdot}10^{-3}$	$\mathrm{K\,m^{-1}}$
a_q	lapse rate coefficient	$1{\cdot}10^{3}$	$\mathrm{kg^2\,kg^{-2}}$
τ_0	characteristic precipitation time	$5{\cdot}10^{5}$	s
z_s	surface layer height	20	m
z_v	roughness length of vegetated soil	0.1	m
z_b	roughness length of bare soil	0.004	m
z_{tib}	roughness length for Tibet	1.5	m
b_1	cumulus cloudiness parameter	$1.5{\cdot}10^{-3}$	$\mathrm{m\,s^{-1}}$
b_2	cumulus cloudiness parameter	$30{\cdot}10^{-3}$	$\mathrm{kg\,kg^{-1}}$
a_1	stratus cloudiness parameter	0.8	1
a_2	stratus cloudiness parameter	0.1	1
a_3	stratus cloudiness parameter	$1{\cdot}10^{-3}$	$\mathrm{m\,s^{-1}}$
τ	soil moisture diffusion specific time	$17.28{\cdot}10^{4}$	s
f_1	field capacity of upper soil layer	24	$\mathrm{kg\,m^{-2}}$
f_2	field capacity of lower soil layer	120	$\mathrm{kg\,m^{-2}}$
w_0	soil moisture at which transpiration ceases	0.332	1
B	exponent for determination of wilting point	6	1
f_r^1	root fraction in upper soil layer	0.75	1
f_r^2	root fraction in lower soil layer	0.25	1
P_{cr}	critical precipitation for determination of V	$3.5{\cdot}10^{3}$	$\mathrm{kg\,m^{-2}\,s^{-1}}$
a_v	coefficient for determination of V	$9{\cdot}10^{9}$	$\mathrm{s^2\,m^4\,kg^{-2}}$
$\lvert\bar{u}(h)\rvert$	mean zonal wind velocity at h	2.4	$\mathrm{m\,s^{-1}}$
A_{00}	parameter of Budyko formula	231	$\mathrm{W\,m^{-2}}$
B_{00}	parameter of Budyko formula	2.1	$\mathrm{W\,m^{-2}\,K^{-1}}$
C_{00}	parameter of Budyko formula	59	$\mathrm{W\,m^{-2}}$
D_{00}	parameter of Budyko formula	0.65	$\mathrm{W\,m^{-2}\,K^{-1}}$
η	CO_2 sensitivity parameter	0.04	1
pCO_2^0	reference CO_2 concentration	325	ppm
pCO_2	present-day volume concentration of CO_2	360	ppm
	Tunable parameters		
C_k^1	constant for determination of K for $w > 0$	5	1
C_k^2	constant for determination of K for $w < 0$	1.5	1
C_h^1	constant for determination of h for $w > 0$	4	1
C_h^2	constant for determination of h for $w < 0$	0.4	1
N_{cu}^0	reference cumulus cloud amount	0.7	1
K_r	runoff parameter	0.4	1
K_{ent}	cumulus clouds entrainment factor	0.7	1

Table 3.1: Thermodynamical parameters of the monsoon model. Note that in tuning the model, we treat the parameterizations taken from other studies as fixed, and vary only the parameters that are truly unknown ('tunable parameters').

where N is the total cloud amount and τ_P the turnover time of water in the atmosphere which is a function of the vertical velocity w:

$$\tau_P = \tau_0 \left(1 - a_\tau \, 0.5 \left(1 + \tanh\left(\frac{w}{a_3}\right)\right)\right). \tag{3.26}$$

Here τ_0, a_τ and a_3 are parameters. Condensation C is assumed to be equal to precipitation:

$$C = P. \tag{3.27}$$

The surface runoff R is computed according to Hansen et al. (1983) as a function of precipitation and moisture of the upper soil layer w_1:

$$R = K_r \, P \, w_1, \tag{3.28}$$

whereby K_r is the proportionality constant.

3.2.6 Clouds

Two types of clouds are considered in the model: large-scale stratus and cumulus clouds. Stratus cloud cover is assumed to be dependent on relative humidity $q_a/q_{sat}(T_a, p_0)$, where $q_{sat}(T_a, p_0)$ is the saturation specific humidity at the temperature T_a and pressure p_0, and vertical velocity w (Petoukhov et al. 2000):

$$N_{st} = \left(\frac{q_a}{q_{sat}(T_a, p_0)}\right)^{1.5} \left(a_1 + a_2 \, 0.5 \left(\frac{w}{a_3}\right)\right). \tag{3.29}$$

Here the a_1, a_2, a_3 are parameters given in Table 3.1. The fraction of cumulus clouds is described as a function of the surface specific humidity and vertical velocity (Petoukhov et al. 2000):

$$N_{cu} = \begin{cases} N_{cu}^0 \, \tanh\left(\frac{w}{b_1}\right) \tanh\left(\frac{q_a}{b_2}\right), & \text{if} \quad w \geq 0 \\ 0 & \text{if} \quad w < 0 \end{cases} \tag{3.30}$$

where N_{cu}^0, b_1 and b_2 are parameters. The total cloudiness N is finally obtained as the superposition of stratus and cumulus cloud amount:

$$N = 1 - (1 - N_{cu})(1 - N_{st}). \tag{3.31}$$

The height of the cumulus clouds h_{cu} (which is needed for the determination of the optical properties of cumuli) is computed as the product of the potential height h_{cu}^{max} and a so-called 'entrainment' factor K_{ent}:

$$h_{cu} = h_{cu}^{max} \, K_{ent}. \tag{3.32}$$

The potential height is determined from the condition that the moist static energy E_{ms} of an ascending air parcel be conserved between the condensation level z_c and the height h_{cu}^{max}. With $E_{ms}(z) = c_p T(z) + gz + \mathcal{L} q_{sat}(T(z), p(z))$ (i.e., the sum of internal, potential and latent energy; cf. Peixoto and Oort 1992) this condition is expressed as:

$$c_p \, T\,(h_{cu}^{max}) + g \, h_{cu}^{max} + \mathcal{L} \, q_{sat}(T(h_{cu}^{max}), p(h_{cu}^{max})) = c_p \, T(z_c) + g \, z_c + \mathcal{L} \, q_a. \tag{3.33}$$

Note that per definition $q_{sat}(T(z_c), p(z_c)) = q_a$. With the Clausius-Clapeyron equation $q_{sat}(T, p) = q_{sat}(T_0) \, exp\,(0.622 \, \mathcal{L}\,(T - T_0)/R/T/T_0) p_0/p$ this condition allows one to determine the condensation temperature T_c (i.e., the temperature at which an ascending air parcel with humidity q_a condensates) and with it z_c (since $z_c = (T_a - T_c)/\Gamma_a$).

3.2.7 Solar radiation and planetary albedo

The downward solar radiation at the top of the atmosphere $F_{\downarrow}^{SL,TA}$ is a function of the solar constant I_0 and the solar zenith angle ξ:

$$F_{\downarrow}^{SL,TA} = I_0 \cos\xi \,. \tag{3.34}$$

The planetary albedo A_{sys} is given as the sum of the albedos of stratus clouds, cumulus clouds and the clear-sky atmosphere:

$$A_{sys} = N_{st}\, A_{st}^{p} + N_{cu}\, A_{cu}^{p} + N_{cs}\, A_{cs}^{p}, \tag{3.35}$$

where $N_{cs} = 1 - N$ and the A_i^p with $i \in \{st, cu, cs\}$ are functions of the respective albedos A_i and the surface albedo A_s (Liou 1980):

$$A_{st}^{p} = (A_{st} + (1 - A_{st})^2\, A_s)\, P_{cl} \tag{3.36}$$
$$A_{cu}^{p} = (A_{cu} + (1 - A_{cu})^2\, A_s)\, P_{cl} \tag{3.37}$$
$$A_{cs}^{p} = (A_{cs} + (1 - A_{cs})^2\, A_s)\, P_{cs}. \tag{3.38}$$

Here P_{cl} and P_{cs} are the integral transmission functions for solar radiation in the cloudy and clear sky atmosphere, respectively.

The albedo of stratus clouds A_{st} is calculated as:

$$A_{st} = b_{cl} \frac{(\tau_{st})^{k_\tau}}{(\cos\xi)^{m_{cl}}}, \tag{3.39}$$

where τ_{st} is the optical thickness of stratus clouds (which is assumed constant), b_{cl} is the albedo of the semi-infinite cloud at $\xi = 0$ and k_τ, m_{cl} are cloud droplets parameters. Accordingly, the albedo of cumulus clouds A_{cu} is derived as:

$$A_{cu} = b_{cl} \frac{(\tau_{cu})^{k_\tau}}{(\cos\xi)^{m_{cl}}}, \tag{3.40}$$

where the optical thickness τ_{cu} is a function of cumulus cloud amount N_{cu} and height h_{cu}:

$$\tau_{cu} = \sigma_0\, h_{cu}\, W_{cu}^{0}\, (N_{cu})^{k_w}. \tag{3.41}$$

σ_0 is the cloud droplets extinction coefficient and $W_{cu}^{0}\,(N_{cu})^{k_w}$ the cumulus liquid water content, k_w being a constant parameter. The albedo of the clear sky atmosphere A_{cs} is calculated as:

$$A_{cs} = \frac{b_{cs}}{(\cos\xi)^{m_{cs}}}. \tag{3.42}$$

The parameters b_{cs} and m_{cs} are listed in Table 3.2.

The surface albedo A_s is computed as the weighted sum of the albedos of vegetated and bare soil, A_v and A_b, respectively:

$$A_s = V\, A_v + (1 - V)\, A_b. \tag{3.43}$$

Both A_v and A_b consist of a component in the ultraviolet/visible and in the infrared band of the solar spectrum:

$$A_v = K_a^{vis}\, A_v^{vis} + \left(1 - K_a^{vis}\right)\, A_v^{ir} \tag{3.44}$$
$$A_b = K_a^{vis}\, A_b^{vis} + \left(1 - K_a^{vis}\right)\, A_b^{ir}, \tag{3.45}$$

where K_a^{vis} is the relative weight of the ultraviolet plus visible radiation in the total solar spectrum. The visible and infrared albedos of vegetated soil, A_v^{vis} and A_v^{ir}, are constants whereas A_b^{vis} and A_b^{ir} are functions of the water content of the upper soil layer w_1 (Dickinson et al. 1986):

$$A_b^{vis} = \begin{cases} A_b^{sat} + \Delta A_b(w_1) & \text{if} \quad \Delta A_b(w_1) > 0 \\ A_b^{sat} & \text{otherwise} \end{cases} \tag{3.46}$$

$$A_b^{ir} = 2\, A_b^{vis}, \tag{3.47}$$

where A_b^{sat} is the albedo of the saturated soil and $\Delta A_b(w_1) = 0.01\,(11 - 40\, w_1\, f_1\, 10^3/z_1)$ the increase in the albedo due to dryness of the soil, z_1 being the depth of the upper soil layer.

3.2.8 Long-wave radiation

The outgoing long-wave radiation at the top of the atmosphere $F_\uparrow^{LW,TA}$ is described according to the Budyko (1982) formula as a function of the temperature at the surface T_a and cloudiness N:

$$F_\uparrow^{LW,TA} = A_0 + B_0\,(T_a - T_0) - N\,(C_0 + D_0\,(T_a - T_0))\,, \tag{3.48}$$

where the coefficients $X_0 \in \{A_0, B_0, C_0, D_0\}$ are functions of the actual CO_2 concentration pCO_2:

$$X_0 = X_{00}\left(1 - \eta\, \ln\left(\frac{pCO_2}{pCO_2^0}\right)\right). \tag{3.49}$$

The parameters pCO_2^0, A_{00}, B_{00}, C_{00}, D_{00} and η are listed in Table 3.1.

3.2.9 Advection of heat and moisture

The total fluxes of heat and moisture due to horizontal advection, A_T and A_v, are the sum of the contributions from the monsoon circulation, the Hadley cell and the zonal wind:

$$A_T = \sum_i A_T^{m,i} + A_T^H + A_T^{tr}, \tag{3.50}$$

$$A_v = \sum_i A_v^{m,i} + A_v^H + A_v^{tr}. \tag{3.51}$$

We start with the description of the advection associated with the monsoon circulation. In summer, when the land is warmer than the adjacent oceans, i.e. $T_a > T_i$, the surface monsoon circulations $u_{m,i}^0$ are directed from the ocean towards the Indian peninsula. Above the monsoon turning height h_m, they are compensated by opposite return flows $u_{m,i}^1$. In winter, i.e. for $T_a < T_i$, the monsoon cells are reversed. For the summer monsoon, the terms $A_T^{m,i}$ are described as (Petoukhov et al. 2000):

$$A_T^{m,i} = \frac{c_p\, L}{S}\left[\int_0^{h_m} u_{m,i}(z)\, \rho\, \theta(T_i)\, dz + \int_{h_m}^{H_t} u_{m,i}(z)\, \rho\, \theta\,(T_a)\; dz\right]. \tag{3.52}$$

Here $\theta(T_i)$ is the potential temperature at the i^{th} boundary and $\theta(T_a)$ that over India. L denotes the width and S the area of the box. For the sake of simplicity, we assume h_m to coincide with the depth of the PBL, h, an approximation supported by empirical evidence. Further, we take the vertical profile of the monsoon winds to be independent of height above

	Parameter	Value	Unit
	Physical constants		
g	gravity constant	9.81	$\mathrm{m\,s^{-2}}$
R	gas constant for dry air	287	$\mathrm{m^2\,s^{-1}\,K^{-1}}$
c_p	specific heat of air at constant pressure	1000	$\mathrm{J\,kg^{-1}\,K^{-1}}$
$\mathcal{L}$	latent heat of evaporation	$2.5{\cdot}10^6$	$\mathrm{J\,kg^{-1}}$
I_0	solar constant	1365	$\mathrm{W\,m^{-2}}$
ω	earth rotation angular velocity	$7.4{\cdot}10^{-5}$	$\mathrm{rad\,s^{-1}}$
κ	von Kármán's constant	0.4	1
	Fixed parameters		
L	box width	$1.5{\cdot}10^6$	m
H_{tib}	height of the Tibetan Plateau	$3.5{\cdot}10^3$	m
ϕ_0	mean latitude of India	20	°N
b_{cl}	albedo of the semi-infinite cloud at $\xi = 0$	0.0475	1
k_τ	cloud albedo parameter	2/3	1
m_{cl}	cloud albedo parameter	0.82	1
σ_0	cloud droplets extinction coefficient	0.3	$\mathrm{m^2\,g^{-1}}$
W_{cu}^0	reference liquid water content	0.05	$\mathrm{g\,m^{-3}}$
k_w	parameter for determination of optical thickness of cumuli	1.5	1
b_{cs}	clear-sky albedo at $\xi = 0$	0.05	1
m_{cs}	clear-sky albedo parameter	1	1
A_v^{vis}	albedo of vegetated soil (UV/visible radiation)	0.08	1
A_v^{ir}	albedo of vegetated soil (IR radiation)	0.28	1
A_b^{sat}	albedo of saturated bare soil for UV/visible radiation	0.09	1
K_a^{vis}	relative weight of UV/visible radiation in solar spectrum	0.58	1
	Tunable parameters		
H_t	height of the troposphere	$14{\cdot}10^3$	m
P_{cl}	integral transmission function in cloudy atmosphere	0.97	1
P_{cs}	integral transmission function in clear-sky atmosphere	0.8	1
τ_{st}	optical thickness of stratus clouds	7.5	1

Table 3.2: Physical constants, geometrical and optical parameters of the monsoon model.

and below the turning height h, so that $u_{m,i}(z) = u_{m,i}^0$ for $z < h$ and $u_{m,i}(z) = u_{m,i}^1$ for $z > h$. The $u_{m,i}^1$ are derived through the continuity equation:

$$u_{m,i}^1 \int_h^{H_t} \rho \, dz = u_{m,i}^0 \int_0^h \rho \, dz. \tag{3.53}$$

Note that for the northern boundary, Eq. 3.52 takes a slightly different form due to the difference in surface elevation between the Indian subcontinent and the Himalayas (the integration limits are to be substituted with H_{tib}, $H_{tib} + h_{tib}$ in the first and $H_{tib} + h_{tib}$, H_t in the second integral). For the winter monsoon ($T_a < T_i$), the $A_T^{m,i}$ are computed similarly to Eq. 3.52 but with $\theta(T_i)$ in the place of $\theta(T_a)$ and viceversa.

As in the case of heat advection, we describe the monsoonal advection of moisture for summer conditions as:

$$A_v^{m,i} = \frac{L}{S}\left[u_{m,i}^0 \int_0^h \rho \, q_i \, dz + u_{m,i}^1 \int_h^{H_t} \rho \, q_a \, dz\right], \tag{3.54}$$

where q_i is the specific humidity at the i^{th} boundary, and is calculated as the product of the the relative humidity f_i and the saturation specific humidity at T_i. For the description of advection of moisture under winter monsoon conditions and for Tibet we proceed as above for the advection of heat.

Similarly to the monsoon, the large-scale meridional Hadley circulation reverses its direction in the course of the year, with northward surface flow ($v_H^0 > 0$) in summer and southward flow in winter (and opposite return flow v_H^1 at upper levels). Due to the similarity with the monsoon, we give the expression for the advection of heat associated with the Hadley cell for summer conditions only:

$$A_T^H = \frac{c_p\, L}{S}\left[v_H^0 \int_0^{h_H} \rho\, \theta(T_S)\, dz + v_H^1 \int_{h_H}^{H_t} \rho\, \theta\left(T_a\right)\, dz\right]. \tag{3.55}$$

Here $\theta(T_S)$ denotes the potential temperature at the southern boundary and h_H the Hadley circulation turning height. The latter, as well as v_H^0 and v_H^1, is exogenously prescribed (cf. Table 3.3). A_v^H is computed similarly to A_T^H, with q_S and q_a instead of $\theta(T_S)$ and $\theta(T_a)$.

The upper tropospheric zonal wind is westerly in winter, with a strong maximum (u_{tr}^{max}) at approximately 12 km and a linear decrease with height. Below the zonal wind turning height h_{tr} the circulation is easterly. In summer, the zonal wind is reversed, but the circulation maximum in the upper troposphere is much less pronounced. We approximate the vertical profile of the zonal wind by a linear law ($u_{tr}(z) = u_{tr}^{max}\,(z - h_{tr})/(H_t - h_{tr})$) and prescribe the seasonal course of u_{tr}^{max} and h_{tr} according to observational data (cf. Table 3.3). In contrast to the monsoon and the Hadley circulation, the zonal wind blows homogeneously over India (i.e., without air ascent). For winter zonal wind conditions ($u_{tr}^{max} > 0$) the advection of heat is therefore described as:

$$A_T^{tr} = \frac{c_p\, L}{S}\left[\int_0^{h_{tr}} |u_{tr}|\, \rho\left(\theta(T_E) - \theta(T_a)\right)\, dz + \int_{h_{tr}}^{H_t} |u_{tr}|\, \rho\left(\theta(T_W) - \theta(T_a)\right)\, dz\right], \tag{3.56}$$

where $\theta(T_E)$ denotes the potential temperature at the eastern and $\theta(T_W)$ that at the western boundary. For $u_{tr}^{max} < 0$, A_T^{tr} is obtained by replacing $\theta(T_W)$ with $\theta(T_E)$ and viceversa. A_v^{tr} is calculated by again substituting the specific humidities q_i to the corresponding $\theta(T_i)$.

3.3 The annual cycle of the Indian monsoon

This section discusses the annual course of the Indian monsoon as simulated by the reduced-form model. For this purpose, the model is forced by the annual cycle of solar radiation, according to Berger (1978). The boundary conditions, i.e., temperature and relative humidity at each of the four boundaries, Hadley circulation and zonal wind intensities, are prescribed according to their observed seasonal values (cf. Table 3.3). The dynamics of the system is determined by the governing equations (3.2), (3.4), (3.5) and (3.6). Note that Eqs. (3.2) and (3.4) can be rewritten as ordinary differential equations by solving the integrals for the vertical profiles of potential temperature, specific humidity and density specified by Eqs. (3.7), (3.9) and (3.10). The governing equations are integrated by applying a simple Euler forward scheme with a time-step of twelve hours. The latter is the largest step size for which the integration procedure converges.

The resulting dynamics is depicted in Figs. 3.2 and 3.3. The summer monsoon regime is clearly distinguishable from the winter regime as the hydrological cycle is much stronger.

	Variable	Dec.	March	June	Sept.	Unit
h_H	Hadley circulation turning height	1000	1000	1000	1000	m
v_H^0	Hadley circulation velocity for z $< h_H$	-2.5	-2.0	0.2	-1.5	$\mathrm{m\,s^{-1}}$
u_{tr}^{max}	Maximum trade wind velocity	39	31	-2.8	13	$\mathrm{m\,s^{-1}}$
u_{tr}^0	Trade wind velocity at z = 0	-3.2	-3	-2.5	-3	$\mathrm{m\,s^{-1}}$
h_{tr}	Trade wind turning height	1500	1500	0	1500	m
T_S	Temperature at southern boundary	299	300	301	300	K
T_N	Temperature at northern boundary	275	280	285	280	K
T_E	Temperature at eastern boundary	299	300	301	300	K
T_W	Temperature at western boundary	297	298	299	298	K
f_S	Relative humidity at southern boundary	0.75	0.8	0.85	0.8	1
f_N	Relative humidity at northern boundary	0.2	0.3	0.4	0.3	1
f_E	Relative humidity at eastern boundary	0.75	0.8	0.85	0.8	1
f_W	Relative humidity at western boundary	0.75	0.8	0.85	0.8	1

Table 3.3: Values of the boundary conditions at the 21$^{\mathrm{st}}$ of the indicated months. Intermediate values are obtained by linear interpolation. For the meridional velocity v_H positive values denote southerlies and for the zonal velocity u_{tr} they denote westerlies.

The transition from the winter to the summer monsoon regime occurs in early May, when the ascending motion associated with the monsoon circulation is strong enough to overcome the weakly subsiding limb of the large-scale Hadley circulation. This is reflected in the vertical velocity, which becomes positive (cf. Fig. 3.2-h). Moist air advected from the adjacent oceans is now forced to rise, leading to the formation of deep cumulus clouds which, in turn, give rise to enhanced precipitation (Fig. 3.2-c) and latent heat release to the atmosphere. This initiates a positive feedback loop whereby more heat release leads to a stronger upper-tropospheric pressure gradient, intensified monsoon circulation and stronger moisture convergence over India (Fig. 3.2-f). Cumulus cloudiness, on the other hand, increases the planetary albedo, counteracting the atmospheric warming by reflecting a larger fraction of solar radiation back to space (Figs. 3.3-b, -c and -d). Also, increased horizontal advection of heat towards the Indian Ocean and the Tibetan Plateau moderates the warming of the system (Fig. 3.3-g). The hydrological cycle is strongest in July when the Indian Ocean, which lags the insolation maximum by one to two months, is warmest. As the zenith angle of the sun begins to decline, the land-ocean temperature contrast decreases and the hydrological cycle weakens. As the ascending motion associated with the monsoon weakens and is surmounted by the subsiding limb of the Hadley circulation which begins to establish in October, the monsoon again settles in the winter regime.

This picture emphasizes the role of the large-scale circulation patterns, in particular the Hadley cell, in shaping the seasonal evolution of the Indian monsoon. Their effect, however, is not limited to the reinforcement/suppression of vertical motions. In fact, both Hadley and trade-wind circulation play an important role in the horizontal advection of heat and moisture. Similarly to the monsoon circulation, they transport heat towards India in winter and towards the ocean in summer, moderating the thermal contrast. In summer, they also supply moisture to the thermodynamical engine over India.

As discussed previously, the land cover plays an important role in modulating the dynamics of the Indian monsoon (cf., e.g., Claussen 1997). Indeed, the vegetation fraction (Fig. 3.3-h) determines the main surface properties (i.e., roughness and albedo) and therefore

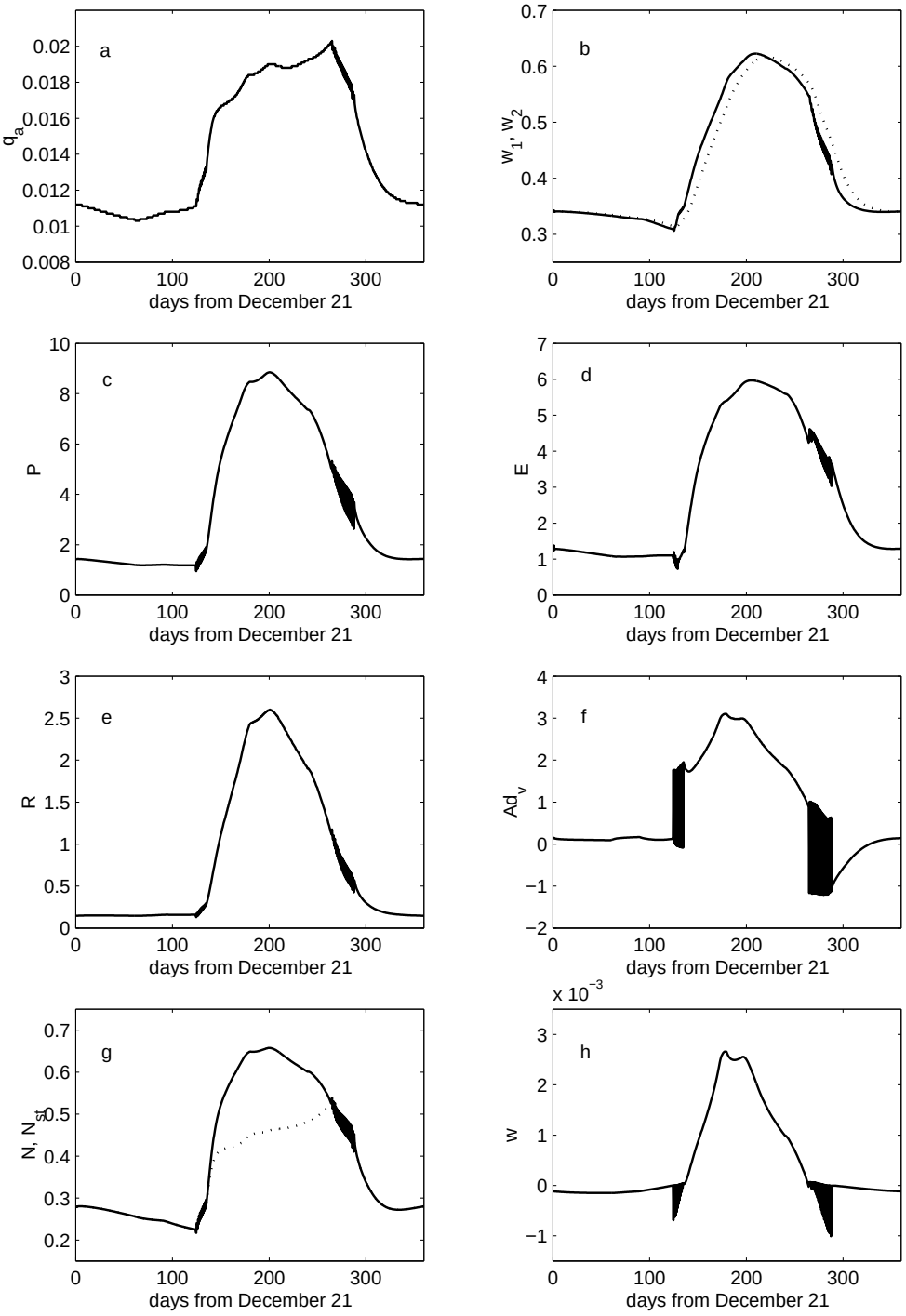

Figure 3.2: Annual evolution of key components of the hydrological cycle. a) Surface specific humidity [kg m^{-3} s^{-1}]. b) Soil moisture w_1 (solid) and w_2 (dotted) [1]. c) Precipitation [mm d^{-1}]. d) Evapotranspiration [mm d^{-1}]. e) Runoff [mm d^{-1}]. f) Advection of moisture [mm d^{-1}]. g) Total (solid) and stratus (dotted) cloud cover [1]. h) Vertical velocity [m s^{-1}]. Note that the oscillations (with a period of about one day) exhibited by some of the variables during the onset and withdrawal of the summer monsoon are caused by the sharp switches between regimes characterized by positive and negative values of vertical velocity (cf. section 3.2.9).

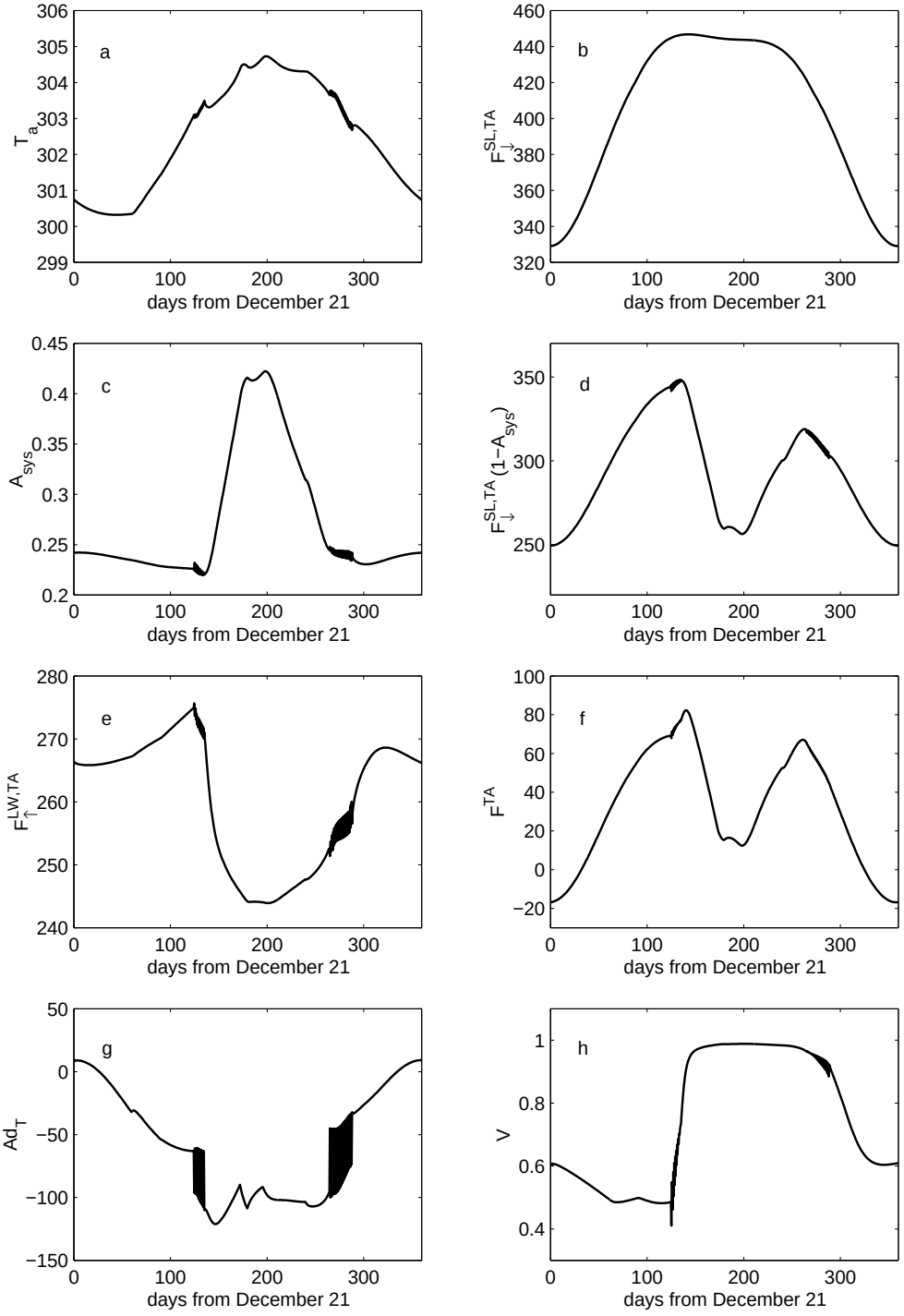

Figure 3.3: Annual evolution of key components of the heat budget. a) Surface air temperature [K]. b) Incident solar radiation at the top of the atmosphere (TA) [$\mathrm{W\,m^{-2}}$]. c) Planetary albedo [1]. d) Net solar radiation at TA [$\mathrm{W\,m^{-2}}$]. e) Outgoing long-wave radiation at TA [$\mathrm{W\,m^{-2}}$]. f) Net radiation at TA [$\mathrm{W\,m^{-2}}$]. g) Advection of heat [$\mathrm{W\,m^{-2}}$]. h) Vegetation fraction [1].

	Variable	Model	Data	Model	Data
		Summer		Winter	
T_a	Surface temperature	304.6^a	303^a	300.9^b	298^b
P	Precipitation	8.0^c	7.6^c	1.3^d	0.4^d
N	Cloud cover	0.65^a	0.8^a	0.28^b	0.3^b
E	Evapotranspiration	2.8^e	2.8^e	–	–
$F_{\downarrow}^{SL,TA}$	Incident solar radiation	442^c	450^c	351^d	325^d
A_{sys}	Planetary albedo	0.27^e	0.25^e	–	–
$F_{\downarrow}^{SL,TA}(1-A_{sys})$	Net solar radiation	293^e	300^e	–	–
$F_{\uparrow}^{LW,TP}$	Outgoing LW radiation	260^e	250^e	–	–
–	Regime transition	early May	May	mid October	October

Table 3.4: Comparison of the model results with observational data (Peixoto and Oort, 1992) for the summer and winter monsoon regimes. Precipitation data is taken from Parthasarathy (1994). [a]Values averaged over July. [b]Values averaged over December. [c]Values averaged over June-July-August. [d]Values averaged over December-January-February. [e]Annual mean values. Units are as in Figs. 3.2 and 3.3.

influences the monsoon circulation. The latter feeds back on the vegetation cover through precipitation. In our model, interactive vegetation reduces the seasonal temperature variations and intensifies the hydrological cycle, particularly during the summer monsoon.

Qualitatively, the annual cycle of the monsoon as simulated by our box model resembles well the observed monsoon dynamics. Table 3.4 and Fig. 3.4 demonstrate that the correspondence is satisfactory also in quantitative terms by displaying the model results along with observational data (Parthasarathy et al. 1994; Peixoto and Oort 1992). The annual or seasonal values of most of the model variables displayed in Table 3.4 deviate by less than ten percent from the observed values (cf. Table 3.4). The major difference concerns the temperature over India: the modeled temperature is 1.6 K warmer than the observed value in summer and about 3 K warmer in winter. As a consequence, the land is slightly warmer than the surrounding ocean even in winter, such that the land-ocean temperature gradient is not truly reversed[1]. This leads to moisture convergence over India also during the winter months, and higher winter precipitation than observed (cf. Fig. 3.4). The higher winter temperature could also be the cause for the earlier than observed monsoon onset, which occurs at the end of April/begin of May instead of mid May and the higher precipitation in the early monsoon phase. Peak summer precipitation and the withdrawal of the south-westerly monsoon are, on the other hand, captured correctly by our reduced-form model.

We define the monsoon onset as the time when precipitation begins to rise sharply, which corresponds to a switch in the vertical velocity from negative to positive values and the startup of convection (cf. Fig. 3.2-c and -h). The monsoon withdrawal is defined as the time cumulus convection ceases, which is again associated with a switch in the vertical velocity.

All in all, our simple model performs well in simulating the observed monsoon dynamics. This demonstrates that despite its high degree of idealization the model captures the essential physical processes and feedback mechanisms. Note that a closer fit to the observed annual evolution of precipitation, the most policy relevant variable, could be enforced by tuning some

[1]Note that this finding is not necessarily in contradiction to common knowledge. Usually it is referred to the large-scale temperature contrast between the Eurasian land-mass and the Indian Ocean which is much stronger (particularly in winter) than that between Indian Ocean and peninsula.

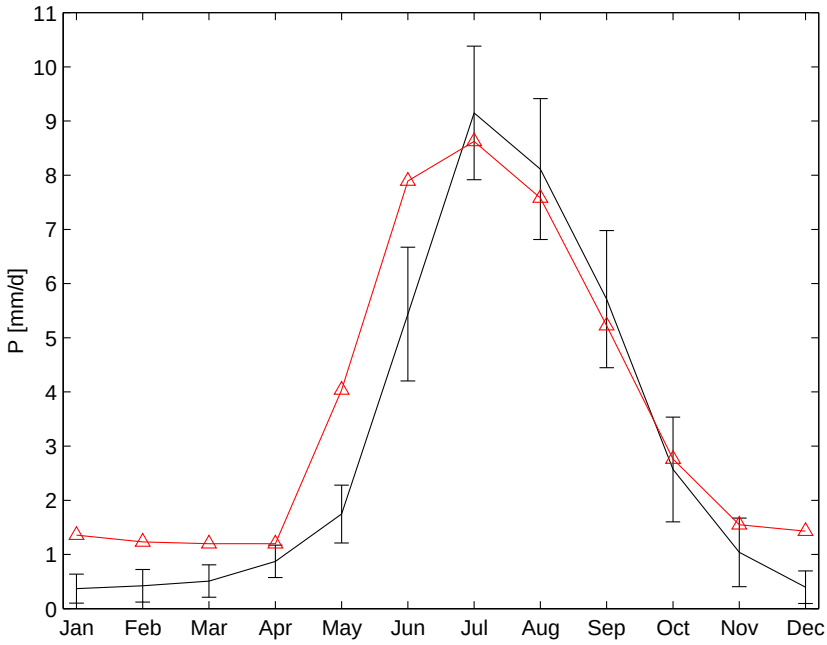

Figure 3.4: Modeled (red) and observed (black) monthly mean precipitation values. The observed data (Parthasarathy 1994) is averaged over the period 1871-1990. The bars encompass two standard deviations.

of the model parameters we have so far considered as fixed (cf. Tables 3.1 and 3.2).

3.4 Reduction of the basic model

This section describes the reduction of the basic monsoon model to a form which can be treated analytically. The idea is to use the latter to identify qualitative changes in the Indian monsoon dynamics induced by parameter variations. To this scope, we identify the steady state model solutions and analyze their linear stability, first for standard and subsequently for perturbed parameters and boundary conditions.

We proceed by reducing the model so as to get the most simple 'caricature' of the Indian monsoon (the 'elementary monsoon'; Webster 1987). This is achieved by omitting geographical detail, neglecting the large-scale circulation patterns and simplifying some parameterizations. In addition, we remove the seasonal cycle by 'freezing' the system at summer resp. winter conditions. In detail, we apply the following simplifications:

- Equal conditions at all four boundaries ($T_N = T_S = T_E = T_W := T_{oc}$, $q_N = q_S = q_E = q_W := q_{oc}$)
- Neglect of Hadley and trade-wind circulations ($v_H = u_{tr}$=0)
- Prescription of cloudiness N
- Prescription of fractional vegetation cover (V=1)
- Equality of effective evapotranspiration with potential evapotranspiration ($E_v = E_v^{max}$)

- Prescription of turnover time of water in the atmosphere ($\tau_P = \tau_0$)
- Prescription of surface temperature T_s.

In a subsequent step, we express all terms on the right hand sides of the governing equations (3.2), (3.4), (3.5), (3.6) as functions of the variables T_a, q_s, w_1, w_2 and constant coefficients C_i^j:

$$E := -C_E^1\, w_1\, q_a\, T_a + C_E^2\, w_1\, T_a + C_E^3\, q_a\, w_1 - C_E^4\, w_1, \tag{3.57}$$

$$C = P := C_P\, q_a, \tag{3.58}$$

$$R := C_R\, q_a\, w_1, \tag{3.59}$$

$$A_v := C_{A_v}^1\,(T_a - T_{oc}) - C_{Av}^2\, q_a\,(T_a - T_{oc})\,, \tag{3.60}$$

$$F_{\downarrow}^{SL,TA}\,(1 - A_{sys}) := C_{SL}, \tag{3.61}$$

$$F_{\uparrow}^{LW,TA} := C_{LW}^1 + C_{LW}^2\, T_a, \tag{3.62}$$

$$A_T := C_{A_T}^1\,(T_a - T_{oc}) + C_{A_T}^2\, T_a\,(T_a - T_{oc}) - C_{A_T}^3\,(T_a - T_{oc})\,(\Gamma - \Gamma_a)\,. \tag{3.63}$$

The coefficients C_i^j are defined in appendix B (Table B.1).

We then collect the terms with the same combination of variables and obtain the following system of ordinary differential equations:

$$\dot{w_1} = A_2\, w_2 + B_2\, w_1 + C_2\, q_a - D_2\, w_1\, q_a - E_2\, T_a\, w_1 + F_2\, T_a\, w_1\, q_a, \tag{3.64}$$

$$\dot{w_2} = A_1\, w_1 - A_1\, w_2 - B_1, \tag{3.65}$$

$$\dot{q_a} = -A_3\, w_1 + B_3\, q_a + C_3\, T_a + D_3\, w_1\, q_a + E_3\, w_1\, T_a - F_3\, T_a\, q_a - G_3\, T_a\, w_1\, q_a - H_3, \tag{3.66}$$

$$\dot{T_a} = A_4\, q_a + B_4\, w_1 + C_4\, T_a - D_4\, T_a\, q_a^2 + E_4\, q_a^2 + F_4\, T_a\, w_1\, q_a - G_4\, T_a\, w_1 - H_4\, w_1\, q_a + I_4\, T_a^2 + J_4\, T_a^2\, q_a^2 + K_4. \tag{3.67}$$

These ordinary differential equations include polynomial nonlinearities up to 4^{th} order. Their coefficients are given in appendix B (Table B.2).

3.4.1 Steady state solutions of the reduced model

In the following, we discuss the steady state solutions of the reduced monsoon model described above. They are derived by equating the right hand sides of Eqs. (3.64)–(3.67) with zero and successively eliminating the variables w_2, q_a and w_1 until a closed analytical expression for T_a is obtained (cf. appendix B). The latter is an 8^{th} order polynomial in T_a which takes two different forms (referred to as $f_+(T_a)$ and $f_-(T_a)$, respectively), one for each solution of w_1 (Eqs. (B.4–B.5)). The steady state solutions of T_a are derived as the zeros of the polynomials $f_+(T_a)$ and $f_-(T_a)$, those of the other variables are obtained by substituting the values of T_a into the respective expression (Eqs. (B.1)–(B.3)).

Given the algebraic complexity of $f_+(T_a)$ and $f_-(T_a)$, we don't attempt to solve these polynomials analytically, but employ appropriate routines provided by the MATLAB package (i.e., the function `fzero`). For summer, we identified two real solutions for both $f_+(T_a)$ and $f_-(T_a)$, for winter four. Table 3.5 displays the steady state values of the variables T_a, q_a, w_1

Solution	T_a^0	w_1^0, w_2^0	q_a^0	Linear Stability
		Summer		
1	**302.8**	**0.76**	**0.021**	**stable**
2	303.0	-0.66	-0.036	unstable
		Winter		
1	281.2	-4.4	0.020	unstable
2	**293.8**	**0.03**	**0.004**	**stable**
3	297.3	-0.51	-0.282	unstable
4	297.7	-0.43	-0.047	unstable

Table 3.5: The simplified monsoon model's steady state solutions and their linear stability for both summer and winter conditions. Summer conditions are realized under the following settings: summer insolation at it's peak, $w > 0$, $T_a > T_{oc}$, $N = 0.66$, $T_{oc} = 300$, $f_{oc} = 0.85$. Winter conditions are realized under the settings: insolation at the winter solstice, $w < 0$, $T_a < T_{oc}$, $N = 0.28$, $T_{oc} = 299$, $f_{oc} = 0.75$.

and w_2 for summer and winter conditions (the parameter settings associated with the latter are specified in the table's caption).

In a next step, we investigate the linear stability of the steady state solutions. We proceed by calculating the Jacobian of the system of differential Eqs. (3.65)–(3.67) and performing a classical eigenvalue analysis (Argyris et al. 1995). The eigenvalues are calculated using the function `eig` provided by the MATLAB package.

Our analysis indicates that in summer as well as in winter a single steady state is stable (cf. Table 3.5). These stable equilibria correspond to the summer and winter monsoon regimes discussed in section 3.3: they are associated with high temperature, humidity and soil moisture for summer and low values of these variables for winter conditions. The summer to winter differences of these variables, however, are much more pronounced than in the basic model. The reason is the neglect of the Hadley and trade-wind circulations and the associated advection of heat and moisture. The unstable steady state solutions are mostly unphysical being associated with negative values of humidity and/or soil moisture.

3.4.2 Sensitivity and bifurcation analysis of the reduced model

In this section, we describe the sensitivity of the steady state solutions and their qualitative structure to variations of the model parameters and boundary conditions. We devote particular attention to the quantities influenced by human actions (i.e., emissions of greenhouse gases and aerosols, land-cover changes), and/or subject to natural variability. These include the conditions at the oceanic boundaries, CO_2 concentrations, planetary albedo ${A_{sys}}^2$, characteristic precipitation time τ_P (the latter being potentially related to natural and anthropogenic emissions of aerosols), surface roughness z_v and insolation $I_0 \cos \xi$. We limit our discussion to the summer monsoon, since it is qualitative changes in this regime which would strongly affect India's agriculture and socio-economy (cf. section 1.5).

Fig. 3.5 illustrates the sensitivity of the steady state solutions T_a^0 to variations of some

[2]Note that in our model A_{sys} is not a parameter but a function of the cloudiness N and vegetation fraction V (cf. section 3.2.7). Given, however, that in the reduced model these quantities are prescribed, A_{sys} can be treated as a parameter. Note also that in the sensitivity experiments A_{sys} is varied independently of N.

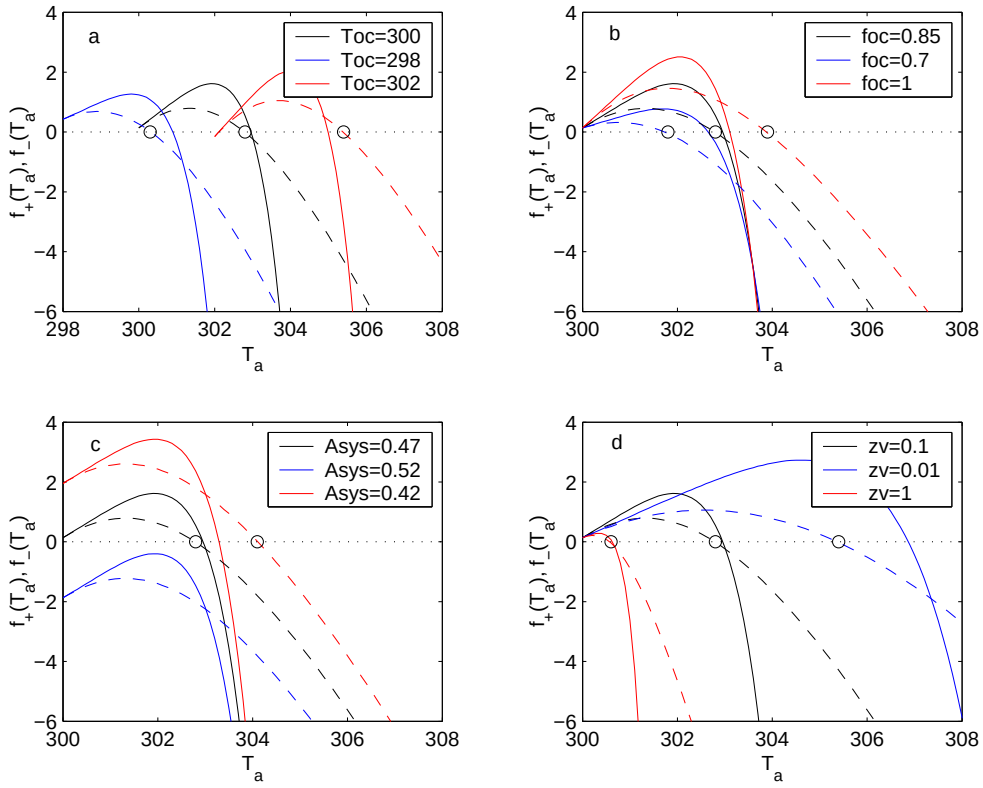

Figure 3.5: Polynomials $f_+(T_a)$ (solid), $f_-(T_a)$ (dashed) for summer conditions and different values of the following parameters: a) temperature over the ocean T_{oc} [K], b) relative humidity over the ocean f_{oc} [1], c) planetary albedo A_{sys} [1], d) surface roughness z_v [m]. Note the disappearance of the stable solution (open circle) for A_{sys} equal to 0.52. Recall that $f_+(T_a)$ and $f_-(T_a)$ are derived from the four-dimensional system through successive elimination of the variables w_1, w_2, q_a. Their functional form determines the qualitative structure and position of the steady state solutions (and is therefore related to the bifurcation diagram), but does not bear any deeper physical meaning.

of the aforementioned parameters by displaying the polynomials $f_+(T_a)$, $f_-(T_a)$ for different parameter constellations. In the following, we will focus our discussion on the stable state (marked by the circle), given that the other solutions are physically irrelevant.

Our results indicate that a 2 K increase (decrease) in the temperature at the oceanic boundary T_{oc} leads to a shift of the polynomials to the right (left) (cf. Fig. 3.5-a). As a consequence, the stable equilibrium is displaced towards higher (lower) values of T_a, which also results in increased (decreased) values of w_1, w_2 and q_a (not shown).

When f_{oc} is varied, $f_-(T_a)$ is displaced to the left (right) for decreased (increased) values of f_{oc} (Fig. 3.5-b). Accordingly, the stable solution is located at lower (higher) values of T_a.

For variations of A_{sys}, the curves are displaced vertically: for a decrease (increase) in albedo by 0.05 $f_+(T_a)$ and $f_-(T_a)$ are displaced upwards (downwards). Notably, for A_{sys} equal to 0.52, the polynomial $f_-(T_a)$ shifts entirely below the zero line (cf. Fig. 3.5-c). This results in the 'disappearance' of the stable solution: as will be discussed below, the latter becomes unstable as it undergoes a so-called 'saddle-node bifurcation'. We find that the stable equilibrium disappears also in the case of lowered insolation $I_0 \cos\xi$ (not shown), the relevant quantity being the amount of solar radiation penetrating to the surface. The insolation value

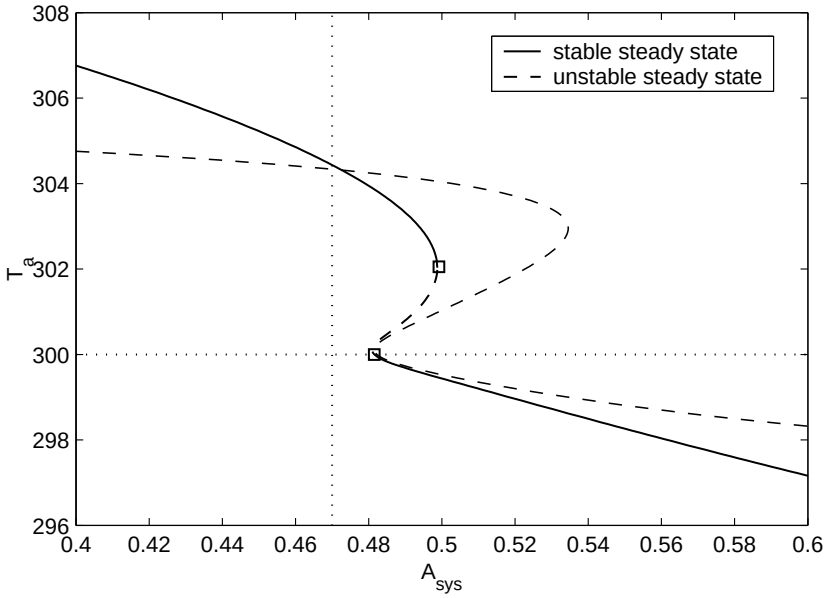

Figure 3.6: Bifurcation diagram of the summer monsoon regime. The squares mark the saddle-node bifurcations. The vertical and horizontal dotted lines indicate the present-day value of A_{sys} resp. the value of T_a at which the land-ocean temperature gradient is reversed.

at which the summer monsoon regime is destabilized is 425 $\mathrm{W\,m^{-2}}$, which corresponds to a decrease by about 5% of the present-day value.

Similarly, for changes in CO_2 concentrations the curves are displaced vertically, though less markedly: doubling (halving) present-day pCO_2 results in slight upward (downward) shifts. In order to destabilize the stable equilibrium pCO_2 is to be lowered to a value of about 110 ppm (not shown).

In the case of an increase (decrease) of the surface roughness z_v by one order of magnitude (which can be taken to mimic land-cover changes towards rain-forest resp. desert), the changes are rather pronounced: the stable equilibrium shifts towards considerably lower (higher) values of T_a (cf. Fig. 3.5-d). Note that in this case a lower value of T_a results in higher values of w_1, w_2 and q_a (not shown).

In contrast, variations of the characteristic precipitation time τ_P do not have marked effects: increases (decreases) of τ_P by up to 25% lead to slight contractions (enlargements) of the solution curves (not shown).

The most notable result of the above analysis is thus the destabilization of the stable steady state which occurs for a critical value of the planetary albedo (or insolation). Analysis of the eigenvalues associated with the stable steady state indicates that one of them crosses the imaginary axis at a value of A_{sys} of 0.5. This behavior of the eigenvalues is typical for a so called 'saddle-node bifurcation' (Sotomayor 1973). If such a bifurcation occurs on a branch of a stable state, the latter becomes unstable at the bifurcation point. Note that this is the same type of bifurcation that was identified for the THC at critical values of the North Atlantic freshwater forcing (cf. section 2.2.1).

By means of the the numerical bifurcation software AUTO (Doedel 1981), we followed the steady state solutions of the system against the planetary albedo. The resulting bifurcation diagram is displayed in Fig. 3.6. It confirms the qualitative features already evident in

Fig. 3.5-c: the stable solution branch becomes unstable for values of A_{sys} of 0.5.

An interesting question concerns the evolution of the system following destabilization of the stable steady state. Transient simulations with the reduced model reveal the existence of a further stable equilibrium: once the critical value of A_{sys} is transgressed, the system rapidly cools. This cooling causes the reversal of the land-ocean temperature contrast, such that the monsoonal cells as well as the vertical velocity change direction. This leads to the appearance of a new stable equilibrium in which the system settles (cf. Fig. 3.6). This steady state is associated with relatively low values of specific humidity ($q_a^0 = 0.004\ \mathrm{kg\,m^{-3}\,s^{-1}}$) and soil moisture ($w_1^0 = w_2^0 = 0.04$) and may therefore be referred to as 'dry' summer monsoon regime. The 'bistability' of the system is evident in Fig. 3.6: for A_{sys} ranging from 0.475 to 0.5, two stable equilibria coexist.

Physically, the existence of multiple equilibria is due to the moisture advection feedback described previously: the upper-level temperature gradient which drives the monsoon circulation is to a large extent maintained by the monsoon itself. Once the temperature gradient falls short of a critical value, the monsoon circulation cannot be sustained. Note the similarity to the role played by the salt advection feedback in giving rise to the bistability of the THC (cf. section 1.4).

Given that the saddle-node bifurcation is located not far from the present-day state, the question arises whether anthropogenic perturbations of the planetary albedo such as sulfur emissions or land-cover changes could drive the system across the critical threshold. In the following, we assess this possibility by (crudely) estimating the influence of changes in the above factors on the planetary albedo. The direct radiative effect of sulfate aerosols[3] is taken into account by increasing the opacity b_{cs} of the clear-sky atmosphere by 50%, while the first indirect effect (i.e., that on cloud optical properties) is accounted for by increasing the optical depth of stratus clouds by 50%. Other indirect effects are neglected. The above increments were chosen so as to reproduce the effects of a strong, but not unrealistic aerosol loading. The optical depth of cumulus clouds is left unchanged, as convection is less sensitive on the presence of cloud condensation nuclei (as which the aerosols act) than large-scale condensation. Implementation of the above changes yields an increase in the planetary albedo by about 9% (from 0.47 to 0.51).

Land-cover changes towards semi-desert, which are implemented in the model through changes in the values of surface roughness and albedo, lead to an increase in the planetary albedo by a similar amount (to 0.50). Thus, according to the simplified model, aerosol emissions alone or in combination with processes affecting the land surface such as desertification could well bring the system across the critical threshold. In section 3.5, we will discuss whether the same conclusion can be drawn with the basic model. Before doing so, a further reduction of the monsoon model is described.

3.4.3 Reduction to a three-dimensional system

Since the time scales of the hydrological variables q_a, w_1 and w_2 are much shorter than that of the surface temperature T_a, it is possible to separate their dynamics and reduce the four-dimensional to a three-dimensional (3d) system in the variables q_a, w_1 and w_2 with prescribed

[3]Sulfate aerosols originate from the oxidation of sulfur dioxide. Their radiative forcing is negative in sign. It consists of a 'direct' and an 'indirect' component. The direct effect is associated with the back-scattering of solar radiation; the first indirect effect is induced via changes in the optical properties of clouds. There are also other indirect effects, such as the influence of sulfate aerosols on cloud lifetime.

temperature T_a. The resulting nonlinear equations include polynomial nonlinearities up to 2^{nd} order as can easily be inferred from Eqs. (3.64)–(3.66). The 3d system exhibits one single stable steady state. Bifurcation analysis indicates that this state maintains its stability under variations of a number of parameters within broad ranges. This demonstrates that the fourth dimension (physically: the feedback processes involving surface temperature) is essential for the bifurcations discussed in the previous section to exist.

Notably, if a few further simplifications are applied (e.g., runoff is set equal to precipitation), it is possible to bring the 3d system into a form which resembles the classical Lorenz (1963) system. The structure of the nonlinear equations is identical, only the coefficients differ, being different from one in all equation terms (recall that in the Lorenz system only three coefficients, namely σ, r and b are different from one). The similarity between the 3d monsoon and the Lorenz model is remarkable in so far as it has been previously postulated (Palmer 1994) in order to interpret the seemingly chaotic transition between break and active monsoon phases (cf. section 1.5). In our model, under summer conditions and standard parameter settings all three steady states are found to be unstable. Cloud cover, e.g., has to be increased up to 0.9 for one stable state to exist. This state is associated with zero values of all variables, which is physically implausible. The bistable or chaotic domains cannot be reached with any realistic parameter constellation. This indicates that the simplifications we applied to the system are unphysical. Apart from representing an academic curiosity, the similarity of our 3d monsoon system to the Lorenz system does therefore not allow for real-world implications to be drawn.

3.5 Response of the monsoon to enhanced sulfate aerosol and CO_2 concentrations

After having explored the structure of the phase space of the reduced model and having identified possible bifurcation points, we come back to the basic model for a quantitative analysis of the sensitivity of the Indian monsoon to variations of model parameters and boundary conditions. We focus on changes of quantities which can be related to anthropogenic emissions of greenhouse gases (GHGs) and sulfur dioxide. The scope of these experiments is twofold: firstly, in view of integrated assessment applications, we intend to explore the ability of the model to realistically simulate the response of the Indian monsoon to climate change. Secondly, we are interested whether the bifurcation identified in the reduced system also occurs in the basic model under plausible parameter assumptions.

In a first set of experiments we force the system with conditions associated with increased GHG concentrations. Given that the conditions at the box boundaries have to be prescribed externally, the choice of the specific climate change scenario is limited to the already existing simulations with coupled climate models of global scale. As for the THC box model, we use the CLIMBER-2 model as reference and take the anomalies in the boundary conditions from an equilibrium $2\times CO_2$ experiment with this model (Ganopolski et al. 2001). We further consider scenarios with CO_2 concentrations increased to four times the pre-industrial value by linear extrapolation of the boundary conditions for the $2\times CO_2$ case (cf. Table 3.6). This is only a crude approximation since the response of the climate system to large concentration changes is certainly not linear, but given the overall simplicity of the model and the exploratory purpose of these experiments, we think it is a valid assumption.

We calculated the equilibrium response of the annual cycle of the Indian monsoon to the

	$2\times CO_2$		$4\times CO_2$		SO_4	
	Summer	Winter	Summer	Winter	Summer	Winter
$\Delta T_{S,E,W}$ [K]	2.5	2.5	5	5	-	-
ΔT_N [K]	3	4	6	8	-	-
Δu_{tr}^{max} [$m\,s^{-1}$]	-0.25	-0.25	-0.5	-0.5	-	-
Δv_H^0 [$m\,s^{-1}$]	-0.02	0.02	-0.04	0.04	-	-
pCO_2 [ppm]	560		1120		360	
B_{SO_4} [$mg\,m^{-2}$]	-		-		25	
τ_{st} [1]	-		-		9	
τ_0 [s]	-		-		$6{\cdot}10^5$	

Table 3.6: Anomalies in the boundary conditions and parameters imposed in the climate change experiments.

	CTL	$\Delta(2\times CO_2)$	$\Delta(4\times CO_2)$	$\Delta(SO_4)$	$\Delta(2\times CO_2{+}SO_4)$
Surface temperature	304.4	2.4	4.8	-0.55	1.9
Surface specific humidity	0.019	0.002	0.0045	0	0.001
Soil moisture	0.59	0	0	-0.03	-0.02
Precipitation	8.0	1.2	2.5	-1.6	-0.65
Evapotranspiration	5.6	0.8	1.8	-1.2	-0.5
Runoff	2.2	0.3	0.7	-0.5	-0.25
Advection of moisture	2.5	0.3	0.7	-0.4	-0.2
Cloud cover	0.63	0	0.01	-0.00	0
Cumulus cloud cover	0.31	0.01	0.03	-0.06	-0.06
Net solar radiation	277	-7	-15	-4	-7
Outgoing LW radiation	246	-1	-5	-1	-2
Advection of heat	-101	-3.5	-9	16	11

Table 3.7: June-July-August values of key components of the water and heat budgets for present-day ('CTL') and changed climate conditions. $\Delta(2\times CO_2)$, $\Delta(4\times CO_2)$, $\Delta(SO_4)$ and $\Delta(2\times CO_2{+}SO_4)$ denote differences between the respective climate change and the control experiment. Units are as in Figs. 3.2 and 3.3.

two CO_2 forcings indicated in Table 3.6. Table 3.7 displays the June-July-August (JJA) values of the main model variables for present-day climate conditions ('CTL') and their anomalies under the applied climatic changes.

Our results indicate a strengthening of the hydrological cycle under increased CO_2 conditions. In the $2\times CO_2$ and $4\times CO_2$ experiments JJA precipitation over India increases by 15% resp. 31% (cf. also Fig. 3.7). This strengthening of the hydrological cycle is due to higher specific humidity over the oceans which leads to stronger landward advection of moisture and hence increased convection, cumulus cloudiness and precipitation (cf. Table 3.7). At the surface, the increase in precipitation is balanced by higher evaporation and runoff such that soil moisture does not change markedly. At the top of the atmosphere, the change in long-wave radiation emitted to space is negligible, whereas the net incoming solar radiation decreases because of a larger planetary albedo associated with increased cumulus cloudiness. Export of heat towards the surrounding oceans by advection increases in the CO_2 runs (i.e., becomes more negative; cf. Table 3.7).

In both the $2\times CO_2$ and $4\times CO_2$ experiment, the summer monsoon sets on a few days earlier and withdraws about two weeks earlier (in late September instead of mid October; cf.

Fig. 3.7 and Table 3.8).

Perhaps surprisingly, the temperature contrast between the Indian Ocean and the Indian peninsula is reduced slightly under increased CO_2 conditions (since T_a increases less than T_S, T_E and T_W). As a consequence, the monsoon circulation weakens relative to the present-day strength. There are two explanations for this behavior. The reduction in the temperature contrast could be due to different sensitivities to CO_2 concentrations of the radiative scheme implemented in the CLIMBER-2 model, which is used to determine the temperatures at the boundaries, and the Budyko (1982) scheme used in the present model. Alternatively, the weakening of the temperature gradient may be associated with increased cumulus cloud cover which reduces the amount of solar radiation penetrating to the surface. This explanation is consistent with GHG experiments with comprehensive models which indicate a local minimum of temperature increase over India due to significant changes in the hydrological cycle (Kitoh et al. 1997).

A number of studies have identified a stronger land-ocean temperature contrast as a primary reason for the intensification of monsoon precipitation in response to increased CO_2 concentrations (Meehl and Washington 1993; Bhaskaran and Mitchell 1998; Hu et al. 2000). Our results are not necessarily in contradiction to these studies since, as noted previously, they refer to the large-scale difference between the Eurasian continent and the Indian Ocean, which can be expected to be much stronger than that between the Indian peninsula and the adjacent Indian Ocean.

Besides possible differences in simulating the land-ocean temperature contrast, the results with our simple monsoon model are very similar to those obtained with atmospheric GCMs. In fact, most of the recent studies simulate an increase in summer precipitation over India along with a weakening of the monsoon circulation (Kitoh et al. 1997; Douville et al. 2000; May 2002). The precipitation increase is attributed to an intensification of the atmospheric moisture transport into the Indian region. This intensification is achieved despite the weakening of the monsoon circulation because of the larger water content in the warmer atmosphere.

In a subsequent set of experiments, we investigate the response of the Indian monsoon to increased anthropogenic sulfur emissions. Given that our model does not include a proper representation of the sulfur chemistry, the aerosol forcing is treated in a highly idealized way. The direct radiative effect due to back-scattering of solar radiation in the clear-sky atmosphere is expressed as a perturbation of the surface albedo depending on the total sulfate aerosol burden in the atmospheric column (Mitchell et al. 1995; Meehl et al. 1996; Haywood 1997):

$$\Delta A_s = (1 - A_s)^2 \; k_e \, B_{SO_4} \, \beta \, \cos(\xi)^{-1},$$

where k_e is the specific extinction coefficient of sulfate aerosol, B_{SO_4} is the total column burden of sulfate and β is the backscattered fraction. k_e and β are set to values of 8 $\mathrm{m^2\,g^{-1}}$ and 0.29 (Mitchell et al. 1995). The sulfate aerosol concentration is taken from a study in which a chemical transport model coupled to an AOGCM is driven by IPCC emission scenario IS92a (Roeckner et al. 1999). The employed value of 25 $\mathrm{mg\,m^{-2}}$ corresponds to the decadal mean for 2040–2050 over India. For a surface albedo of 0.16 (which corresponds to the summer value in our model), the above formula leads to an increase in surface albedo by almost 50%.

The first indirect aerosol effect is taken into account by increasing the optical depth of stratus clouds by 20%. This increment is the result of educated guesswork rather than a value derived from model simulations. The procedure, however, to consider the indirect

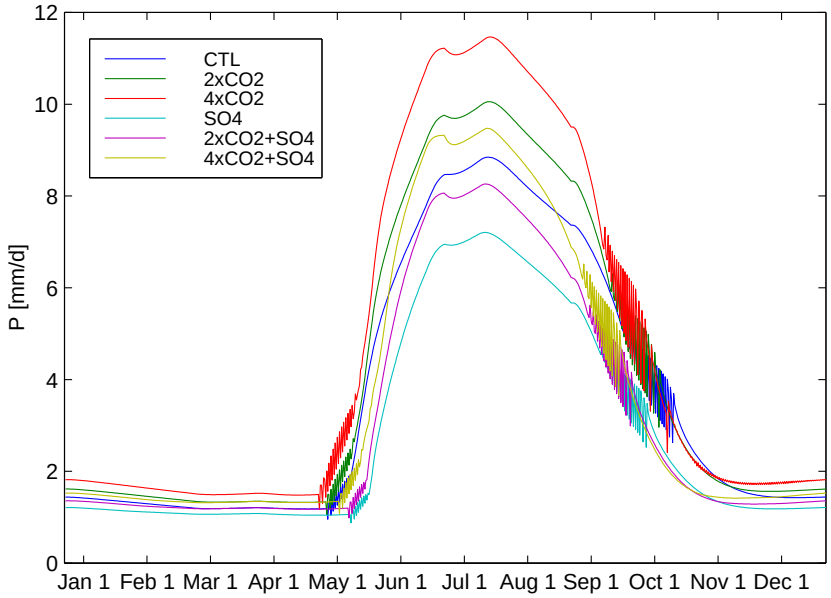

Figure 3.7: Annual cycle of Indian rainfall under present-day and increased CO_2 and sulfate aerosol concentrations.

Experiment	Monsoon Onset	Monsoon Withdrawal
CTL	early May	mid October
$2\times CO_2$	early May	late September
$4\times CO_2$	late April	late September
SO_4	mid May	late September
$2\times CO_2+SO_4$	mid May	mid September
$4\times CO_2+SO_4$	early May	mid September

Table 3.8: Duration of the Indian summer monsoon under present-day and enhanced CO_2 and sulfate aerosol concentrations.

aerosol effect via increase in cloud albedo is applied in studies with complex models as well (cf., e.g., Meehl et al. 1996). Through their effects on the size of cloud droplets, aerosols also affect precipitation directly. In fact, large concentrations of aerosols nucleate smaller droplets that coalesce inefficiently into raindrops (Rosenfeld 2000). We account for this effect by increasing the characteristic precipitation time τ_0 by 20%.

The parameter settings used in the aerosol experiment (denoted 'SO_4') are summarized in Table 3.6. Note that we leave the conditions at the boundaries unchanged given that the aerosol loading is found to be mainly concentrated over the Asian continent (Roeckner et al. 1999).

The results of the SO_4 experiment are displayed in Table 3.7. Our results indicate that the increased reflectivity of the atmosphere under both clear-sky and cloudy conditions leads to a reduced fraction of solar energy entering the systems. This leads to a weakening of the land-ocean temperature contrast and, in turn, the monsoon circulation. As a consequence, landward advection of moisture, evaporation and precipitation are reduced. This general weakening of the hydrological cycle is amplified by the direct effect of the aerosols on pre-

cipitation. In fact, higher τ_0 decreases the precipitation efficiency (defined here as $1/\tau_P$; cf. Eq. 3.25), and, in turn, the latent heat release to the atmosphere. This further weakens the land-sea temperature contrast. The overall effect of the scattering aerosols is a reduction of summer precipitation by as much as 20% (cf. Table 3.7 and Fig. 3.7). The duration of the summer monsoon is reduced by more than one month.

In a further experiment, we apply the aerosol forcing in addition to the $2\times CO_2$ forcing (experiment labelled '$2\times CO_2$+SO_4'). Our results indicate that the aerosol effect dominates the CO_2 effect, the precipitation over India being reduced by 8% as compared to the present-day value. The physical mechanism responsible for this decrease in precipitation is again the cooling of the land relative to the ocean. Note that the results for the $2\times CO_2$+SO_4 experiment are similar, but not identical to the sum of the values of the SO_4 and $2\times CO_2$ experiments, indicating the operation of some feedback mechanism. If the aerosol forcing is superimposed on the $4\times CO_2$ forcing, the summer precipitation is higher than under present-day conditions, but the monsoon withdraws about one month earlier (cf. Fig. 3.7 and Table 3.8).

The results obtained with our model are in line with the findings of complex climate models which show a weakening of the Indian summer monsoon in response to sulfate aerosol forcing (Meehl et al. 1996; Boucher et al. 1998). If aerosol forcing is superimposed on GHG forcing, the results of the comprehensive models diverge, with some of them showing that GHG warming more than offsets the aerosol effect (Roeckner et al. 1999). Others show that the aerosol effect dominates, such that the Indian monsoon is less vigorous than today's (Lal et al. 1995; Bhaskaran and Mitchell 1998). These results demonstrate the large uncertainty associated with the radiative effects of aerosols, in particular the indirect ones.

An issue worth exploration is whether the system, driven by changes in sulfate concentrations and/or other processes affecting planetary albedo such as land-cover changes, could hit the bifurcation point identified in section 3.4.2. This question gains particular relevance in the light of observational evidence showing that a large cloud of anthropogenic haze spreads over South and Southeast Asia (Lelieveld et al. 2001). On the basis of calculations with the reduced model, we concluded that the system could be brought in the proximity of the threshold for plausible changes in opacity, stratus cloud and surface albedo. The question whether this possibility is maintained also in the more 'complex' model is legitimate in so far as in the reduced model some feedback mechanisms are suppressed because of the prescription of cloudiness. We proceed by varying some of the parameters affecting planetary albedo and simulating the annual cycle of the Indian monsoon for the modified parameter settings. We found that a combination of increased opacity, increased surface and cloud albedo (both stratus and cumulus) and reduced precipitation efficiency is capable of suppressing the 'wet' summer monsoon regime. The parameter changes required in our model, however, lie probably outside the plausible range. The reason is that emissions of sulfur dioxide will not continue to rise indefinitely (Nakićenović and Swart 2000). Also, our calculations still include a number of simplifying assumptions. For lack of availability of seasonally resolved data, we took the aerosol forcing to be constant over the year although a pronounced seasonal variability is observed: associated with the seasonal cycle of the atmospheric winds and stability conditions, the anthropogenic aerosol loading over Asia builds up from October, peaks in March and decreases during the summer under the washout and scavenging influence of the summer monsoon (Ramanathan et al. 2001). Further, the Indo-Asian haze is composed not only of scattering but also of absorbing aerosols such as black carbon, which are observed to considerably heat the lower troposphere (Ramanathan et al. 2001). Last but not least, the effects of the scattering aerosols on the Indian monsoon is counteracted by GHG warming.

A synthesis of the findings discussed in this chapter and the resulting conclusions will be presented in chapter 5.

Chapter 4

Emissions corridors preserving the Atlantic thermohaline circulation

4.1 Motivation

The aim of this chapter is the presentation of an exemplary integrated assessment (IA) application of the reduced-form model of the Atlantic thermohaline circulation (THC) discussed in chapter 2. To this end, we draw on the conceptual and methodological framework provided by the tolerable windows approach (TWA; Petschel-Held et al. 1999; Bruckner et al. 1999). Recall that the latter is an inverse approach which attempts to derive ranges of CO_2 emissions ('emissions corridors') which are compatible with predefined policy goals ('guardrails'). Here, we derive emissions corridors which are compatible with two kinds of guardrails. The first is environmentally motivated and aims at preventing 'dangerous' changes in the THC. The second is socio-economic in nature and is meant to limit the costs of GHG emissions reduction ('mitigation'). These guardrails are in accordance with the goals of environmental and socio-economic sustainability put forward by Article 2 of the UNFCCC (section 1.6).

With one exception (Tóth et al. 1998), earlier studies (Keller et al. 2000; Mastrandrea and Schneider 2001) exploring the implications of nonlinear changes in the THC for climate change decision-making were conducted in a cost-benefit framework (cf. section 1.6). We draw on the TWA as it offers several advantages compared to conventional integrated assessment approaches such as cost-benefit analysis, particularly in the context of singular climate change (Schellnhuber 1997; Bruckner et al. 1999). Firstly, it is designed from the very beginning to account for nonlinear and threshold effects in the climate system. Secondly, it avoids the difficult aggregation across time, space and impact categories which is needed to valuate the benefits of avoided damages and compare them to the costs of climate protection. Thirdly, it allows for a clear separation of normative settings[1] and rigorous scientific analysis. Lastly, any analysis carried out on the basis of the TWA does not need the specification of a damage function. This is particularly relevant in the present context since, as discussed in section 1.4, we are far from being able to come up with a complete accounting of the impacts associated with THC changes.

The first attempt to consider nonlinear changes in the THC within the framework of the TWA was made by Tóth et al. (1998). In their study, a translated version (to temperature

[1] A setting is normative when it involves value judgments. The definition of unacceptable impacts or unbearable mitigation costs is, for instance, a normative setting.

change-rate of temperature change phase space; cf. section 2.5.4) of the THC stability diagram derived by Stocker and Schmittner (1997) is applied as guardrail preventing a shutdown of the THC. This procedure, however, implies some drastic simplifications: it assumes that restrictions are imposed on the actual magnitude and rate of temperature change rather than on the asymptotic temperature change and the long-term average rate of change, although the latter were used to derive the stability curve. This illustrates the need to incorporate a dynamic THC model into the modeling framework of the TWA.

For the analysis presented in this chapter, we couple the (dynamic) reduced-form THC model described in chapter 2 to a globally aggregated multi-gas climate model (section 4.3). This allows us to represent the full causal chain from emissions of GHGs and aerosols to THC intensity, which is needed to translate the THC guardrail into the admissible range of emissions (i.e., the emissions corridor). The socio-economy is not modeled explicitly: the pertinent guardrails are considered in a simplified way in the form of constraints on the emissions behavior (section 4.4). The variety of results (section 4.5) demonstrates the strength of this modeling framework.

4.2 Mathematical background and algorithm for the calculation of emissions corridors

As may intuitively be clear, emissions corridors represent set-valued solutions to an inverse problem. Let's, for example, set a guardrail limiting the magnitude of global mean temperature change. Then a full bundle of emissions trajectories exists which allows one to fall short of the specified temperature level. The derivation of emissions corridors is therefore far from trivial and can only be tackled by the application of sophisticated concepts and methods provided by mathematical theory.

In mathematical terms, the calculation of emissions corridors may be formulated as a control theoretic problem. From the perspective of this theory, the time evolution of the system considered is described by a vector-valued function of state variables. This function, which is denoted by $\mathbf{x}(t)$, includes time-dependent paths of variables such as concentrations of all major greenhouse gases, global mean temperature and the strength of the THC. The time evolution of the system is determined by an appropriately chosen control function $\mathbf{u}(t) \in \mathcal{U}$, where $\mathcal{U}$ is the set of all conceivable control measures. In climate-related problems, for example, $\mathcal{U}$ may denote the set of available climate protection strategies or plausible emissions paths. The relationship between $\mathbf{x}(t)$ and $\mathbf{u}(t)$ is described by a set of differential equations:

$$\dot{\mathbf{x}}(t) = \mathbf{f}(\mathbf{x}(t), \mathbf{u}(t), t) \quad \forall t \in [t_0, t_{end}], \tag{4.1}$$

with initial conditions $\mathbf{x}(t = 0) = \mathbf{x_0}$. In addition, $\mathbf{x}(t)$ may be restricted by a set of prescribed guardrails. These can be imposed on state variables (e.g., the strength of the THC) as well as on control variables (e.g., the rate of emissions reductions; cf. section 4.4). The guardrails can be cast in the form of a set of inequalities:

$$\mathbf{h}(\mathbf{x}(t), \mathbf{u}(t), t) \leq \mathbf{0} \quad \forall t \in [t_0, t_{end}]. \tag{4.2}$$

The goal is the determination of the set of all control measures $\mathbf{u}'(t)$ which simultaneously fulfill Eq. 4.1 and Eq. 4.2. One approach to the problem would be to define various control paths $\mathbf{u}(t) \in \mathcal{U}$, integrate the differential equations over a given period in time and

check whether the corresponding trajectories $\mathbf{x}(t)$ violate the constraints or not. Those control strategies $\mathbf{u}'(t) \in \mathcal{U}$ that keep the system within the guardrails would then, in the climate change example, be eligible as climate policy attaining the predefined targets (e.g., environmental and economic sustainability). This is the method followed by the 'safe landing approach', where the concept of emissions corridors was firstly introduced (Alcamo and Kreileman 1996).

In the framework of the TWA, the problem is posed in inverse terms: *Identify all climate protection strategies, i.e., the complete bundle of admissible control paths* $\mathbf{u}(\cdot)$ *that satisfy simultaneously the predefined constraints Eq. 4.2 subject to the dynamical constraints Eq. 4.1 with initial conditions* $\mathbf{x_0}$.

A suitable mathematical framework for the description of the set-valued solution to this problem is provided by the emerging theory of 'differential inclusions', or 'multi-valued differential equations' (Aubin 1991; Deimling 1992). In the terminology of this theory, the most comprehensive solution to the problem specified by Eqs. 4.1–4.2 is given by the 'bundle of admissible state trajectories' $\mathcal{S}(\mathbf{x_0})$ which can be realized by an underlying 'bundle of admissible control paths' $\tilde{\mathcal{S}}(\mathbf{x_0})$. Unfortunately, for higher dimensional systems the complete and exact determination of these bundles is not feasible at the current state of the mathematical theory. Nevertheless, it is possible to determine specific aspects of the solution bundles.

The methodology currently applied in the TWA focuses directly on these aspects (Bruckner et al. 1999; Bruckner et al. 2003). The set of points ($\mathbf{x}$(t), $\mathbf{u}$(t)) in the combined state and control space that are visited by the bundles $\mathcal{S}(\mathbf{x_0})$ and $\tilde{\mathcal{S}}(\mathbf{x_0})$ is the so-called '(integral state) funnel':

$$\Gamma(\mathbf{x_0}) := \{(\mathbf{x}(t), \mathbf{u}(t)) \mid \mathbf{x}(\cdot) \in \mathcal{S}(\mathbf{x_0}), \mathbf{u}(\cdot) \in \tilde{\mathcal{S}}(\mathbf{x_0}), t \in [t_0, t_{end}]\}. \tag{4.3}$$

The funnel $\Gamma(\mathbf{x_0})$ is the picture that one obtains when all admissible state and control trajectories are plotted simultaneously. The subtle difference between the funnel and the bundle of admissible trajectories is that in the latter case emphasis is placed on the trajectories, whereas in the first case emphasis is on the set of admissible points. In other words, the funnel does not contain information about the dynamics of the system, i.e., about which points are connected by which trajectories. Since the funnel $\Gamma(\mathbf{x_0})$ can be derived without knowing the comprehensive solutions $\mathcal{S}(\mathbf{x_0})$ and $\tilde{\mathcal{S}}(\mathbf{x_0})$, this concept simplifies the problem considerably.

A further possible simplification consists in selecting one component of either the state or control vector and determining the projection of the funnel $\Gamma(\mathbf{x_0})$ onto a plane spanned by time and the respective variable. These projections are called 'necessary corridors'. In the framework of the TWA, the variable usually selected is energy-related CO_2 emissions. The corresponding two dimensional projection is referred to as an 'emissions corridor'.

It should be stressed that the simplified solution procedure described is associated with loss of information. Indeed, the necessary corridors do not contain information about their inner structure. This has the important consequence that the corridors impose a necessary but not a sufficient condition on the admissibility of a particular trajectory: all paths which are compatible with the guardrails lie within the corridor, but not every path which lies within the corridor is necessarily admissible. A concept for constructing sufficient corridors is outlined in Kriegler and Bruckner (2004).

If a corridor is simply connected, it is sufficient to determine its boundary. For two dimensional corridors such as emissions corridors the upper (lower) boundary can be efficiently

computed by maximizing (minimizing) the emissions E successively for fixed points in time $\hat{t} \in \{t_0, t_1, ..., t_n\}$, $t_n \leq t_{end}$ (Leimbach and Bruckner 2001; Bruckner et al. 2003):

$$\text{Maximize (Minimize)} \quad E(t) \mid_{t=\hat{t}} \tag{4.4}$$

subject to the dynamical constraints Eq. 4.1 with initial conditions $\mathbf{x_0}$ and the guardrails expressed by Eq. 4.2. This optimization task can be solved with well established methods of optimal control theory (Papageorgiou 1991).

We calculate the upper and lower corridor boundaries for the period 2000-2100 in time steps of 5 years, i.e., $\hat{t} \in \{2000, 2005, ..., 2100\}$. The time horizon of the optimizations t_{end} is set to 2400 in order to account for the inertia of the ocean and to ensure that an emissions path observing the guardrails in the 21st century does not lead to a violation in the centuries to follow. For the numerical solutions of the optimization problems, the GAMS package (General Algebraic Modeling System; Brooke et al. 1992) is employed.

So far, we have described the algorithm for the calculation of emissions corridors in rather general terms. For its concrete application, one needs to specify the model (i.e., the set of differential equations 4.1) and the guardrails (i.e., the inequalities 4.2).

4.3 Model components

For our analysis, we require a dynamic climate model representing the full causal chain from GHG and aerosol emissions to concentrations, radiative forcing, global mean temperature (GMT) and THC intensity. The link between the latter two is provided by the reduced-form THC model presented in chapter 2. In order to link emissions to GMT we employ the ICLIPS climate model.

4.3.1 The ICLIPS climate model (ICM)

The ICLIPS multi-gas climate model (ICM; Bruckner et al. 2003) is a computationally efficient, globally aggregated model capable of mimicking the transient response of sophisticated carbon-cycle and atmosphere-ocean general circulation models. The model consists of differential equations translating anthropogenic emissions of CO_2, CH_4, N_2O, halocarbons, SF_6, and SO_2 (which make up the control function $\mathbf{u}(t)$ introduced above) into time-dependent paths for concentrations, radiative forcing and GMT (components of $\mathbf{x}(t)$). The output includes transient spatial patterns of relevant impact variables such as temperature, precipitation, cloud cover and humidity changes and transient information about various factors contributing to sea-level rise (thermal expansion of the ocean, melting of glaciers and ice sheets). The spatially explicit information is efficiently constructed by scaling fixed spatial patterns of the respective variable with GMT change. The spatial patterns and the signal's (dimension reduced) time evolution were previously derived by an Empirical Orthogonal Function (EOF) analysis of the results of a climate change simulation with the ECHAM3/LSG GCM (Hooss et al. 1999; Hooss et al. 2001). In the present context, we make use only of the GMT change output provided by ICM.

The core component of ICM is a differential equation analogue to a nonlinear impulse response function (IRF) model of the coupled carbon-cycle-plus-climate system (Hooss et al. 1999; Hooss et al. 2001). Non-linear here means that the differential equations of the IRF model analogue are extended to include nonlinear physical processes, such as the solubility of additional CO_2 in ocean surface waters, the response of primary productivity of land

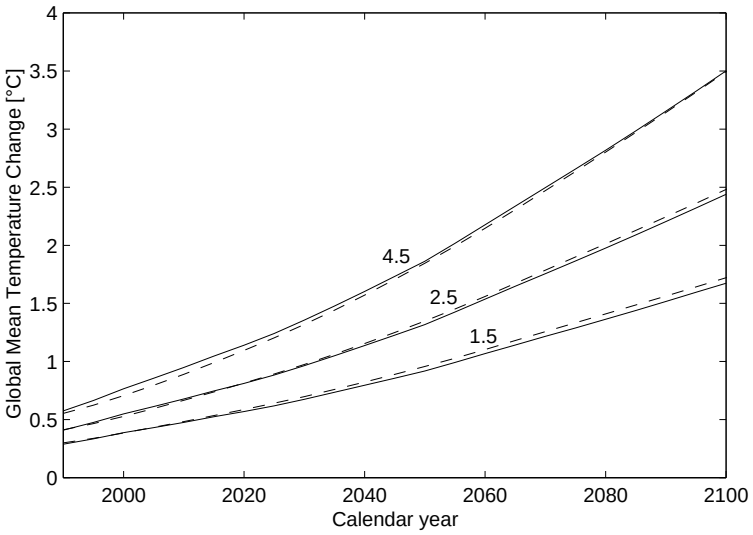

Figure 4.1: Temperature projections for different values of the climate sensitivity $T_{2\times CO_2}$ [°C] following emissions scenario IS92a. The dashed lines are results obtained with the ICLIPS climate model, the solid lines those given in the IPCC Second Assessment Report (Houghton et al. 1995).

vegetation and radiative greenhouse forcing to CO_2, which usually limit the applicability of (linearized) IRF models to concentrations less than twice the preindustrial value (Maier-Reimer and Hasselmann 1987).

For the modeling of the atmospheric chemistry and radiative forcing of major non-CO_2 greenhouse gases (CH_4, N_2O, halocarbons, SF_6, tropospheric and stratospheric O_3, and stratospheric water vapor) and aerosols (originating from SO_2 and biomass burning), various components of MAGICC (Wigley 1994) are incorporated into ICM.

Climate sensitivity

Particularly in view of integrated assessment applications, a crucial requirement on a climate model is that it allows one to explore the sensitivity of the output to the main uncertain quantities. These can be divided into two categories: 'external' factors, such as emissions of greenhouse gases and aerosols, and 'internal' factors comprising the model's parameters and structure. In reduced-form climate models such as ICM, where many of the physical processes are not modeled explicitly, this second class of uncertainties can be subsumed under the climate sensitivity parameter $T_{2\times CO_2}$, which describes the equilibrium global mean temperature response to a doubling of atmospheric CO_2 concentrations. In sophisticated models, the climate sensitivity is obviously not a simple parameter, but a diagnostic quantity which is determined by a range of feedback processes, both positive and negative, involving a number of components of the climate system. Some of these feedbacks are of quite uncertain magnitude, so that the climate sensitivity is only known within a wide uncertainty range. For the set of models listed in the IPCC Third Assessment Report (TAR) this range spans 1.7–4.2 °C (Houghton et al. 2001).

ICM in its standard setup (Bruckner et al. 2003) is calibrated such that a doubling of CO_2 concentrations results in an asymptotic warming of 2.5 °C. For the scope of the analysis presented in this chapter, ICM is extended to allow for the consideration of different

climate sensitivities. This is achieved by relating the near-surface temperature IRF model to a differential box-diffusion model analogue, allowing one to express the (non-physical) IRF parameters as functions of the physical box model quantities, i.e., climate sensitivity, box heat capacities and diffusion coefficients (Kriegler 2001).

The suitability of this method is demonstrated in Fig. 4.1, which displays the response of the full ICM to emissions following the business-as-usual scenario IS92a (Houghton et al. 1992) assuming different values of the climate sensitivity. For comparison, the figure also displays the corresponding projections presented in the IPCC Second Assessment Report (SAR; Houghton et al. 1995). Although being tuned for a fixed climate sensitivity, ICM agrees fairly well in its response with the SAR projections also for other values of this parameter.

4.3.2 Coupling ICM and the reduced-form THC model

ICM and the reduced-form THC model described in chapter 2 are coupled via global mean temperature (GMT) change. The latter drives the THC box model through spatially explicit fluxes of heat and freshwater (cf. section 2.4). By coupling the models in this way, the feedbacks of the THC on GMT is omitted, but this is permissible as argued in the last paragraph of section 2.4. Nevertheless, we disregard also other feedbacks. One of these is the feedback of the THC on the oceanic carbon cycle which can be split into a physical and a biological component. The first refers to the fact that under a weaker THC and hence reduced convective activity less carbon is transported to the deep ocean. On the other hand, a weaker THC would affect the 'biologic pump' (i.e., the removal of CO_2 from the ocean surface layer to the deep ocean through biological activity) by altering the community structure of phytoplankton in the Atlantic. Another feedback involves the oceanic heat uptake: a weaker THC reduces the heat loss from the ocean to the atmosphere and increases the oceanic heat capacity. This, in turn, affects the surface air temperature response, and hence the climate sensitivity (Raper et al. 2002). It should be noted, however, that the feedback of the THC on the oceanic carbon cycle is disregarded in other state-of-the-art reduced-form climate models as well. The feedback on the oceanic heat capacity is considered, for instance, in the so called 'upwelling-diffusion' climate models such as the one included in MAGICC (Raper et al. 1996).

4.4 Specification of guardrails

The objective of our analysis is to identify emissions corridors which preserve the THC while avoiding intolerable burdens of mitigation measures, in accordance with the goals of environmental and socio-economic sustainability stated by Article 2 of the UNFCCC (cf. chapter 1).

In specifying the guardrail compatible with the goal of preserving the THC, we take advantage of the fact that in this system a well-defined threshold exists, beyond which the circulation shuts down. It can be shown analytically that in equilibrium the critical flow (i.e., the flow strength beyond which the circulation cannot be sustained) corresponds to half the equilibrium overturning for zero freshwater forcing (Rahmstorf 1996) and is thus given as 11.3 Sv in our four-box model (cf. Table 2.3). In the transient case this picture changes slightly since, as discussed in section 2.5.4, the critical threshold is dependent upon the rate of climate change (cf. Fig. 2.9). We account for this transient effect and specify the minimum admissible overturning m_{min} as 10 Sv. The guardrail constraining the THC is then cast as:

$$m(t) \geq m_{min} = 10 \text{ Sv} \quad \forall t \in [t_0, t_{end}]. \tag{4.5}$$

In the course of a sensitivity analysis we tighten this constraint by requiring a minimum admissible flow of the THC, expressed in terms of a maximum admissible weakening relative to the present-day value. The assumption of stricter guardrails is justified since already a weakening of the THC may be perceived as an intolerable outcome. In fact, gradual THC changes could trigger singular responses along the impact chain (cf. section 4.5.7).

The socio-economic guardrails are intended to ensure that minimum requirements concerning economic development are met. They are usually cast in terms of maximum admissible welfare loss or minimum per capita consumption (cf. Leimbach and Bruckner 2001, Tóth et al. 2003b). Since our framework so far does not include an integrated model of the energy-economy sector, which is needed to link economic and climatic variables, the expectations about the socio-economically acceptable pace of emissions reductions are expressed in a simplified way by two conditions concerning the flexibility of emissions paths (Kriegler and Bruckner 2004). The first specifies the maximum feasible rate of emissions reductions r:

$$g(t) \geq -r \quad \forall t \in [t_0, t_{end}] \quad \text{with } g(t) := \dot{E}(t)/E(t), \tag{4.6}$$

where $E(t)$ denotes industrial CO_2 emissions.

The maximum emissions reduction rate r can be related to two major drivers of anthropogenic CO_2 emissions: the future level of economic activity and the future state of technology, determining both energy-use efficiency and technological options for energy generation. In the short term, r is determined by the existing energy infrastructure, which has an average turnover time of several decades. In the long run, it is determined by global energy demand. In the literature, estimates of the maximum feasible emissions reduction rate r range from 0.5 to 3% per year (for a review cf. Alcamo and Kreileman 1996). After a detailed analysis of scenarios of technological change in the energy sector, Alcamo and Kreileman (1996) conclude that "in order to achieve global annual emissions reduction rates of more than 2%, substantial policy measures are required, even in the case of optimistic assumptions on technological change. ... It is therefore highly uncertain that rates of around 2% per year or higher can be maintained over such long periods of time [i.e., from 2010 to 2100]". For our analysis, we have chosen a default value of 1.5% per year.

The second condition addresses socio-economic inertia by imposing a smoothness constraint on the transition to a decarbonizing economy (i.e., an economy where carbon emissions decrease in absolute terms). This is achieved by requiring a minimum time span t_{trans} for switching from today's economic regime with increasing emissions to a regime where emissions decrease with the maximum reduction rate r. This constraint is motivated by evidence that emissions pathways allowing for a more gradual near-term transition away from carbon-venting fuels result in lower mitigation costs. One reason for this is the turnover time of the energy converting capital stock (e.g., power plants, buildings, transport systems) mentioned above. Another reason is that the availability of low-cost technological options depends on investments into 'research and development' (R&D) and on 'learning by doing' (Metz et al. 2001). Watson et al. (1996), for example, report that the time required to put in place optimal technology for deep cuts in CO_2 corresponds to approximately 50 years. We use a default minimum transition time t_{trans} of 20 years, which may thus be considered as a rather restrictive value.

Finally, we introduce a 'monotony' condition which allows growing CO_2 emissions to be followed by a reduction period, but not viceversa. For technical reasons we formulate this constraint even stronger by requiring that the emissions growth rate g decreases monotonously in time, with a maximum emissions growth rate g_0 in the year 2005. As pointed out in Kriegler

and Bruckner (2004), this constraint is rather strong as it excludes emissions trajectories where the emissions growth rate itself grows after 2005. This would be the case, e.g., for emissions scenarios which assume a switch to coal after the exploitation of oil and gas reserves, as is the case in some of the SRES emissions scenarios (Nakićenović and Swart 2000). The majority of these scenarios, however, complies with the constraint.

We combine the 'monotony' condition and the constraint on the transition time into a single inequality:

$$-\frac{g_0 + r}{t_{trans}} \leq \dot{g}(t) \leq 0 \quad \forall t \in [t_0, t_{end}]. \tag{4.7}$$

Note that for vanishing transition times t_{trans} the change in the growth rate g is almost unlimited from below, allowing for a sudden switch in the emissions pathway (cf. Fig. 4.10).

4.5 Results

In the following, we present emissions corridors compatible with the goal of preserving the THC while keeping the pace of greenhouse gas mitigation at a bearable level. First, we show the emissions corridor for standard model settings (section 4.5.1). We then discuss the results of a sensitivity analysis with respect to the main uncertain model parameters, such as climate sensitivity (section 4.5.2), North Atlantic hydrological sensitivity (section 4.5.3), emissions of non-CO_2 greenhouse gases (section 4.5.5) and sulfate aerosols (section 4.5.6). Lastly, we explore the dependence of the shape of the emissions corridors on the guardrails (i.e. minimum intensity of the THC, maximum emissions reduction rate, transition time towards a decarbonizing economy; sections 4.5.7 and 4.5.8).

The standard values of the uncertain parameters as well as the ranges within which they are varied in the course of the sensitivity analysis are given in Table 4.1. Note that the standard value for the hydrological sensitivity of 0.03 Sv/°C is larger than the value indicated in Table 2.4. The higher choice is motivated by the fact that the North Atlantic hydrological sensitivity derived from CLIMBER-2 is low compared to the values diagnosed in other models, as discussed in section 2.5.2. As standard we thus adopt a value which lies in the middle of the plausible range.

For the calculation of emissions corridors we need to specify scenarios for the CO_2 emissions from land-use change (recall that the control variable are energy-related CO_2 emissions only) and emissions of non-CO_2 greenhouse gases and aerosols. For the greenhouse gas emissions during the 21st century we make use of the scenarios developed by the IPCC in its Special Report on Emissions Scenarios (SRES; Nakićenović and Swart 2000). In this report, 40 emissions scenarios belonging to 4 scenario 'families' are presented. Scenarios pertaining to the same family share common assumptions about the main driving forces of greenhouse gas emissions, such as demographic change, social and economic development and technological change. From each family, one representative emissions paths is selected as 'illustrative marker scenario' (denoted as B1, B2, A1B and A2 scenario, respectively). In the present study it is assumed that CO_2 emissions from land-use change and emissions of non-CO_2 greenhouse gases follow the average of these four marker scenarios until 2100. From 2100 until 2400 (i.e., the time horizon of the optimization) these emissions are held constant. This is a rather strong assumption which can only be motivated by the lack of coherent scenarios for the time after 2100. Therefore, in section 4.5.5 we explore the sensitivity of the emissions corridors to alternative assumptions concerning long-term emissions of land-use change related CO_2 and non-CO_2 greenhouse gases.

Parameter	Standard value	Range
Hydrological sensitivity:		
h_2	0.03 Sv°C^{-1}	0.01 – 0.05 Sv°C^{-1}
Climate sensitivity:		
$T_{2\times CO_2}$	2.5 °C	1.5 – 4.5 °C
Guardrails:		
m_{min}	10 Sv	60 – 90% $m(2000)$
r	0.015 yr^{-1}	0.005 – 0.025 yr^{-1}
t_{trans}	20 yrs	0 – 40 yrs
Non-CO_2 GHGs :		
emissions scenario	mean of B1, B2, A1B, A2	B1, B2, A1B, A2
Desulfurization rate :		
ds	1.5% yr^{-1}	0 – 3% yr^{-1}

Table 4.1: Elements of the sensitivity analysis.

In contrast to major non-CO_2 greenhouse gases such as CH_4 and N_2O which are to a large extent biogenic, sulfate aerosols originate mainly from the burning of fossil fuels. We therefore link SO_2 emissions $E(SO_2, t)$ to the control variable, i.e., energy-related CO_2 emissions $E(CO_2, t)$. Because of the increasing control of sulfur emissions by end-of pipe technologies due to the recognition of their negative effects on human health, food production and ecosystems, it is reasonable to assume that over the long term SO_2 emissions will become independent from CO_2 emissions. This assumption is implemented in our model by introducing a so-called 'desulfurization rate' ds:

$$\frac{E(SO_2, t)}{E(SO_2, t')} = \frac{E(CO_2, t)}{E(CO_2, t')}(1 - ds)^{dt}, \tag{4.8}$$

where $t' < t$ and $dt = t - t'$. In our standard case we assume a globally averaged desulfurization rate of 1.5% per year.

4.5.1 Emissions corridor for standard parameter values

The corridor for standard parameter settings is displayed in Fig. 4.2, along with selected emissions paths to illustrate its internal structure. The corridor boundaries demarcate emissions limits beyond which either the THC collapses or the socio-economic guardrails are violated. It should be re-emphasized that emissions corridors impose only a necessary condition on the admissibility of a particular emissions path, implying that not every single path within the corridor is necessarily admissible. For example, the upper boundary of the corridor can be reached in 2060 only if emissions remain far inside the corridor for several decades in the first half of the 21st century.

For purpose of reference, Fig. 4.2 also displays representative low and high CO_2 emissions scenarios (SRES scenario B1 and A2, respectively). Our results indicate that for standard parameter values the emissions corridor is wider than the range spanned by the SRES marker scenarios. This result might suggest that no immediate mitigation effort would be necessary

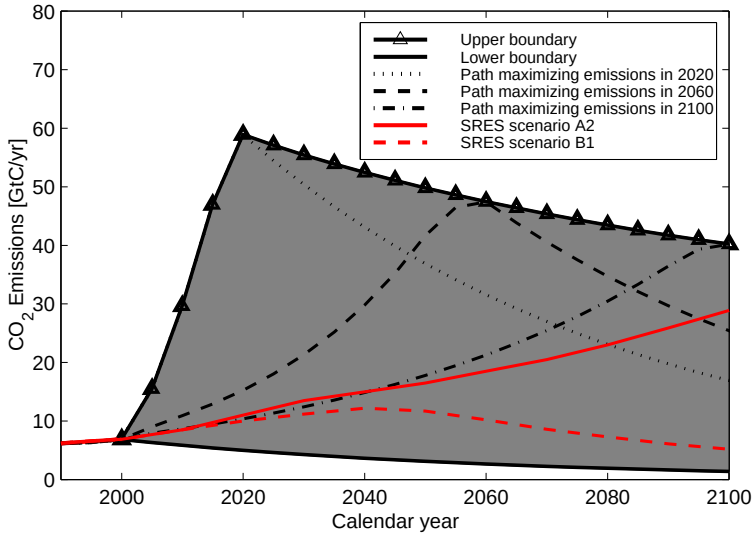

Figure 4.2: Emissions corridor – the shaded area between upper and lower boundaries – for standard parameter settings (cf. Table 4.1). For an illustration of its internal structure, we show paths maximizing CO_2 emissions in 2020, 2060, and 2100. For reference, we also display representative low and high emissions scenarios (SRES marker scenarios B1 and A2, respectively).

in order to preserve the THC. In the following, however, we show that this result is very sensitive to the specific assumptions concerning climate and hydrological sensitivity.

Fig. 4.3 illustrates the constraints which the guardrails impose on CO_2 concentrations and global mean temperature. Fig. 4.3a shows the paths maximizing emissions in the years 2020, 2060 and 2100. Figs. 4.3b–d display the resulting CO_2 concentrations, changes in global mean temperatures and thermohaline circulation intensities. It is evident that in order to keep the THC within the guardrails (i.e., above the critical flow of 10 Sv), the change in global mean temperature has to be stabilized at 5.5 °C. In terms of CO_2 concentrations this means a maximum of approximately 1300 ppm reached during the 22$^{\text{nd}}$ century and a slight decline thereafter. A notable feature is the considerable lag between the time of maximum CO_2 emissions and that of maximum weakening of the THC: the emissions paths peaking during the 21$^{\text{st}}$ century lead to transient THC responses reaching their minima about two centuries later.

4.5.2 Emissions corridors for different values of the climate sensitivity

Fig. 4.4 displays emissions corridors for different values of the climate sensitivity $T_{2\times CO_2}$. This parameter is varied in the range from 1.5 to 4.5 °C (with all other parameters at their standard values), which is the uncertainty range specified by the IPCC (Houghton et al. 1995; Houghton et al. 2001). Note, however, that in recent studies this uncertainty range is extended considerably towards higher values (Andronova and Schlesinger 2001; Knutti et al. 2002; Forest et al. 2002).

Our findings indicate a very strong dependence of the width of the emissions corridor on climate sensitivity. This change in width is determined only by a shift in the position of the upper corridor boundary, as the lower boundary is determined by the maximum emissions reduction rate r and is thus the same for all values of climate sensitivity. For a value of

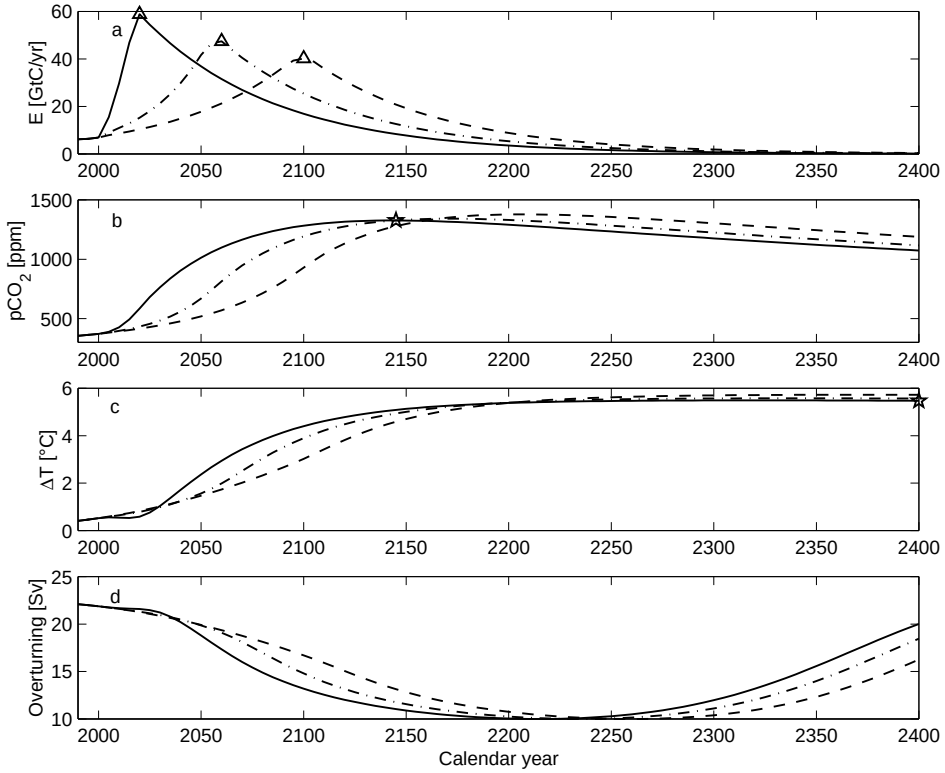

Figure 4.3: a) Paths maximizing CO_2 emissions in 2020, 2060, 2100 (solid, dashed-dotted and dotted lines, respectively). The triangles mark the points (maxima) that determine the upper corridor boundary in Fig. 4.2. b) CO_2 concentrations resulting from the emissions paths in a). c) Changes in global mean temperature relative to pre-industrial (under inclusion of the radiative forcing from non-CO_2 greenhouse gases and aerosols). d) Thermohaline overturning intensities. The stars in b) and c) denote the maximum CO_2 concentration (pCO_2^{max}) and the stabilization temperature (T^{2400}) for the path maximizing CO_2 emissions in 2020, respectively.

1.5 °C, the corridor widens significantly (by 250%[2]) relative to the corridor for standard assumptions, such that its upper boundary is far from being touched by any of the SRES emissions scenarios for the 21st century. On the other hand, for climate sensitivities of 3.5 and 4.5 °C the corridor shrinks (by 38% resp. 55%), and the high reference emissions scenario (SRES marker scenario A2) crosses the upper corridor boundaries in the second half of the 21st century. It should be emphasized that a transgression of the corridor boundaries does not imply an immediate collapse of the THC: because of the inertia of the ocean (cf. Fig. 4.3), the actual event occurs centuries after it has been triggered. Once the corridor boundaries are transgressed, however, a collapse of the THC is inevitable.

Two mechanisms contribute to the reduction of the corridor with increasing climate sensitivity: the differential warming between the southern and the northern boxes (cf. Table 2.4), and the enhanced freshwater transport towards the northern latitudes, which increases with rising global mean temperature (cf. Eq. 2.27). Both act to reduce the meridional density gradient which drives the THC and thus bring the latter closer to the stability threshold.

[2]As measure for the width of emissions corridors we take the maximum of the upper corridor boundary. Relative changes relate to this measure.

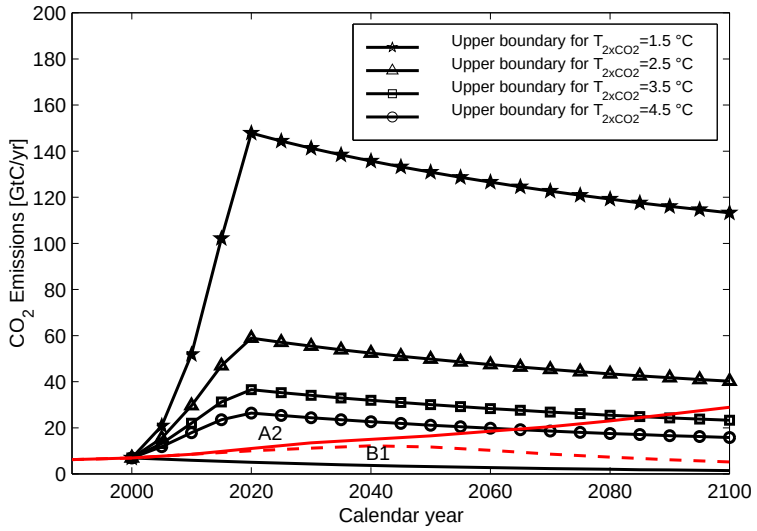

Figure 4.4: Emissions corridors for different values of the climate sensitivity $T_{2\times CO_2}$.

4.5.3 Emissions corridors for different values of the North Atlantic hydrological sensitivity

In further experiments, we computed emissions corridors for different values of the North Atlantic hydrological sensitivity h_2, which is varied in the range from 0.01 to 0.05 Sv/°C (for a justification of this range see section 2.5.2). The resulting emissions corridors are shown in Fig. 4.5. As for climate sensitivity, the size of the emissions corridors is largely dependent on the specific parameter choice: for low values of h_2 the corridor is much larger than the range spanned by the SRES emissions scenarios, while for high values SRES emissions scenario A2 transgresses the upper corridor boundary in the second half of the 21$^{\text{st}}$ century. This strong sensitivity of the THC to the value of the North Atlantic hydrological sensitivity h_2 was already evident in Fig. 2.9: the higher h_2, the lower the temperature increase and thus the CO_2 load of the atmosphere that can be reached if the THC is to be kept in the stable domain.

4.5.4 Aggregated sensitivity analysis

So far we have restricted our discussion to single parameter sensitivity analysis whereby we varied one parameter while keeping all others at their standard values. In Table 4.2 we present the results of an aggregated sensitivity analysis for the parameter constellations $T_{2\times CO_2} \in \{1.5, 2.5, 3.5, 4.5\ ^\circ\text{C}\} \times h_2 \in \{0.01, 0.02, 0.03, 0.04, 0.05\ \text{S}v/^\circ\text{C}\}$. In order to synthesize the results, it is useful to define an indicator which captures the essential information contained in emissions corridors. As such we have chosen maximum admissible cumulative emissions in 2100 (E^{cum}) (cf. Kriegler and Bruckner 2004). Obviously this indicator does not convey the full information carried by emissions corridors such as, e.g., the shape of the corridor boundaries, but it provides an intuition of the maneuvering space for CO_2 emissions in the 21$^{\text{st}}$ century. Interestingly, for each parameter constellation the path maximizing cumulative emissions in 2100 corresponds to that maximizing annual CO_2 emissions in 2020 (cf. Fig. 4.2). This is due to a peculiarity in the response of the carbon cycle: the faster a given amount

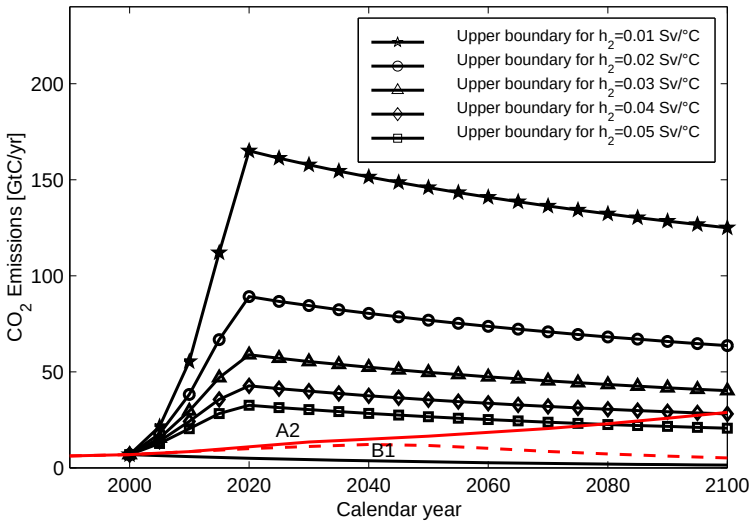

Figure 4.5: Emissions corridors for different values of the North Atlantic hydrological sensitivity h_2 (with all other parameters at their standard values).

of CO_2 is released to the atmosphere, the higher the fraction of atmospheric carbon which is taken up by the ocean (cf. Edmonds and Wise 1998). Along with E^{cum} we display the corresponding maximum CO_2 concentration (pCO_2^{max}) and stabilization temperature (T^{2400}) (for a definition of pCO_2^{max} and T^{2400} cf. Fig. 4.3 and related discussion). It must be emphasized, however, that these two values are given for illustrative purposes only, and are not central results of our analysis. Table 4.2 shows that the sensitivity of E^{cum} to both climate and hydrological sensitivity is large and of comparable magnitude for both quantities. For the 'best case' combination of model parameters (i.e., $T_{2\times CO_2}$=1.5 °C, h_2=0.02 Sv/°C), for example, E^{cum} amounts to 14052 GtC compared to the 870 GtC for the 'worst case' combination ($T_{2\times CO_2}$=4.5 °C, h_2=0.05 Sv/°C). The cumulative emissions in 2100 associated with the A2 and B1 scenarios amount to 1701 GtC and 920 GtC, respectively. According to these numbers, the A2 scenario would lead to an exceedance of the admissible carbon load for high climate and medium to high hydrological sensitivities (cf. Table 4.2). The B1 scenario would lead to a transgression of the guardrails for 'worst case' parameter assumptions only. It must be recalled, however, that in considering maximum cumulative emissions in 2100, information is omitted about the time-dependence of admissible emissions paths. If this information is taken into account, the parameter ranges for which the A2 scenario transgresses the upper corridor boundary are enlarged to include the combinations 4.5 °C, 0.02 Sv/°C; 3.5 °C, 0.03 Sv/°C; 2.5 °C, 0.05 Sv/°C for climate resp. hydrological sensitivity.

The stabilization temperature T^{2400} (i.e., the value at which GMT change has to be stabilized for a collapse of the THC to be avoided) ranges from 3.9 °C for the highest to 9.2 °C for the lowest value of the hydrological sensitivity. The values of T^{2400} are largely insensitive to climate sensitivity since the crucial quantity in determining the response of the THC, i.e., North Atlantic heat and freshwater forcing, depends solely on the amount of temperature increase and not on CO_2 concentrations. The slight differences arise because of transient effects associated with the sensitivity of the THC to the rate of temperature change (for higher $T_{2\times CO_2}$ the initial temperature response is slightly slower).

$T_{2\times CO_2}$ [°C]	h_2 [Sv/°C]					
	0.01	0.02	0.03	0.04	0.05	
1.5	-	14052	8050	5484	4100	E^{cum} [GtC]
	-	6646	3478	2242	1633	pCO_2^{max} [ppm]
	-	6.9	5.6	4.6	3.9	T^{2400} [°C]
2.5	8952	4960	3345	2473	1923	E^{cum} [GtC]
	3935	2005	1326	1002	817	pCO_2^{max} [ppm]
	9.2	6.9	5.5	4.5	3.9	T^{2400} [°C]
3.5	5033	3069	2140	1591	1224	E^{cum} [GtC]
	2037	1220	888	714	609	pCO_2^{max} [ppm]
	9.2	6.9	5.5	4.6	4.0	T^{2400} [°C]
4.5	3597	2265	1583	1161	870	E^{cum} [GtC]
	1426	930	712	592	517	pCO_2^{max} [ppm]
	9.2	7.0	5.6	4.8	4.2	T^{2400} [°C]

Table 4.2: Maximum cumulative emissions in 2100 (E^{cum}), associated maximum CO_2 concentrations (pCO_2^{max}) and stabilization temperatures (T^{2400}) for the parameter constellations $T_{2\times CO_2} \in \{1.5, 2.5, 3.5, 4.5\} \times h_2 \in \{0.01, 0.02, 0.03, 0.04, 0.05\}$. For the parameter combination $T_{2\times CO_2} = 1.5$ °C, $h_2 = 0.01$ Sv/°C these quantities are not given since the associated allowable emissions exceed the domain of applicability of the coupled-carbon-cycle-plus-climate-model.

4.5.5 Sensitivity of the corridors to emissions of non-CO_2 greenhouse gases

In a set of simulations we investigated the influence of different assumptions concerning CO_2 emissions from land-use change and emissions of non-CO_2 greenhouse gases (GHGs) on the shape of the emissions corridors. We recall the standard assumption (cf. Table 4.1) that these emissions follow the average of the four SRES marker scenarios until 2100 and are held constant thereafter. In a first set of model runs we assume that emissions of CO_2 from land-use change and non-CO_2 GHGs follow one of the SRES marker scenarios B1, B2, A1B and A2 until 2100 and are constant thereafter. Subsequently, we explore the sensitivity to this constant assumption by projecting alternative storylines spanning the 22$^{\text{nd}}$, 23$^{\text{rd}}$ and 24$^{\text{th}}$ century.

Fig. 4.6 displays emissions corridors for CO_2 from land-use change and non-CO_2 GHGs following the single SRES marker scenarios. The corridor for our standard assumption is not displayed as it is almost identical to the corridor for the B2 scenario. The sensitivity of the corridor to the specific scenario is significant, although not as large as in the case of climate or hydrological sensitivity (cf. Fig. 4.4 and Fig. 4.5). For the B1 scenario, where emissions of the most influential non-CO_2 GHGs CH_4 and N_2O are lowest, the corridor is increased by 15% as compared to the standard case. In contrast, for the A2 scenario where emissions of CH_4 and N_2O increase strongly throughout the 21$^{\text{st}}$ century, the corridor is reduced by 20%. Note that the B2 scenario leads to a narrower corridor than the A1B scenario, contrarily to what one might expect on the basis of the respective CO_2 emissions (which are lower for the B2 than for the A1B scenario). The reason are much higher CH_4 emissions in the B2 scenario as compared to the A1B scenario. Note also that for non-CO_2 GHGs following the A2 scenario the reference CO_2 emissions scenario A2 approaches the upper corridor boundary rather closely. This means that if CO_2 *and* non-CO_2 GHGs will follow the A2 storyline, a collapse of the THC could be triggered in the first years of the 22$^{\text{nd}}$ century.

As already mentioned, the assumption that emissions of CO_2 from land-use change and

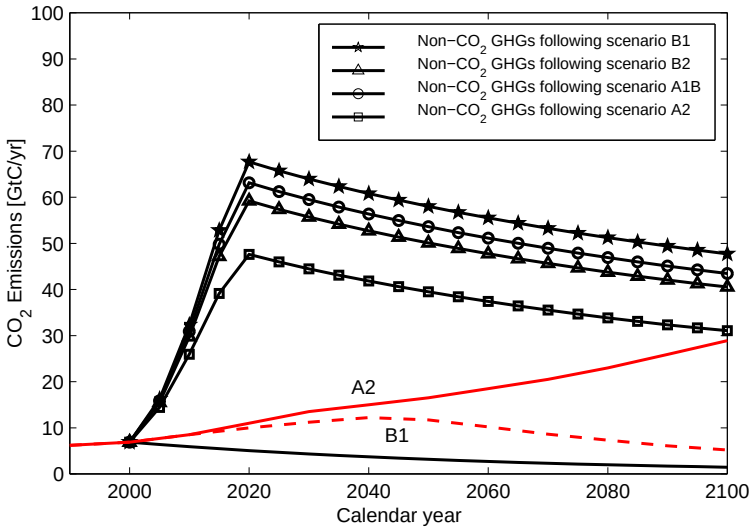

Figure 4.6: Corridors for different assumptions concerning emissions of CO_2 from land-use change and non-CO_2 greenhouse gases.

non-CO_2 GHGs stay constant after 2100 can be motivated solely by the lack of more plausible alternatives. We therefore developed three different scenarios for emissions of these gases after 2100:

1. Emissions of non-CO_2 GHGs are coupled to energy-related CO_2 emissions[3].

2. Emissions of non-CO_2 GHGs follow the average of the SRES marker scenarios until 2100 and are coupled to energy-related CO_2 emissions thereafter.

3. Emissions of non-CO_2 GHGs follow the average of the SRES marker scenarios until 2100 and then proceed according to their trend in the second half of the 21st century.

In all three cases, emissions of CO_2 from land-use change follow our standard scenario. Note that in comparison to emissions of non-CO_2 GHGs such as CH_4 and N_2O land-use change emissions play only a minor role.

In a set of experiments we explored the sensitivity of the emissions corridor to these alternative scenarios. The tightest corridor arises from scenario 1: the area of the corridor is decreased by 16% compared to the standard case. The reason is that in this case emissions of non-CO_2 GHGs reach rather high values in the first half of the 21st century, as they are coupled to energy-related CO_2 emissions which are maximized in order to determine the upper corridor boundary. The largest corridor is generated by assuming scenario 2: the corridor is increased by 14% compared to the standard case. This increase is due to the fact that emissions of non-CO_2 GHGs decline rapidly after 2100 such that higher CO_2 emissions can be attained before 2100. Scenario 3 gives rise to a corridor which differs little compared to the corridor for standard assumptions.

[3]Ideally, only the energy-related fractions should be coupled to the control variable. Unfortunately, the SRES database does not allow one to discriminate between energy and non-energy related emissions of non-CO_2 GHGs.

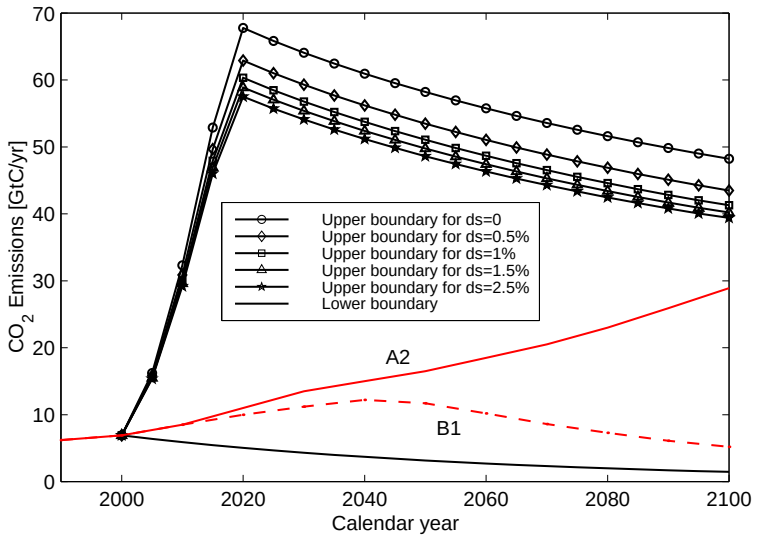

Figure 4.7: Emissions corridors for different assumptions concerning the desulfurization rate *ds*.

4.5.6 Sensitivity of the corridors to SO_2 emissions

In the following we discuss the sensitivity of emissions corridors to different assumptions concerning sulfur dioxide (SO_2) emissions. We recall that these emissions are linked to energy-related CO_2 emissions (i.e., the control variable) assuming a globally averaged desulfurization rate *ds* of 1.5%. In the course of a sensitivity analysis, we vary this quantity between 0 and 3% per year. The resulting emissions corridors for *ds*=0–2.5% are displayed in Fig. 4.7 (note that the corridor for *ds*=3% is not displayed as it almost coincides with that for *ds*=2.5%). We find that the width of the emissions corridor decreases with increasing desulfurization rate. This can be explained as follows: because of the short residence time of sulfate (SO_4) aerosols (which are produced by the oxidation of SO_2) in the atmosphere, high *ds* is associated with a fast removal of the 'aerosol mask' which, in turn, leads to faster and stronger warming[4]. This implies that the maximum CO_2 emissions that can be attained are lower in the case of a higher desulfurization rate. The specific dependence of the position of the upper corridor boundary on *ds* is a result of the sensitivity of the THC to the rate of climate change (cf. section. 2.5.4): the higher *ds* and thus the rate of temperature change, the lower the maximum temperature which can be attained if the THC is to be kept in the present-day mode of operation.

4.5.7 Sensitivity of the corridors to the THC guardrail

So far, we have considered only a complete shutdown of the THC as a possibly unacceptable outcome that should be avoided in the sense of Article 2 of the UNFCCC. It is conceivable, however, that already a weakening of the THC (which is the response most models project for the 21st century; cf. Houghton et al. 2001) might have considerable impacts, at least on the North Atlantic itself. Indeed, a slowdown of the THC would be associated with changes in the physical properties of the North Atlantic waters, such as, e.g., salinity, temperature, and mixed layer depth. This could affect marine ecosystems at all trophic levels with possible repercussions on the oceanic carbon cycle and fisheries (Rahmstorf et al. 2003). Furthermore,

[4]Recall that the radiative forcing of sulfate aerosols is negative in sign.

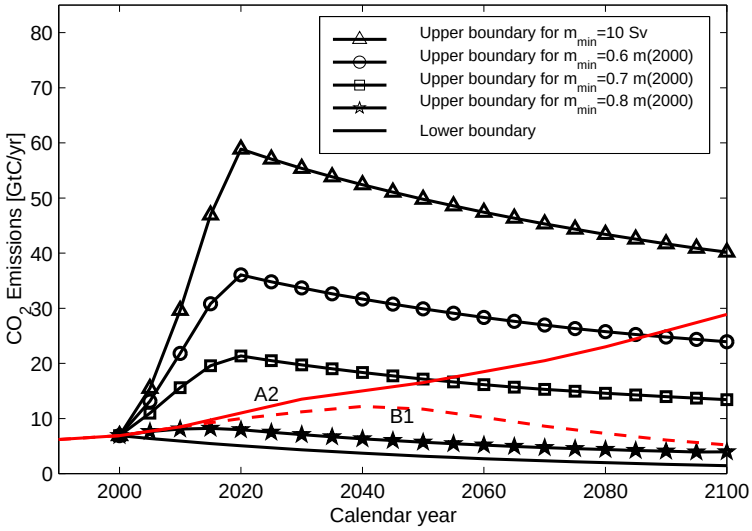

Figure 4.8: Emissions corridors for different assumptions about the THC guardrail expressed in terms of the minimum admissible circulation rate m_{min}. All other parameters are kept at their standard values.

it cannot be excluded that gradual changes in the THC could force these systems across some threshold and hence generate singular responses. On these grounds, one might pursue a more ambitious policy target limiting changes in the THC to a specific amount of weakening relative to the present-day value.

In the following we discuss the sensitivity of the emissions corridor to the THC guardrail m_{min}, which is varied in the range of 60–90% of present-day circulation intensity $m(2000)$. This corresponds to a maximum admissible weakening of the THC of 40–10%. Our results suggest that the width of the emissions corridor depends strongly on the specific policy target. Fig. 4.8 shows that while the maneuvering space for the standard case $m_{min} = 10$ Sv is comfortable, it becomes considerably tighter if m_{min} is increased. Indeed, for $m_{min} = 0.7 \cdot m(2000)$ (i.e., a maximum admissible weakening of the THC of 30%) the high reference scenario A2 leaves the corridor in the mid-century. For $m_{min} = 0.8 \cdot m(2000)$ even the low non-intervention emissions scenario B1 leaves the corridor area in the early years of the 21st century, implying that it would be impossible to attain the target under a business-as-usual emissions regime. For $m_{min} = 0.9 \cdot m(2000)$ no emissions corridor exists. This implies that, given the amount of greenhouse gases already in the atmosphere and the inertia of the climate system, it is not feasible to limit changes in the THC to a 10% weakening under the prescribed socio-economic constraints. The emissions corridor could be 'opened' if mitigation options for non-CO_2 greenhouse gases were considered or the expectations about the socio-economically acceptable pace of CO_2 emissions reduction were relaxed (i.e., t_{trans} decreased and r increased; cf. next section).

4.5.8 Sensitivity of the corridors to the socio-economic guardrails

Fig. 4.9 shows emissions corridors for different values of the maximum feasible emissions reduction rate r (cf. Eq. 4.6). Besides affecting the position of the upper boundary, r is the sole determinant of the shape of the lower corridor boundary: the latter corresponds to a path

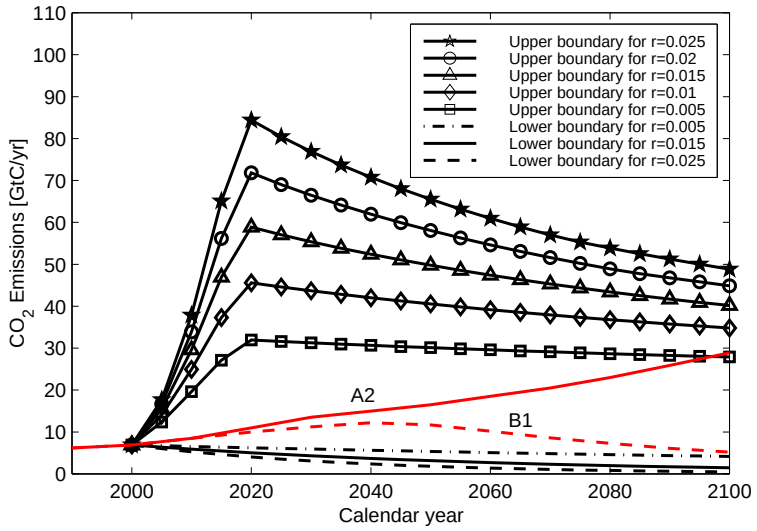

Figure 4.9: Emissions corridors for different assumptions about the maximum admissible emissions reduction rate r. All other parameters are kept at their standard values.

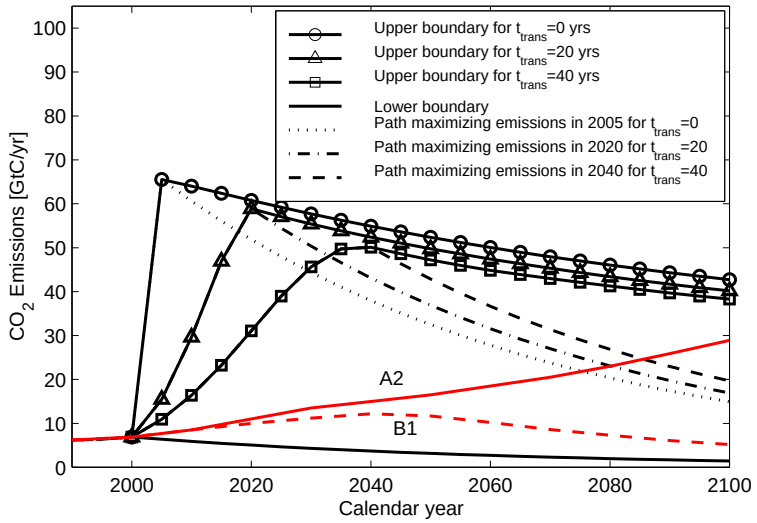

Figure 4.10: Emissions corridors for different assumptions about the transition pace towards a decarbonizing economy t_{trans}. All other parameters are kept at their standard values.

with emissions decreasing exponentially at a rate r. Although the overall width of the emissions corridor is mainly determined by the upper boundary, the shape of the lower boundary is crucial in the case of very tight emissions corridors. For the case $m_{min} = 0.8 \cdot m(2000)$ discussed in the previous section, for example, the corridor would vanish for a lower value of r (precisely for r=0.005 yr^{-1}). The considerable increase of the width of the emissions corridors with increasing r can be explained with the higher flexibility associated with it. Indeed, the additional leeway is due to emissions paths which take advantage of the fast reduction capacity to attain high emissions in the short term.

Fig. 4.10 shows emissions corridors for different values of the transition time t_{trans}, which

is an expression of the inertia characterizing the transition to a decarbonizing economy (cf. section 4.4). We found that t_{trans} determines the shape of the emissions corridor mainly in the first decades of the 21st century, while its effect is relatively small thereafter. The additional leeway for the case $t_{trans} = 0$ in relation to the standard case $t_{trans} = 20$, for example, is due to emissions paths which jump from maximally increasing to maximally decreasing emissions (i.e, from g_0 to r in Eq. 4.7; cf. Fig. 4.10).

Kriegler and Bruckner (2004) use the pertinent metaphor of a ships passage to illustrate the different role of the socio-economically motivated constraints and the other guardrails and parameters in determining the shape of the emissions corridors: "The latter affect the maneuvering space by determining the coast lines of the passage, while the former affect the maneuvering space by determining the maneuvering capacity of the ship".

The findings presented in this chapter and the resulting conclusions will be summarized in chapter 5.

Chapter 5

Summary and Conclusions

The scope of this thesis is the development and application of reduced-form models of two representative large-scale singular events that could potentially be triggered in the wake of anthropogenic climate change. These are the nonlinear response of the Atlantic thermohaline circulation (THC) and the transformation of the Indian monsoon. The models are conceived so as to fulfill the main requirements of integrated assessment (IA) modeling, which may be subsumed under the attributes reliability, high computational efficiency, flexibility and transparency. We have employed the so designed models for sensitivity studies, qualitative analysis and integrated assessment, demonstrating their value for a broad range of applications.

5.1 Reduced-form modeling of the THC

One part of this thesis is devoted to the development and characterization of a reduced-form model of the Atlantic THC. The model is an interhemispheric four-box model calibrated against results obtained with a state-of-the-art climate model of intermediate complexity (Petoukhov et al. 2000; Ganopolski et al. 2001). Our model is designed to be forced by scenarios of global mean temperature change, which are translated into transient fluxes of heat and freshwater through an appropriate down-scaling procedure.

The specific design and computational efficiency of the model allowed us to perform a large number of sensitivity experiments with respect to uncertain model and forcing parameters. We devoted particular attention to the hydrological forcing, which is among the major uncertain factors determining the response of the THC to climate change. We further analyzed the response of the THC to different regional patterns of warming, rates of climate change and initial model states.

Although highly simplified compared to comprehensive climate models (Earth system models of intermediate complexity and three-dimensional general circulation models), the reduced-form model is shown to reproduce their key sensitivities. In response to a $4\times CO_2$ stabilization scenario and weak hydrological forcing, for example, the THC first weakens and then recovers. For strong hydrological forcing (i.e., North Atlantic freshwater forcing exceeding 0.22 Sv), the circulation collapses. The threshold value is found to be sensitive to the spatial distribution of the heat and freshwater forcing, the rate of climate change and the initial (i.e., present-day) circulation intensity.

Besides demonstrating the ability of the box model to reproduce key aspects of the behavior of comprehensive models, these experiments have a value on their own. In fact, they

allow one to explore the sensitivity of the THC to a number of uncertain factors in a systematic and consistent way. Our results suggest that the strongest sensitivity is to the Atlantic hydrological forcing. The latter is a function of two underlying quantities: the magnitude of temperature change (determined by the climate sensitivity) and the hydrological sensitivity. Both quantities are highly uncertain. The rate of climate change also plays a role, but not as large as the factors described above. If the hydrological forcing is low, faster rates of change alone do not have the potential to bring the THC across the critical threshold. If the system, however, is already in the proximity of that threshold, the rate of change becomes crucial for determining whether the THC collapses or not. The significance of these sensitivities for the design of climate protection strategies which aim at avoiding a shutdown of the THC will be discussed in section 5.3.

One might argue that the reduced-form model, which is purely advective, would gain credibility through the inclusion of additional physical processes such as convection, small-scale turbulent mixing and the wind-driven gyre circulation. We therefore explored the performance of the box model under inclusion of simple parameterizations of these physical mechanisms. Our results suggest, for example, that the implementation of vertical mixing across the thermocline enhances the sensitivity of the THC to freshwater forcing. This is in contrast to results obtained with two and three-dimensional ocean models (Schmittner and Weaver 2001; Prange et al. 2003) where vertical mixing acts to stabilize the circulation. This challenges the view that a model as simple as ours would necessarily benefit from the inclusion of additional physics. We are of the opinion that such a reduced-form model is a valid explorative tool only if conceived as 'emulator' of comprehensive ocean models. As such, it is desirable to keep the number of its tunable parameters as low as possible. Also, the inclusion of vertical and horizontal mixing would be at the expense of the mathematical simplicity and overall transparency of the model, which we strongly exploited for the design of the parameter fitting procedure and the interpretation of the sensitivity experiments.

We conclude that our approach to use a dynamic four-box model of the Atlantic to mimic the response of the THC as simulated by comprehensive climate models was successful. We think that our model represents a useful tool for exploring the basic physical mechanisms underlying the response of the THC to climate change. Further, the model has proven to be fast, transparent and flexible, meeting the main requirements of interdisciplinary applications such as integrated assessment modeling.

5.2 Reduced-form modeling of the Indian monsoon

In this thesis, we presented a novel reduced-form model of the Indian monsoon. It is a one-dimensional box model of the tropical atmosphere including parameterizations of the radiative and surface fluxes, the hydrological cycle and surface hydrology. Despite its simplicity, the model satisfactorily reproduce key features of the observed monsoon dynamics such as the annual course of precipitation and the transitions between winter and summer regimes. The major shortcoming of the model is that temperature over India is too high. Probably as a consequence, winter precipitation is stronger than observed and the summer monsoon sets on two weeks earlier. These deficiencies, however, could probably be smoothed out by extending the number of tunable model parameters which has so far been restricted.

In view of integrated assessment applications, it is of central concern that the reduced-form model be able to reliably simulate the response of the Indian monsoon to increased GHG and sulfur emissions. For the purpose of validation, we performed a number of climate

change experiments and compared the findings obtained with our model to those known from studies with more complex models. Results of a set of GHG experiments indicate that under $2\times CO_2$ and $4\times CO_2$ conditions, summer precipitation over India increases. This occurs despite a slight weakening of the land-ocean temperature contrast and hence a slackening of the monsoon circulation. The reason is higher humidity over the oceans which leads to increased landward advection of moisture. The qualitative picture and the magnitude of the changes are consistent with recent findings of studies employing GCMs. Results of a set of aerosol experiments indicate that under enhanced atmospheric sulfate loading alone, summer precipitation is reduced considerably. The reason is the cooling of the Indian subcontinent relative to the adjacent oceans. If $2\times CO_2$ conditions are applied simultaneously to the higher sulfate loading, the summer precipitation is still weaker than under present-day conditions. CO_2 concentrations have to be almost quadrupled in order to compensate the effects of the scattering aerosols on summer precipitation. Again, the magnitude of these changes lies in the range of results obtained with comprehensive models.

On the basis of these experiments we conclude that our reduced-form model has the potential for reliably simulating future changes in relevant climatic variables over India. Before including the model into IAMs, however, the tunable model parameters would have to be subject to a thorough data assimilation procedure similar to that employed for the THC box model. Further, the model would have to be supplemented by an appropriate representation of the radiative effects of sulfate aerosols which is so far very crude.

Besides model validation, the experiments described above allow one to get some indication about possible consequences of climate change for food security, a salient issue in India. Food production is highly variable already under present-day climate conditions, with years of good agricultural performance being associated with abundant precipitation and years of poor agricultural performance and more widespread famine being associated with weak rainfall. The possibility that rising sulfur emissions could lead to a weaker and shorter monsoon, with possible detrimental effects on food supply in India, emphasizes the need for efficient sulfur control policies in South and Southeast Asia.

The vulnerability of Indian rural society also raises the issue of changes in year-to-year monsoon variability. There are indications that the latter could increase in the wake of climate change (Meehl and Washington 1993; Hu et al. 2000) which could seriously challenge the adaptive capacity of people living in the region. Concerning changes in monsoon variability, however, our reduced-form model cannot provide much insight as it does not explicitly represent the large-scale circulation patterns whose changes would be determining.

Given that little is known about the existence of singular points in the dynamics of the Indian monsoon, we devoted large space to the identification of changes in the qualitative system behavior by means of bifurcation analysis. To this scope, we reduced the basic model to an even simpler form (termed 'reduced' model) which could be treated quasi-analytically. For the first time, a bifurcation was identified in the summer monsoon's joint phase and parameter space: it is a saddle-node bifurcation which occurs under summer conditions at critical values of the planetary albedo or insolation. Furthermore, the system was found to exhibit two stable equilibria: besides the wet summer monsoon, a stable state exists which is characterized by a weak hydrological cycle. These findings could be of great concern in the context of climate change (or, more generally, global environmental change) for two reasons: first, the bifurcation point could be located not far from the present-day value. Second, a large cloud of anthropogenic haze is observed to spread over South and Southeast Asia (Lelieveld et al. 2001). The scattering aerosols contained in the haze such as sulfate could

alter the planetary albedo so to force the system across the critical threshold. Analysis with the reduced model suggests that changes in the albedo of the clear-sky and cloudy atmosphere and/or changes in the surface albedo which lie well within the plausible range could lead to a destabilization of the Indian summer monsoon.

The reduced model, however, neglects important feedbacks due to the prescription of cloudiness. We therefore explored the potential for a destabilization of the summer monsoon with the basic model. We found that both cloud and surface albedo have to be increased considerably and precipitation efficiency (which is related to the first indirect aerosol effect) decreased in order to bring the system in the vicinity of the bifurcation point. This is the reason why a destabilization of the Indian summer monsoon is not found in the climate change experiments described above. Given that anthropogenic sulfur emissions will probably not continue to rise indefinitely because of their recognized negative effects on human health, food production and ecosystems, and that the negative radiative forcing of sulfate aerosols will be counteracted by greenhouse warming and the effects of the absorbing aerosols contained in the Asian haze, we conclude that in the light of our results it is unlikely that anthropogenic climate change will force the system across the threshold.

5.3 Emissions corridors preserving the THC

In the last part of this thesis we presented an exemplary integrated assessment application of the reduced-form THC model. Using the conceptual and methodological framework provided by the tolerable windows approach (TWA), we identified the leeway for action for global climate policies committed to the preservation of the THC without endangering future economic growth.

The analytical tool employed consists of the THC box model described in chapter 2 coupled to the reduced-form ICLIPS climate model (ICM; Bruckner et al. 2003). Although the coupled model disregards some feedbacks discussed in the literature, such as the effect of a THC slowdown on the oceanic carbon cycle and heat capacity, the coupled model has proven to reproduce the range of THC responses exhibited by sophisticated climate models. One strength of the coupled ICM/THC model is its flexibility which allows one to investigate the sensitivity of the results to a large number of uncertain factors. In addition to the THC box model and forcing parameters discussed in section 5.1, these include emissions of greenhouse gases and aerosols, and the climate sensitivity parameter.

Results obtained within our modeling framework indicate that for the 'best guess' choice of model parameters, the CO_2 emissions corridor is larger than the range spanned by the SRES emissions scenarios for the 21st century, implying that under these circumstances short-term mitigation efforts are not required to preserve the THC. An extensive sensitivity analysis, however, indicates that this finding is largely dependent upon the specific choice of climate and North Atlantic hydrological sensitivities and assumptions about emissions of non-CO_2 greenhouse gases and aerosols.

Uncertainty in the climate sensitivity $T_{2\times CO_2}$ by a factor of three introduces even greater uncertainty in the allowable CO_2 emissions. As a consequence, for a climate sensitivity of 1.5 °C the corridor is much wider than the range spanned by the SRES emissions scenarios, while for high values (i.e., $T_{2\times CO_2} \geq 3.5$ °C) the A2 marker scenario transgresses the upper corridor boundary. This indicates that if $T_{2\times CO_2}$ turns out to be at the upper end of the IPCC range and emissions during the 21st century will be high, CO_2 emissions will have to be reduced in the second half of this century for the THC to be preserved.

A factor of five uncertainty in the North Atlantic hydrological sensitivity propagates onto a similar uncertainty in the width of the emissions corridor. Similarly to climate sensitivity, this implies a large range in the required CO_2 emissions reduction: from doing nothing in the case of low hydrological sensitivity to notable efforts in the second half of the 21st century in the case of high hydrological sensitivity and high reference CO_2 emissions.

Given that uncertainties in climate and hydrological sensitivity combine to an overall uncertainty range, we performed an aggregated analysis by varying both parameters simultaneously. Assuming 'optimistic' (i.e., low) values of both sensitivities, the resulting emissions corridor is huge: the associated cumulative emissions in the year 2100 of about 14000 GtC widely exceed current estimates of carbon bound in fossil fuel reserves (1500–5000 GtC). In contrast, if we assume high values of both sensitivities, the corridor area becomes very tight (associated cumulative emissions in 2100 amounting to 900 GtC), so that already low non-intervention emissions scenarios such as the SRES B1 scenario transgress the upper corridor boundary in the early decades of this century.

Besides climate and hydrological sensitivity, the width of the corridors is affected by assumptions concerning emissions of non-CO_2 GHGs and aerosols. The influence of these factors, however, is much smaller than that of the climate and hydrological sensitivity parameters.

In addition to the 'prognostic' uncertainties discussed so far, the width of the emissions corridor is affected by the 'normative' uncertainties. These reflect the subjectivity in the judgment of what may be considered unacceptable. Firstly, we assumed a more ambitious THC guardrail by limiting the weakening of the THC to a 10–40% reduction relative to the present-day intensity. We found that the pursuit of a more ambitious THC target tightens the corridors considerably. As a consequence, no open corridor exists if a 10% weakening of the THC is to be avoided, implying that it would not be feasible to attain this target under the predefined socio-economic constraints. For a corridor to exist, these constraints could be relaxed, i.e., the maximum admissible emissions reduction rate r increased and/or the minimum admissible transition time t_{trans} decreased. This illustrates that a trade-off between THC and socio-economic guardrails may be required in the case of very tight emissions corridors. Concerning the sensitivity of emissions corridors to the socio-economically motivated guardrails, we found that the value of r significantly affects the corridor throughout the 21st century whereas the value of t_{trans} influences the corridor mainly in the first decades of this century.

In light of the huge uncertainty associated with the allowable range of CO_2 emissions and the values at stake, a precautionary attitude may seem advisable. This would require to keep global CO_2 emissions within the range spanned by the 'worst case' corridor, i.e., the corridor that arises under the most pessimistic assumptions about all pertinent parameters. The tightness of this corridor in our model emphasizes the necessity to abandon business-as-usual paths within the decades to come if the risk of a THC shutdown is to be kept low.

5.4 Outlook and final remarks

The results presented in this thesis highlight the value of reduced-form modeling. We have demonstrated that besides serving pragmatic purposes, such as efficient emulation of the behavior of complex models, appropriately designed reduced-form models allow one to gain new physical insights. Because of their transparency, they enable the exploration of physical mechanisms without the need for complex model diagnostics. This renders these models

valuable tools for the testing of hypothesis and for tutorial purposes. Because of their relative algebraic simplicity, reduced-form models provide the opportunity to apply analytical methods in order to, for example, systematically explore the structure of the system's joint phase and parameter space and reveal the position of bifurcation points. In this, they provide guidance for future research using comprehensive models. Concerning the monsoon threshold identified in this thesis, for instance, the information gained about its position relative to the present-day state could be exploited for the design of climate change test scenarios. The latter could be employed to drive appropriate EMICs (i.e., resolving the Indian monsoon and representing the effects of aerosols) in order to investigate whether the potential for monsoon destabilization persists in such models. Climbing the complexity scale, insights gained with EMICs can subsequently be used for the design of targeted GCM experiments.

Application of reduced-form climate models exhibiting singular behavior in the context of integrated assessment provides indications about where research efforts may be directed in order to reduce uncertainty about the required GHG mitigation measures. The results of our extensive sensitivity analysis of emissions corridors preserving the THC indicate that the uncertainty in the allowable CO_2 emissions would be reduced most if the uncertainty ranges for climate and hydrological sensitivity could be narrowed. This could perhaps be achieved by a well-designed program of climate model evaluation and improvement and targeted observational programs addressing, e.g., non-CO_2 sources of radiative forcing, ocean heat storage, top-of-the atmosphere radiative fluxes, river and meltwater runoff changes.

Another factor largely contributing to the uncertainty in the admissible CO_2 emissions ranges is the uncertainty about the amount of weakening of the THC which would constitute a serious threat. This highlights the need for enhanced research efforts about the consequences of THC changes. Concerning the impacts on north-western Europe, first studies are now being conducted (INTEGRATION 2001), but concerning other regions potentially affected by THC changes (cf. e.g. Vellinga and Wood 2002) similar research projects have not been initiated yet.

We conclude by drawing some lessons concerning Article 2 of the UNFCCC. In the first place, the findings presented in this thesis challenge the view that large-scale singularities are not a near-term concern for climate policy. In fact, considering the large uncertainties associated with physical parameters, emissions of non-CO_2 GHGs and aerosols and the inertia of the energy-economy system, business-as-usual risks foreclosing the option of preventing a shutdown of the THC already in the first decades of this century. Secondly, avoiding 'dangerous' climate change may require trade-offs between environmentally and socio-economically motivated targets. We have shown, for instance, that it would not be feasible to limit the amount of weakening of the THC to some ten percent under strong restrictions on the costs of GHG mitigation. Trade-off between different environmental targets may also be necessary as illustrated by the THC and monsoon examples: avoiding unacceptable changes in the Indian monsoon may require strong reductions in sulfur dioxide emissions. On the other hand, sulfur mitigation would remove the aerosol mask and speed up global warming potentially foreclosing the option of preventing dangerous changes in the THC.

The latter constitutes a typical dilemma of an integrated management under global environmental change. A way out could be identified through the exploration of a large number of alternative strategies by means of appropriately designed integrated assessment models.

Appendix A

Reduced-form model of the THC including vertical and horizontal mixing

In the following, we give the equations for the version of the four-box model including vertical and horizontal mixing. For the representation of convection and vertical diffusion we subdivide the northern box into an upper and a lower part (the lower part being termed 'box 5') and introduce vertical diffusive fluxes between these boxes, and between box 3 and 4. Horizontal mixing is represented through the implementation of diffusive fluxes between adjacent boxes (i.e., between the surface boxes 1 and 3, and 3 and 2, and the deep boxes 1 and 4, and 4 and 5). Note that the diffusive fluxes are bidirectional, in order to allow for the exchange of heat and salt, but not of mass. This results in the following set of differential equations for the temperatures and salinities of the boxes:

$$\dot{T}_1 = \frac{m+D_h}{V_1}(T_4-T_1)+\frac{D_h}{V_1}(T_3-T_1)+\lambda_1(T_1^*-T_1) \tag{A.1}$$

$$\dot{T}_2 = \frac{m+D_h}{V_2}(T_3-T_2)+\frac{D_v^2}{V_2}(T_5-T_2)+\lambda_2(T_2^*-T_2) \tag{A.2}$$

$$\dot{T}_3 = \frac{m+D_h}{V_3}(T_1-T_3)+\frac{D_h}{V_3}(T_2-T_3)+\frac{D_v^3}{V_3}(T_4-T_3)+\lambda_3(T_3^*-T_3) \tag{A.3}$$

$$\dot{T}_4 = \frac{m+D_h}{V_4}(T_5-T_4)+\frac{D_h}{V_4}(T_1-T_4)+\frac{D_v^3}{V_4}(T_3-T_4) \tag{A.4}$$

$$\dot{T}_5 = \frac{m+D_v^2}{V_5}(T_2-T_5)+\frac{D_h}{V_5}(T_4-T_5) \tag{A.5}$$

$$\dot{S}_1 = \frac{m+D_h}{V_1}(S_4-S_1)+\frac{D_h}{V_1}(S_3-S_1)+\frac{S_0F_1}{V_1} \tag{A.6}$$

$$\dot{S}_2 = \frac{m+D_h}{V_2}(S_3-S_2)+\frac{D_v^2}{V_2}(S_5-S_2)-\frac{S_0F_2}{V_2} \tag{A.7}$$

$$\dot{S}_3 = \frac{m+D_h}{V_3}(S_1-S_3)+\frac{D_h}{V_3}(S_2-S_3)+\frac{D_v^3}{V_3}(S_4-S_3)-\frac{S_0(F_1-F_2)}{V_3} \tag{A.8}$$

$$\dot{S}_4 = \frac{m + D_h}{V_4}(S_5 - S_4) + \frac{D_h}{V_4}(S_1 - S_4) + \frac{D_v^3}{V_4}(S_3 - S_4) \tag{A.9}$$

$$\dot{S}_5 = \frac{m + D_v^2}{V_5}(S_2 - S_5) + \frac{D_h}{V_5}(S_4 - S_5)\,. \tag{A.10}$$

Here, D_v^2, D_v^3 denote the vertical diffusive fluxes between the northern and the low-latitude boxes, respectively, and D_h^s the horizontal diffusive flux.

Since the northern box is split in two parts, the pressure at its bottom results from the volume-averaged densities of box 2 and 5. Eq. (2.1) is therefore rewritten as:

$$\rho_0\, m = k\left(\frac{\rho_2\, V_2 + \rho_5\, V_5}{V_2 + V_5} - \rho_1\right). \tag{A.11}$$

Note that in the limit of very large vertical mixing in the northern box (i.e., $\rho_5 \approx \rho_2$), Eqs. (2.1) and (A.11) are identical.

For the derivation of the fluxes D_v^i and D_h from the diffusion coefficients in the units they are usually expressed in (i.e., m^2/s), we need to specify a lenght. For D_v^i, i$\in \{2,3\}$, this is taken to be the relation between box area A_i and average thickness $\bar{z}$:

$$D_v^2 = \frac{A_2}{\bar{z}}\, K_v^2 \tag{A.12}$$

$$D_v^3 = \frac{A_3}{\bar{z}}\, K_v^3, \tag{A.13}$$

where K_v^2 and K_v^3 are the vertical diffusion coefficients for the northern and low-latitude boxes, respectively. For K_v^2 we use a value of $10^{-4}\,\mathrm{m}^2\,\mathrm{s}^{-1}$ resp. $10^{-2}\,\mathrm{m}^2\,\mathrm{s}^{-1}$ for the convecting and non-convecting case, and for K_v^3 a value of $10^{-4}\,\mathrm{m}^2\,\mathrm{s}^{-1}$.

For the calculation of the horizontal diffusive flux D_h, we use the relation between the area $B = \bar{x}\,\bar{z}$, where $\bar{x}$ is the average zonal box extent, and the average meridional box extent $\bar{y}$:

$$D_h = \frac{B}{\bar{y}}\, K_h, \tag{A.14}$$

where K_h is the horizontal diffusion coefficient. For K_h, $\bar{x}$, $\bar{y}$, $\bar{z}$ we use values of $10^{-1}\,\mathrm{m}^2\,\mathrm{s}^{-1}$, $6{\cdot}10^6$ m, $5{\cdot}10^6$ m and $1.5{\cdot}10^3$ m, respectively.

Note that for the investigation of the effects of the individual physical processes, as attempted in section 2.6, we applied the following model settings:

- Northern vertical mixing: $K_v^3 = K_h = 0$.
- Mid-latitude vertical mixing: 4 boxes (i.e., $V_5 \to 0$, $V_4 \to V_4 + V_5$), K_h=0.
- Horizontal mixing: 4 boxes, K_v^3=0.

Appendix B

Steady-state solutions and coefficients of the reduced monsoon model

B.0.1 Steady state solutions of the reduced model

By equating the right hand sides of Eqs. (3.65), (3.64) with zero we derive the following expressions for w_2 and q_a:

$$w_2 = w_1, \tag{B.1}$$

$$q_a = \frac{-(A_2+B_2)w_1 + E_2 T_a w_1}{C_2 - D_2 w_1 + F_2 T_a w_1}. \tag{B.2}$$

Eq. (3.66) together with the above formulas yields a quadratic polynomial in w_1 and T_a, which we solve for w_1:

$$w_1^{(+,-)} = \frac{-(a_4 T_a^2 + a_5 T_a + a_6) \pm \sqrt{(a_4 T_a^2 + a_5 T_a + a_6)^2 - 4(a_1 T_a^2 + a_2 T_a + a_3)(a_7 T_a + a_8)}}{2\,(a_1 T_a^2 + a_2 T_a + a_3)}, \tag{B.3}$$

whereby the coefficients a_i are defined as follows:

$$\begin{aligned}
a_1 &= F_2 E_3 - E_2 G_3, \\
a_2 &= -F_2 A_3 + E_2 D_3 - D_2 E_3 + G_3(A_2+B_2), \\
a_3 &= D_2 A_3 - D_3(A_2+B_2), \\
a_4 &= F_2 C_3 - E_2 F_3, \\
a_5 &= E_2 B_3 - D_2 C_3 + C_2 E_3 + F_3(A_2+B_2) - F_2 H_3, \\
a_6 &= -C_2 A_3 - B_3(A_2+B_2) + D_2 H_3, \\
a_7 &= C_2 C_3, \\
a_8 &= -C_2 H_3.
\end{aligned}$$

The so-derived expressions for w_2, w_1 and q_a can than be substituted into Eq. (3.67), yielding two 8^{th} order polynomials in T_a (one for each solution of w_1):

$$f_+(T_a) = A_4 q_a + B_4 w_1^+ + C_4 T_a - D_4 T_a q_a^2 + E_4 q_a^2 + F_4 T_a w_1^+ q_a - G_4 T_a w_1^+$$

$$
\begin{aligned}
& -H_4 w_1^+ q_a + I_4 T_a^2 + J_4 T_a^2 q_a^2 + K_4, && \text{(B.4)}\\
f_-(T_a) \;=\; & A_4 q_a + B_4 w_1^- + C_4 T_a - D_4 T_a q_a^2 + E_4 q_a^2 + F_4 T_a w_1^- q_a - G_4 T_a w_1^- \\
& -H_4 w_1^- q_a + I_4 T_a^2 + J_4 T_a^2 q_a^2 + K_4. && \text{(B.5)}
\end{aligned}
$$

B.0.2 Coefficients of the reduced model

In the following tables, we give the coefficients of the reduced monsoon model.

Coefficients C_i^j	
$C_m = \frac{\sin(\alpha_0)\, g\, p_0\, H_t}{\rho_0\, f\, 2\, R\, T_0^2\, \Delta L}$	$H'_e = \frac{H_0\, H_e}{H_0 + H_e}$
$C_E^1 = (1-F)\rho_0\, C_D\, C_m - F\,\rho_0\, C_D\, C_m$	$C_E^2 = C_E^1\, q_{sat}(T_s)$
$C_E^3 = C_E^1\, T_{oc}$	$C_E^4 = C_E^1\, q_{sat}(T_s)\, T_{oc}$
$C_P = \frac{N\,\rho_0\, H'_e}{\tau_0}$	$C_R = C_P\, K_r$
$fact_1 = \exp\left(-\frac{h}{H'_e}\right)\left(1 - \exp\left(\frac{h}{H_0}\right)\right)$	
$C_{A_v}^1 = -\frac{4\Delta L}{S}\, C_m\, \rho_0\, q_{sat}(T_{oc})\, f_{oc}\, H'_e\, \left((1-F)\, \left(\exp\left(-\frac{h}{H'_e}\right) - 1\right) - F\, fact_1\right)$	
$C_{A_v}^2 = -\frac{4\Delta L}{S}\, C_m\, \rho_0\, H'_e\, \left((1-F)\, fact_1 - F\, \left(\exp\left(-\frac{h}{H'_e}\right) - 1\right)\right)$	
$C_S = I_0\, \cos\xi\, (1 - A_{sys})$	
$C_{LW}^1 = A_0 - B_0\, T_0 - C_0\, N + D_0\, N\, T_0$	$C_{LW}^2 = B_0 - D_0\, N$
$z_{eff}^1 = H_0 + \frac{h\, \exp\ -\frac{h}{H_0}}{\exp\ -\frac{h}{H_0}\ -1}$	$z_{eff}^2 = H_0 + \frac{H_t\, \exp\ -\frac{H_t}{H_0}\ -h\, \exp\ -\frac{h}{H_0}}{\exp\ -\frac{H_t}{H_0}\ -\exp\ -\frac{h}{H_0}}$
$C_{A_T}^0 = \frac{4\Delta L}{S}\, C_m\, \rho_0\, c_p\, H_0\, \left(1 - \exp\left(-\frac{h}{H_0}\right)\right)$	
$C_{A_T}^1 = -C_{A_T}^0\, \left((1-F)\, \left(T_{oc} - (\Gamma(T_{oc}) - \Gamma_a)\, z_{eff}^1\right) - F\, \left(T_{oc} - (\Gamma(T_{oc}) - \Gamma_a)\, z_{eff}^2\right)\right)$	
$C_{A_T}^2 = C_{A_T}^0\, (1 - 2\,F)$	$C_{A_T}^3 = C_{A_T}^0\, \left((1-F)\, z_{eff}^2 - F\, z_{eff}^1\right)$

Table B.1: Coefficients C_i^j of Eqs. (3.57)–(3.63). Note that the factor F was introduced to guarantee the validity of the coefficients for both summer (i.e., $T_a > T_{oc}$) and winter ($T_a < T_{oc}$) conditions. F takes the value 0 in summer and 1 in winter.

Coefficients	
$A_1 = f_1/(f_2\,\tau)$	
$A_2 = 1/\tau$	$B_2 = C_E^4/f_1 - 1/\tau$
$C_2 = C_P/f_1$	$D_2 = (C_E^3 + C_R)/f_1$
$E_2 = C_E^2/f_1$	$F_2 = C_E^1/f_1$
$I_q = H_e'\,\rho_0$	
$A_3 = C_E^4/I_q$	$B_3 = (-C_P + C_{A_v}^2\,T_{oc})/I_q$
$C_3 = C_{A_v}^1/I_q$	$D_3 = C_E^3 I_q$
$E_3 = C_E^2/I_q$	$F_3 = C_{Av}^2/I_q$
$G_3 = C_E^1/I_q$	$H_3 = C_{Av}^1\,T_{oc}/I_q$
$I_T = \rho_0\,c_p\,H_0\,\exp\left(\frac{H_a}{H_0} + 1\right)$	
$A_4 = \mathcal{L}\,C_P/I_T$	$B_4 = C_E^4/I_T$
$C_4 = (-C_{LW}^2 + C_{A_T}^1 - C_{A_T}^2\,T_{oc} - C_{A_T}^3\,(\Gamma_0 - \Gamma_1\,T_0 - \Gamma_2\,N - \Gamma_a - \Gamma_1\,T_{oc}))/I_T$	
$D_4 = C_{A_T}^3\Gamma_1\,a_q\,(T_0 + T_{oc})\,/I_T$	
$E_4 = C_{A_T}^3\,\Gamma_1\,a_q\,T_0\,T_{oc}/I_T$	$F_4 = \mathcal{L}\,C_E^1/I_T$
$G_4 = \mathcal{L}\,C_E^2/I_T$	$H_4 = \mathcal{L}\,C_E^3/I_T$
$I_4 = (C_{A_T}^2 - C_{A_T}^3\,\Gamma_1)/I_T$	$J_4 = C_{A_T}^3\,\Gamma_1\,a_q/I_T$
$K_4 = (C_S - C_{LW}^1 - C_{A_T}^1\,T_{oc} + C_{A_T}^3\,T_{oc}\,(\Gamma_0 - \Gamma_1\,T_0 - \Gamma_2\,N - \Gamma_a))/I_T$	

Table B.2: Coefficients of Eqs. (3.65)–(3.67).

References

Alcamo, J. and E. Kreileman (1996). Emission scenarios and global climate protection. *Global Environmental Change 6*, 305–334.

Altabet, M., M. Higginson, and D. Murray (2002). The effect of millennial-scale changes in Arabian Sea denitrification on atmospheric CO_2. *Nature 415*, 159–162.

Andronova, N. and M. Schlesinger (2001). Objective estimation of the probability density function for climate sensitivity. *J. Geophys. Res. 106*(D19), 22,605–22,611.

Argyris, J., G. Faust, and M. Haase (1995). *Die Erforschung des Chaos*. Wiesbaden: Vieweg.

Aubin, J. (1991). *Viability theory*. Basel: Birkhäuser.

Berger, A. (1978). Long-term variations of daily insolation and Quaternary climatic changes. *J. Atmos. Sci. 35*, 2362–2367.

Bhaskaran, B. and J. Mitchell (1998). Simulated changes in Southeast Asian monsoon precipitation resulting from anthropogenic emissions. *Int. J. Climatol. 18*, 1455–1462.

Boucher, O., M. Pham, and R. Sadourny (1998). General circulation model simulations of the Indian summer monsoon with increasing levels of sulphate aerosols. *Ann. Geophys. 16*, 346–352.

Brooke, A., D. Kendrick, and A. Meeraus (1992). *GAMS: a user's guide. Release 2.25*. Scientific Press.

Brovkin, V., M. Claussen, V. Petoukhov, and A. Ganopolski (1998). On the stability of the atmosphere-vegetation system in the Sahara/Sahel region. *J. Geophys. Res. 103*(D24), 31,613–31,624.

Bruckner, T., G. Hooss, H. Füssel, and K. Hasselmann (2003). Climate system modeling in the framework of the tolerable windows approach: the ICLIPS climate model. *Climatic Change 56*, 119–137.

Bruckner, T., G. Petschel-Held, F. Tóth, H. Füssel, C. Helm, M. Leimbach, and H. Schellnhuber (1999). Climate change decision support and the tolerable windows approach. *Env. Mod. Ass. 4*, 217–234.

Budyko, M. (1982). *The Earth's climate*, Volume 29 of *International Geophysics Series*. New York: Academic Press.

Chandrasekar, A. and A. Kitoh (1998). Impact of localized sea surface temperature anomalies over the equatorial Indian Ocean on the Indian summer monsoon. *J. Meteorol. Soc. Jap. 76*(6), 841–853.

Chou, C., J. Neelin, and H. Su (2000). Ocean-atmosphere-land feedbacks. *Q. J. R. Meteorol. Soc. 126*, 1–29.

Claussen, M. (1991). Estimation of areally-averaged surface fluxes. *Boundary Layer Meteorol. 54*, 387–410.

Claussen, M. (1997). Modelling bio-geophysical feedback in the African and Indian monsoon region. *Climate Dynamics 13*, 247–257.

Dansgaard, W., S. Johnsen, H. Clausen, N. Dahl-Jensen, N. Gundestrup, C. Hammer, C. Hvidberg, J. Steffensen, A. Sveinbjoernsdottir, J. Jouzel, and G. Bond (1993). Evidence for general instability of past climate from a 250-kyr ice-core record. *Nature 364*, 218–220.

Deimling, K. (1992). *Multivalued differential equations*. Berlin, Germany: De Gruyter.

Dickinson, R., A. Henderson-Sellers, P. Kennedy, and M. Wilson (1986). Biosphere-atmosphere transfer scheme (bats) for the NCAR community climate model. Technical report, National Center for Atmospheric Research, Boulder, US.

Dixon, K., T. Delworth, M. Spelman, and R. Stouffer (1999). The influence of transient surface fluxes on North Atlantic overturning in a coupled GCM climate change experiment. *Geophys. Res. Let. 26*(17), 2749–2752.

Doedel, E. J. (1981). Auto: A program for the automatic bifurcation analysis of autonomous systems. In *Proc. 10th Manitoba Conf. on Num. Math. and Comp., Univ. of Manitoba, Winnipeg, Canada*, pp. 265–284.

Douville, B., J.-F. Royer, J. Polcher, P. Cox, N. Gedney, D. Stephenson, and P. Valdes (2000). Impacts of CO_2 doubling on the Asian summer monsoon: robust versus model-dependent responses. *J. Meteorol. Soc. Jap. 78*(4), 421–439.

Edmonds, J. and M. Wise (1998). The value of advanced energy technologies in stabilizing atmospheric CO_2. In F. Tóth (Ed.), *Cost-Benefit Analyses of Climate Change*, pp. 87–104. Basel: Birkhäuser.

Fleitmann, D., S. Burns, M. Mudelsee, U. Neff, J. Kramers, A. Mangini, and A. Matter (2003). Holocene forcing of the Indian monsoon recorded in a stalagmite from southern Oman. *Science 300*, 1737–1739.

Forest, C., P. Stone, A. Sokolov, M. Allen, and M. Webster (2002). Quantifying uncertainties in climate system properties with the use of recent climate observations. *Science 295*, 113–117.

Ganachaud, A. and C. Wunsch (2000). Improved estimates of global ocean circulation, heat transport and mixing from hydrographic data. *Nature 408*, 453–457.

Ganopolski, A., V. Petoukhov, S. Rahmstorf, V. Brovkin, M. Claussen, A. Eliseev, and C. Kubatzki (2001). CLIMBER-2: a climate system model of intermediate complexity. Part II: model sensitivity. *Climate Dynamics 17*, 735–751.

Gargett, A. and B. Ferron (1996). The effect of differential vertical diffusion of T and S in a box model of thermohaline circulation. *J. Marine Res. 54*, 827–866.

Gildor, H. and E. Tziperman (2001). A sea ice climate switch mechanism for the 100-kyr glacial cycles. *J. Geophys. Res. 105*(C5), 9117–9133.

Griffies, M. and E. Tziperman (1995). A linear thermohaline oscillator driven by stochastic atmospheric forcing. *J. Climate 8*, 2440–2453.

Gupta, A., D. Anderson, and J. Overpeck (2003). Abrupt changes in the Asian southwest monsoon during the Holocene and their links to the North Atlantic Ocean. *Nature 421*, 354–357.

Hahn, D. and S. Manabe (1975). The role of mountains in the South Asian monsoon circulation. *J. Atmos. Sci. 32*, 1515–1541.

Haney, R. (1971). Surface thermal boundary condition for ocean circulation models. *J. Phys. Oceanogr. 1*, 241–248.

Hansen, J., G. Russell, D. Rind, P. Stone, A. Lacis, S. Lebedeff, R. Ruedy, and L. Travis (1983). Efficient three-dimensional global models for climate studies: Models I and II. *Monthly Weather Review 11*(4), 609–662.

Haywood, J. (1997). Transient response of a coupled model to estimated changes in greenhouse gas and sulfate concentrations. *Geophys. Res. Let. 24*(11), 1335–1338.

Heinrich, H. (1988). Origin and consequences of cyclic ice rafting in the northeast atlantic ocean during the past 130,000 years. *Quat. Res. 29*, 143.

Hooss, G., R. Voss, K. Hasselmann, E. Maier-Reimer, and F. Joos (1999). *A nonlinear impulse response model of the coupled carbon cycle – ocean – atmosphere climate system*. Number 290 in Max-Planck Institut für Meteorologie Report Series. Hamburg.

Hooss, G., R. Voss, K. Hasselmann, E. Maier-Reimer, and F. Joos (2001). A nonlinear impulse response model of the coupled carbon cycle – climate system (NICCS). *Climate Dynamics 18*, 189–202.

Houghton, J., B. Callander, and S. Varney (Eds.) (1992). *Climate Change 1992: The Supplementary Report to the IPCC Scientific Assessment*. Cambridge: Cambridge University Press.

Houghton, J., Y. Ding, D. Griggs, M. Noguer, P. van der Linden, X. Dai, K. Maskell, and C. Johnson (Eds.) (2001). *Climate Change 2001: The scientific basis – Contribution of Working Group I to the Third Assessment Report of the IPCC*. Cambridge: Cambridge University Press.

Houghton, J., L. M. Filho, B. Callander, N. Harris, A. Kattenberg, and K. Maskell (Eds.) (1995). *Climate Change 1995: The science of climate change – Contribution of Working Group I to the Second Assessment Report of the IPCC*. Cambridge: Cambridge University Press.

Hu, Z.-Z., M. Latif, E. Roeckner, and L. Bengtsson (2000). Intensified Asian summer monsoon and its variability in a coupled model forced by increasing greenhouse gas concentrations. *Geophys. Res. Let. 27*(17), 2681–2684.

Huang, R., J. Luyten, and H. Stommel (1992). Multiple equilibrium states in combined thermal and saline circulation. *J. Phys. Oceanogr. 22*, 231–246.

Hughes, T. and A. Weaver (1996). Sea surface temperature-evaporation feedback and the ocean's thermohaline circulation. *J. Phys. Oceanogr. 26*, 644–654.

INTEGRATION (2001). Integrated assessment of changes in the thermohaline circulation. http://www.pik-potsdam.de/∼stefan/Projects/integration/index.html.

Johannessen, O. M., E. V. Shalina, and M. W. Miles (1999). Satellite evidence for an Arctic sea ice cover in transformation. *Science 286*, 1937–1939.

Ju, J. and J. Slingo (1995). The Asian summer monsoon and ENSO. *Q. J. R. Meteorol. Soc. 122*, 1133–1168.

Keller, K., K. Tan, F. Morel, and D. Bradford (2000). Preserving the ocean circulation: implications for climate policy. *Climatic Change 47*, 17–43.

Kitoh, A., S. Yukimoto, A. Noda, and T. Motoi (1997). Simulated changes of the Asian summer monsoon at times of increased CO_2. *J. Meteorol. Soc. Jap. 75*(6), 1019–1031.

Knutti, R., T. Stocker, F. Joos, and G.-K. Plattner (2002). Constraints on radiative forcing and future climate change from observations and climate model ensembles. *Nature 416*, 719–723.

Knutti, R., T. Stocker, and D. Wright (2000). The effects of subgrid-scale parameterizations in a zonally-averaged ocean model. *J. Phys. Oceanogr. 30*, 2738–2752.

Kriegler, E. (2001). Temperature equation of the ICLIPS climate model and its relation to a physical two-box model. Unpublished manuscript.

Kriegler, E. and T. Bruckner (2004). Sensitivity analysis of emissions corridors for the 21$^{\text{st}}$ century. *Climatic Change*. Accepted.

Lal, M., U. Cubasch, R. Voss, and J. Waszkewitz (1995). Effect of transient increase in greenhouse gases and sulphate aerosols on monsoon climate. *Current Science 69*(9), 752–763.

Lal, M., T. Nozawa, S. Emori, H. Harasawa, K. Takahashi, M. Kimoto, A. Abe-Ouchi, T. Nakajima, T. Takemura, and A. Numaguti (2003). Future climate change: Implications for Indian summer monsoon and its variability. *Current Science 81*(9), 1196–1207.

Latif, M., E. Röckner, U. Mikolajewicz, and R. Voss (2000). Tropical stabilization of the thermohaline circulation in a greenhouse warming simulation. *J. Climate 13*, 1809–1813.

Ledwell, J., A. Watson, and C. Law (1998). Mixing of a tracer in the pycnocline. *J. Geophys. Res. 103*(C10), 21,499–21,529.

Leimbach, M. and T. Bruckner (2001). Influence of economic constraints on the shape of emission corridors. *Computational Economics 18*, 173–191.

Lelieveld, J., P. Crutzen, V. Ramanathan, M. Andreae, C. Brenninkmeijer, T. Campos, G. Cass, R. Dickerson, H. Fischer, J. de Gouw, A. Hansel, A. Jefferson, D. Kley, A. de Laat, S. Lal, M. Lawrence, J. Lobert, O. Mayol-Bracero, A. Mitra, T. Novakov, S. Oltmans, K. Prather, T. Reiner, H. Rodhe, H. Scheeren, D. Sikka, and J. Williams (2001). The Indian Ocean experiment: widespread air pollution from South and Southeast Asia. *Science 291*, 1031–1036.

Li, T., Y. Zhang, C.-P. Chang, and B. Wang (2001). On the relationship between Indian Ocean sea surface temperature and Asian monsoon. *Geophys. Res. Let. 28*(14), 2843–2846.

Liou, K.-N. (1980). *An introduction to atmospheric radiation*. New York: Academic Press.

Lorenz, E. (1963). Deterministic nonperiodic flow. *J. Atmos. Sci. 20*, 130–141.

Maier-Reimer, E. and K. Hasselmann (1987). Transport and storage of CO_2 in the ocean – an inorganic ocean-circulation carbon cycle model. *Climate Dynamics 2*, 63–90.

Manabe, S. and R. Stouffer (1988). Two stable equilibria of a coupled ocean-atmosphere model. *J. Climate 1*, 841–866.

Manabe, S. and R. Stouffer (1993). Century-scale effects of increased atmospheric CO_2 on the ocean-atmosphere system. *Nature 364*, 215–218.

Manabe, S. and R. Stouffer (1994). Multiple-century response of a coupled ocean-atmosphere model to an increase of atmospheric carbon dioxide. *J. Climate 7*, 5–23.

Manabe, S. and R. Stouffer (1999). The role of thermohaline circulation in climate. *Tellus 51 A-B*, 91–109.

Mastrandrea, M. and S. Schneider (2001). Integrated assessment of abrupt climatic changes. *Climate Policy 1*, 433–449.

May, W. (2002). Simulated changes of the Indian summer monsoon under enhanced greenhouse gas conditions. *Geophys. Res. Let. 29*(7), 10.1029/2001GL013808.

McCarthy, J., O. Canziani, N. Leary, D. Dokken, and K. White (Eds.) (2001). *Climate Change 2001: Impacts, Adaptation and Vulnerability- Contribution of Working Group II to the Third Assessment Report of the IPCC*. Cambridge: Cambridge University Press.

Meehl, G. (1994). Influence of the land surface in the Asian summer monsoon: External conditions versus internal feedbacks. *J. Climate 7*, 1033–1049.

Meehl, G. and W. Washington (1993). South Asian Monsoon variability in a model with doubled atmospheric carbon dioxide concentration. *Science 260*, 1101–1104.

Meehl, G., W. Washington, D. Erickson III, B. Briegleb, and P. Jaumann (1996). Climate change from increased CO_2 and direct and indirect effects of sulfate aerosols. *Geophys. Res. Let. 23*(25), 3755–3758.

Metz, B., O. Davidson, R. Swart, and J. Pan (Eds.) (2001). *Climate Change 2001: Mitigation – Contribution of Working Group III to the Third Assessment Report of the IPCC*. Cambridge: Cambridge University Press.

Mikolajewicz, U. and R. Voss (2000). The role of the individual air-sea flux components in CO_2-induced changes of the ocean's circulation and climate. *Climate Dynamics 16*, 627–642.

Mitchell, J., T. Johns, M. Eagles, W. Ingram, and R. Davis (1999). Towards the construction of climate change scenarios. *Climatic Change 41*, 547–581.

Mitchell, J., T. Johns, J. Gregory, and S. Tett (1995). Climate response to increasing levels of greenhouse gases and sulfate aerosols. *Nature 376*, 501–504.

Morrill, C., J. Overpeck, and J. Cole (2003). A synthesis of abrupt changes in the Asian summer monsoon since the last deglaciation. *The Holocene 13*(4), 465–476.

Mudur, G. (1995). Monsoon shrinks with aerosol model. *Science 270*, 1922.

Nakićenović, N. and R. Swart (2000). *Emissions scenarios*. Cambridge: Cambridge University Press.

Neelin, J. and N. Zeng (2000). A quasi-equilibrium tropical circulation model. *J. Atmos. Sci. 57*, 1741–1766.

Nordhaus, W. (1994). *Managing the global commons: the economics of climate change*. Cambridge, MA: MIT Press.

Palmer, T. (1994). Chaos and predictability in predicting the monsoons. *Proc. Indian Natn. Sci. Acad. 60A*(1), 57–66.

Papageorgiou, M. (1991). *Optimierung*. München: Oldenbourg.

Parmesan, C. and G. Yohe (2003). A globally coherent fingerprint of climate change impacts across natural systems. *Nature 421*, 37–42.

Parthasarathy, B., A. Munot, and D. Kothawale (1994). All-India monthly and seasonal rainfall series: 1871-1993. *Theor. Appl. Climatol. 49*, 217–224.

Peixoto, J. and A. Oort (1992). *Physics of Climate*. New York, US: Springer.

Peterson, B., R. Holmes, J. McClelland, C. Vörösmarty, R. Lammers, A. Shiklomanov, I. Shiklomanov, and S. Rahmstorf (2002). Increasing river discharge to the Arctic Ocean. *Science 298*, 2171–2172.

Petoukhov, V., A. Ganopolski, V. Brovkin, M. Claussen, A. Eliseev, C. Kubatzki, and S. Rahmstorf (2000). CLIMBER-2: a climate system model of intermediate complexity. Part I: model description and performance for present climate. *Climate Dynamics 16*, 1–17.

Petoukhov, V., A. Ganopolski, and M. Claussen (2003). POTSDAM - a set of atmosphere statistical-dynamical models: theoretical background. Technical Report 81, Potsdam Institute for Climate Impact Research, Potsdam.

Petschel-Held, G., H.-J. Schellnhuber, T. Bruckner, F. Tóth, and K. Hasselmann (1999). The tolerable windows approach: theoretical and methodological foundations. *Climatic Change 41*, 303–331.

Prange, M., G. Lohmann, and A. Paul (2003). Influence of vertical mixing on the thermohaline hysteresis: Analyses of an OGCM. *J. Phys. Oceanogr. 33*(8), 1707–1721.

Rahmstorf, S. (1995). Bifurcations of the Atlantic thermohaline circulation in response to changes in the hydrological cycle. *Nature 378*, 145–149.

Rahmstorf, S. (1996). On the freshwater forcing and transport of the Atlantic thermohaline circulation. *Climate Dynamics 12*, 799–811.

Rahmstorf, S. (1999). Rapid transitions of the thermohaline ocean circulation. In F. Abrantes and A. Mix (Eds.), *Reconstructing Ocean History: A Window into the Future*. New York: Kluwer.

Rahmstorf, S. (2000). The thermohaline ocean circulation – a system with dangerous thresholds? *Climatic Change 46*, 247–256.

Rahmstorf, S. (2003). The current climate. *Nature 421*, 699.

Rahmstorf, S. and M. England (1997). Influence of southern hemisphere winds on North Atlantic deep water flow. *J. Phys. Oceanogr. 27*, 2040–2054.

Rahmstorf, S. and A. Ganopolski (1999a). Long-term global warming scenarios computed with an efficient coupled climate model. *Climatic Change 43*, 353–367.

Rahmstorf, S. and A. Ganopolski (1999b). Simple theoretical model may explain apparent climate instability. *J. Climate 12*, 1349–1352.

Rahmstorf, S., T. Kuhlbrodt, K. Zickfeld, G. Bürger, F. Badeck, M. Hofmann, S. Pohl, S. Sitch, H. Held, T. Schneider von Deimling, D. Wolf-Gladrow, M. Schartau, C. Sprengel, S. Sundby, B. Ådlansvik, F. Vikebø, R. Tol, and M. Link (2003). Integrated assessment of changes in the thermohaline circulation - INTEGRATION. In *Proceedings of the DEKLIM status seminar, 6–8 October 2003, Bad Münstereifel, Germany*.

Rahmstorf, S. and J. Willebrand (1995). The role of temperature feedback in stabilizing the thermohaline circulation. *J. Phys. Oceanogr. 25*, 787–805.

Ramanathan, V., P. Crutzen, J. Lelieveld, A. Mitra, D. Althausen, J. Anderson, M. Andreae, W. Cantrell, G. Cass, C. Chung, A. Clarke, J. Coakley, W. Collins, W. Conant, F. Dulac, J. Heintzenberg, A. Heymsfield, B. Holben, S. Howell, J. Hudson, A. Jayaraman, J. Kiehl, T. Krishnamurti, D. Lubin, G. McFarquhar, T. Novakov, J. Ogren, I. Podgorny, K. Prather, K. Priestley, J. Prospero, P. Quinn, K. Rajeev, P. Rasch, S. Rupert, R. Sadourny, S. Satheesh, G. Shaw, P. Sheridan, and F. Valero (2001). Indian Ocean Experiment: An integrated analysis of the climate forcing and effects of the great Indo-Asian haze. *J. Geophys. Res. 106*(D22), 28,371–28,398.

Raper, S., J. Gregory, and R. Stouffer (2002). The role of climate sensitivity and ocean heat uptake on AOGCM transient temperature response. *J. Climate 15*, 124–130.

Raper, S., T. Wigley, and R. Warrick (1996). Global sea level rise: Past and future. In J. Millman and B. Haq (Eds.), *Sea-level rise and coastal subsidence: Causes, consequences and strategies*, pp. 11–45. Dordrecht, The Netherlands: Kluwer Academic Publishers.

Roeckner, E., L. Bengtsson, J. Fechter, J. Lelieveld, and H. Rodhe (1999). Transient climate change simulations with a coupled Atmosphere–Ocean GCM including the tropospheric sulfur cycle. *J. Climate 12*, 3004–3032.

Root, T., J. Price, K. Hall, S. Schneider, C. Rosenzweig, and J. Pounds (2003). Fingerprints of global warming on wild animals and plants. *Nature 421*, 57–60.

Rosenfeld, D. (2000). Suppression of rain and snow by urban and industrial air pollution. *Science 287*, 1793–1796.

Sankar-Rao, M., L. Lau, and S. Yang (1996). On the relationship between Eurasian snow cover and the Asian summer monsoon. *Int. J. Climatol. 16*, 605–616.

Schaeffer, M., F. Selten, J. Opsteegh, and H. Goosse (2002). Intrinsic limits to predictability of abrupt regional climate change in IPCC SRES scenarios. *Geophys. Res. Let. 29*(16), 10.1029/2002GL01524.

Schellnhuber, H.-J. (1997). Integrated assessment of climate change: regularity and singularity. Paper presented at the symposium 'Climate impact research: Why, how and when?', Berlin-Brandenburg Academy of Sciences and German Academy Leopoldina, Berlin, October 28-29, 1997.

Schellnhuber, H.-J. (1998). Sustainable Development: One + Four Paradigms. In H.-J. Schellnhuber and V. Wenzel (Eds.), *Earth System Analysis*. Berlin Heidelberg: Springer.

Schellnhuber, H.-J. (1999). 'Earth system' analysis and the second Copernican revolution. *Nature 402*(SUPP), C19–C23.

Schellnhuber, H.-J. and G. Yohe (1998). Comprehending the economic and social dimensions of climate change by integrated assessment. In *Proceedings of the WCRP conference, 26-28 August 1997, Geneva, Switzerland*, Geneva, Switzerland. WMO.

Schiller, A., U. Mikolajewicz, and R. Voss (1997). The stability of the North Atlantic thermohaline circulation in a coupled ocean-atmosphere general circulation model. *Climate Dynamics 13*, 325–347.

Schmittner, A. and T. Stocker (1999). The stability of the thermohaline circulation in global warming experiments. *J. Climate 12*, 1117–1133.

Schmittner, A. and A. Weaver (2001). Dependence of multiple climate states on ocean mixing parameters. *Geophys. Res. Let. 28*(6), 1027–1030.

Schneider, S. (1997). Integrated assessment modeling of global climate change: Transparent rational tool for policy making or opaque screen hiding value-laden assumptions? *Env. Mod. Ass. 2*, 229–249.

Schneider, S. and S. Thompson (2000). Simple climate model used in economic studies of global change. In S. De Canio, R. Howarth, A. Sanstad, S. Schneider, and S. Thompson (Eds.), *New directions in the economics and integrated assessment of global climate change*, pp. 59–80. Arlington, VA: Pew Center on Global Climate Change.

Schneider, S., B. Turner II, and H. Morehouse Garriga (1998). Imaginable surprise in global change science. *J. Risk Research 1*(2), 165–185.

Scott, J., J. Marotzke, and P. Stone (1999). Interhemispheric thermohaline circulation in a coupled box model. *J. Phys. Oceanogr. 29*, 351–365.

Shaffer, G. and S. Olsen (2001). Sensitivity of the thermohaline circulation and climate to ocean exchanges in a simple coupled model. *Climate Dynamics 17*, 433–444.

Slawig, T. and K. Zickfeld (2004). Parameter optimization using algorithmic differentiation in a reduced-form model of the Atlantic thermohaline circulation. *Nonlinear Analysis: Real World Applications*. In Press.

Smith, J. and G. Pitts (1997). Regional climate change scenarios for vulnerability and adaptation assessments. *Climatic Change 36*, 3–21.

Sotomayor, J. (1973). Generic bifurcations of dynamical systems. In M. Peixoto (Ed.), *Dynamical Systems*, pp. 549–560. New York: Academic Press.

Stammer, D., C. Wunsch, R. Giering, C. Eckert, P. Heimbach, J. Marotzke, A. Adcroft, C. Hill, and J. Marshall (2002). Global ocean circulation during 1992–1997, estimated from ocean observations and a general circulation model. *J. Geophys. Res. 107*(C9), 3118.

Stocker, T. and A. Schmittner (1997). Influence of CO_2 emission rates on the stability of the thermohaline circulation. *Nature 388*, 862–865.

Stommel, H. (1961). Thermohaline convection with two stable regimes of flow. *Tellus 13*, 224–241.

Thorpe, R. B., J. M. Gregory, T. C. Johns, R. A. Wood, and J. F. B. Mitchell (2001). Mechanisms determining the Atlantic thermohaline circulation response to greenhouse gas forcing in a non-flux-adjusted coupled climate model. *J. Climate 14*, 3102–3116.

Titz, S., T. Kuhlbrodt, U. Feudel, and S. Rahmstorf (2002). On freshwater-dependent bifurcations in box models of the interhemispheric thermohaline circulation. *Tellus 54*(1), 89–98.

Tóth, F., T. Bruckner, H.-M. Füssel, M. Leimbach, and G. Petschel-Held (2003a). Integrated assessment of long-term climate policies: Part 1 – model presentation. *Climatic Change 56*, 37–56.

Tóth, F., T. Bruckner, H.-M. Füssel, M. Leimbach, and G. Petschel-Held (2003b). Integrated assessment of long-term climate policies: Part 2 – model results and uncertainty analysis. *Climatic Change 56*, 57–72.

Tóth, F., G. Petschel-Held, and T. Bruckner (1998). Kyoto and the long-term climate stabilization. In *Proceedings of the OECD Workshop on Economic Modeling of Climate Change, Paris, September 17-18, 1998*.

Tziperman, E. (1997). Inherently unstable climate behavior due to weak thermohaline ocean circulation. *Nature 386*, 592–594.

Tziperman, E., J. Toggweiler, Y. Feliks, and K. Bryan (1994). Instability of the thermohaline circulation with respect to mixed boundary conditions: Is it really a problem for realistic models? *J. Phys. Oceanogr. 24*, 217–232.

UNEP/WMO (1992). *United Nations Framework Convention on Climate Change*. Geneva, Switzerland: United Nations Environment Programme and World Meteorological Organization (UNEP/WMO), Information Unit on Climate Change.

Vellinga, M. and R. Wood (2002). Global climatic impacts of a collapse of the Atlantic thermohaline circulation. *Climatic Change 54*, 251–267.

Verma, A. (2002). ADMAT: Automatic differentiation in MATLAB using object oriented methods. http://www.tc.cornell.edu/ averma/AD/admatoo.ps.

Walther, G.-R., E. Post, P. Convey, A. Menzel, C. Parmesan, T. Beebee, J.-M. Fromentin, O. Hoegh-Guldberg, and F. Bairlein (2003). Ecological responses to recent climate change. *Nature 416*, 389–395.

Watson, R., M. Zinyowera, and R. Moss (Eds.) (1996). *Climate Change 1995, Impacts, Adaptations and Mitigation of climate Change: Scientific-Technical Analysis – Contribution of Working Group II to the Second Assessment Report of the IPCC*. Cambridge: Cambridge University Press.

Webster, P. (1987). The elementary monsoon. In J. Fein and P. Stephens (Eds.), *Monsoons*. New York: John Wiley & Sons.

Webster, P., V. Magaña, T. Palmer, J. Shukla, R. Thomas, M. Yanai, and R.A.Thomas (1998). Monsoons: processes, predictability and the prospects for prediction. *J. Geophys. Res. 103*(C7), 14,451–14,510.

Wigley, T. (1994). *MAGICC (Model for the assessment of greenhouse-gas induced climate change): User's guide and scientific reference manual*. Boulder, Colorado: National Center for Atmospheric Research.

Wood, R., A. Keen, J. Mitchell, and J. Gregory (1999). Changing spatial structure of the thermohaline circulation in response to atmospheric CO_2 forcing in a climate model. *Nature 399*, 572–575.

Wright, E. L. (2003). Incorporating catastrophes into integrated assessment: science, impacts and adaptation. *Climatic Change 57*, 265–286.

Yanai, M., C. Li, and Z. Song (1992). Seasonal heating of the Tibetan Plateau and its effects on the evolution of the Asian summer monsoon. *J. Meteor. Soc. Jap. 70*, 319–351.

Zeng, N., J. Neelin, and C. Chou (2000). The first quasi-equilibrium tropical circulation model - implementation and simulation. *J. Atmos. Sci. 57*, 1767–1796.

Zickfeld, K. and T. Bruckner (2003). Reducing the risk of abrupt climate change: emissions corridors preserving the Atlantic thermohaline circulation. *Integrated Assessment 4*(2), 106–115.

Zickfeld, K., T. Slawig, and S. Rahmstorf (2004). A low-order model for the response of the Atlantic thermohaline circulation to climate change. *Ocean Dynamics 54*(1), 8–26.

Danksagung

An dieser Stelle möchte ich allen danken, die zum Gelingen dieser Arbeit beigetragen haben.

Hans-Joachim Schellnhuber gilt mein besonderer Dank– dafür, mich an das spannende Gebiet der Erdsystemanalyse herangeführt zu haben. Aus seiner Herangehensweise an integrierte Fragestellungen habe ich viel gelernt.

Stefan Rahmstorf danke ich für die Diskussionen und Anregungen bezüglich der Ozeanmodellierung.

Vladimir Petoukhov danke ich für die inhaltliche Unterstützung bei der Entwicklung des Monsunmodells. Seine Bereitschaft, jederzeit auf meine vielen Fragen einzugehen, hat mir sehr geholfen.

Thomas Bruckner und Elmar Kriegler danke ich herzlich für die vielen anregenden Diskussionen.

Matthias Lüdeke danke ich für die freundliche Betreuung in der Endphase dieser Arbeit.

Till Kuhlbrodt, Jürgen Kropp, Hermann Held, Klaus Eisenack, Jürgen Scheffran und Sven Titz danke ich für die hilfreichen Anmerkungen zu früheren Entwürfen dieser Arbeit.

Brigitte Knopf danke ich für die numerische Unterstützung bei der Erstellung der Bifurkationsdiagramme.

Ein herzliches Dankeschön auch an die vielen noch ungenannten Kollegen für die ausgesprochen nette und anregende Arbeitsatmosphäre.

Ein großer Dank gilt meinem Lebensgefährten Jens Wieting, der einige Tiefs während der Erstellung dieser Arbeit aufzufangen hatte.